The Influence of Age and Mechanical Loading on Bone Structure and Material Properties

vorgelegt von
M.Sc.
Marta Isabel Fernandes do Aido
geb. in Viseu, Portugal

von der Fakultät III - Prozesswissenschaften
der Technischen Universität Berlin
zur Erlangung des akademischen Grades

Doktor der Ingenieurwissenschaften
– Dr.-Ing. –

genehmigte Dissertation

Promotionsausschuss:

Vorsitzender: Prof. Dr. Roland Lauster
Gutachterin: Prof. Dr. Claudia Fleck
Gutachter: Prof. Dr. Peter Fratzl

Tag der wissenschaftlichen Aussprache: 23. März 2015

Berlin 2015

Acknowledgements

Writing the following words is the chance to say thank you and express my gratitude to the many people who have contributed, supported and inspired me during my PhD.

I would like to thank my supervisor Prof. Duda at the Julius Wolff Institute for the opportunity given to work in such an interesting environment and for the support and supervision throughout these years. I would also like to thank my mentor Bettina Willie not only for giving me the chance to work in such a diverse and challenging project, but also for the knowledge shared and the support through each step of this work. I thank Sara Checa for always being ready to help and discuss my work and for all the support during my PhD. I'm very thankful to Marzena Prinz for all the things she taught me in the Histology Lab. Her will to share and teach was always above any communication difficulty due to my initial scarce German. I would also like to thank Tobias Thiele for being very helpful in the first steps of my PhD and for sharing his great mice handling skills with me. I thank Annette Birkhold for the help with the animal experiments and Mario Thiele for the support with the microCT and microscopy. I would like to express my gratitude to Michael Skornia for all his tips and the time spent helping me with the University courses. Finally, I extend my thank you to all my colleagues at the Julius Wolff Institute and in particular to Hajar Razi, Paul Zaslansky, Bernhard Hesse, Peter Varga, Ansgar Petersen, Amaia Cipitria and Katharina Schmidt-Bleek, for always being available to enthusiastically discuss my work and help.

Apart from having the chance to work so close to the clinical world in the Julius Wolff Institute, I also had the privilege to work in the Max Planck Institute of Colloids and Interfaces in Golm. Not only for this opportunity, but also for all the rich and instructive meetings, the valuable feedback and the supportive guidance throughout my PhD, I would like to express my sincere gratitude to my supervisor Prof. Fratzl. I'm very thankful to Wolfgang Wagermaier for the constant support throughout the years, for the guidance and for introducing me to many new techniques. In addition, I would like to thank Michael Kerschnitzki for the knowledge shared and the techniques he taught me, especially in the beginning of my PhD. I would also like to thank Dr. Till Hartmut Metzger and Rebecca Hörth for the support during the SAXS experiments. I thank Petra Leibner for the help with nanoindentation and Birgit Schonert for the help with sample preparation. Thank you Richard Weinkamer for all the supportive and insightful discussions. Finally, I would like to thank Felix Repp for the help with the confocal microscope and the many discussions about the osteocyte project. The collaborative atmosphere and all the great people I encountered in the Biomaterials group definitely made up for the sometimes long train rides Berlin - Golm.

I would like to thank my supervisor in the Technical University of Berlin, Prof. Claudia Fleck for the supervision and support throughout my PhD. In addition, I want to thank the Berlin-Brandenburg School for Regenerative Therapies (BSRT) and in particular Dr. Sabine Bartosch, for enriching the experience of the PhD program. It's hard to sum up all the skills and the new things I learned through the different courses and events organized by the BSRT, as well as the many interesting people I was able to meet on the way.

From the Hospital of Special Surgery in New York and the collaboration in the FTIRI project, I would like to thank Dr. Adele Boskey for the helpful discussions about the project and Ludymila

Spevak for the constant availability. I am also thankful to the ESRF for the opportunity given to perform experiments at their facility and in particular, I would like to thank Manfred Burghammer, Cédric Montero and Michael Reynolds for the support with the synchrotron experiment.
I would like to thank my parents for the unconditional support, which will always be an inherent part of any project I complete. I dedicate this thesis to you, which is only a tiny gesture in comparison with your life dedication to my brother and me. I thank also my brother for always being there. Nils, thank you for following so closely and patiently all the ups and downs of these years. My very last words go to my grandfather, because I know how much they would have made him happy. Obrigada.

Abstract

Bone is not only a dynamic living tissue, but also a composite material with a complex hierarchical structure, responsible for bone's remarkable functionality. However, advanced age leads to a decrease in bone mass and compromised material quality, which can result in osteoporosis, the most prevalent skeletal disease. A promising nonpharmacological therapy against age-related bone loss and fragility is physical exercise. Although exercise is known to be beneficial to the body, the effect of mechanical loading on bone and how bone's adaptive response changes with age, in particular in terms of its material quality (which includes the properties of mineral particles and collagen matrix) is largely unknown. The cells, essential in bone adaptation to mechanical loading, are the osteocytes. These cells sense and transduce mechanical stimuli, and are part of a largely interconnected lacuno-canalicular network (LCN).

The overall aim of this work was to investigate using a materials science approach how aging influences bone mass, geometry and material quality after physiological and controlled *in vivo* mechanical loading. An axial compressive loading model was used to apply additional loads to the tibia of female young, adult and elderly mice. The first aim was to study the effect of additional mechanical loading on cortical bone mass, geometry and material properties and how age modulates the adaptive response of bone to additional loading. The results obtained revealed that the effect of additional mechanical loading varied with animal age. In young mice and to a lesser extent in adult mice, additional mechanical loading enhanced bone mass and geometry, while in elderly mice additional *in vivo* loading only maintained bone mass. However, the effect of loading on bone mineral and matrix properties was predominately observed in the elderly mice, where an enhancement of collagen maturity and degree of mineralization was detected. Interestingly, the new tissue formed with additional *in vivo* loading showed similar mineral and matrix properties to new tissue formed with physiological loading. Furthermore, the mineral and matrix properties of new bone tissue differed regionally, according to whether bone was formed on the periosteal or endocortical surface of the bone, which corresponds to different biological and mechanical environments. Pilot studies revealed that mechanical loading had an impact on the topology of the osteocyte LCN, suggesting clues to possible mechanisms responsible for age-related decreases in mechanoresponsiveness. The second aim of this work was to analyze the effect of animal age and tissue age on cortical bone mass, geometry and material properties during physiological loading. Mineral and matrix properties were shown to be animal age and tissue age dependent during physiological loading. However, the changes in bone mass and geometry with animal aging were more pronounced than the changes in mineral and matrix properties. Finally, unexpected results showed that calcein fluorochrome labels might not only bind to mineralizing surfaces, but also stunt bone's mineral growth. Additionally, the mineral particles in the proximity of blood vessels were shown to be thinner and less aligned.

The obtained results provided a broader understanding of how bone adapts to mechanical loading and how these changes are modulated by age. Interestingly, new tissue formed in response to additional loading and physiological loading was shown to have similar bone material properties and additional loading was shown to enhance bone material properties in

elderly mice. Therefore, despite some differences in skeletal aging between mice and humans, these data suggest that physical activity is a promising noninvasive treatment to enhance bone quality and maintain bone mass in individuals suffering from age-related bone loss.

Kurzfassung

Knochen bestehen nicht nur aus dynamischem, lebendem Gewebe, sie stellen auch ein Verbundmaterial mit komplexer, hierarchischer Struktur dar, welches für die erstaunliche Funktionalität von Knochen verantwortlich ist. Dennoch führt hohes Alter zu reduzierter Knochenmasse und verringerter Materialqualität, und mündet häufig in Osteoporose, einer der am weitesten verbreiteten Erkrankungen des Knochens. Körperliche Betätigung stellt eine vielversprechende, nicht-pharmazeutische Vorbeugungsmaßnahme gegen altersbedingten Knochenabbau dar. Während körperliche Betätigung allgemein als vorteilhaft für den Körper angesehen wird, ist der Effekt von mechanischer Belastung auf den Knochen und die Veränderung der Anpassungsfähigkeit des Knochens im Alter, insbesondere im Hinblick auf die Materialqualität (welche sowohl die Mineral-Partikel, als auch Eigenschaften der organischen Matrix beinhaltet), bisher wenig erforscht. Osteozyten, die Zellen, die im Knochen für die Anpassung an mechanische Belastung verantwortlich sind, detektieren und übermitteln mechanische Stimuli und sind Teil des lakuno-kanalikulären Netzwerks (LKN).

Das Ziel dieser Arbeit war es, unter Verwendung eines materialwissenschaftlichen Ansatzes die Auswirkung des Alterungsprozesses auf Knochenmasse, Knochenstruktur und Materialqualität nach physiologischer und kontrollierter mechanischer *in vivo* Belastung zu erforschen. Dazu kam ein axiales Druckbelastungsmodell zum Einsatz, um zusätzliche Belastung auf die Tibiae von weiblichen, jeweils jungen, adulten und alten Mäusen auszuüben. Das primäre Ziel war es, die Auswirkung von zusätzlicher mechanischer Belastung auf die kortikale Knochenmasse, die Geometrie und die Materialeigenschaften zu untersuchen. Zusätzlich sollte erforscht werden, wie sich das Alter auf die Fähigkeit des Knochens auswirkt, auf mechanische Belastung zu reagieren. Die im Rahmen dieser Arbeit erlangten Ergebnisse zeigen, dass die Auswirkung von zusätzlicher mechanischer Belastung abhängig vom Alter der Tiere variiert. Während bei jungen, und in geringerem Maße bei erwachsenen Mäusen ein positiver Effekt auf Knochenmasse und -struktur zu verzeichnen war, trug die zusätzliche *in vivo* Belastung bei alten Tieren lediglich dazu bei, die Knochenmasse zu erhalten. Andererseits zeigten sich bei den Eigenschaften von Mineral- und Knochenmatrix in erster Linie bei älteren Tieren Veränderungen, wo sowohl eine erhöhte Kollagenquervernetzung, als auch ein höherer Grad an Mineralisierung zu verzeichnen waren. Interessant war, dass das neu geformte Gewebe, welches unter zusätzlicher *in vivo* Belastung entstand, ähnliche Mineral- und Matrixeigenschaften zeigten wie jenes, welches durch normale physiologische Belastung entstand. Des Weiteren unterschieden sich die Materialeigenschaften des neu gebildeten Knochengewebes regional, abhängig davon, ob sich das neue Gewebe an der periostalen oder endocorticalen Oberfläche des Knochens gebildet hat, welche unterschiedliche biologische und mechanische Umgebungen darstellen. Pilotstudien haben ergeben, dass die mechanische Belastung Auswirkungen auf die Topologie des Osteozyten LKN hat, was auf Mechanismen hindeuten könnte, die mit dem altersbedingten Verlust des Reaktionsvermögens auf mechanische Einwirkungen im Zusammenhang stehen. Das zweite Ziel dieser Arbeit war die Analyse der Auswirkung von Tier- und Gewebealter auf die kortikale Knochenmasse, die Geometrie und die Materialeigenschaften während physiologischer Belastung. Bei den physiologisch belasteten Tibiae führte fortgeschrittenes Alter zu verringerter kortikaler Fläche

und Dicke. Auch Mineral-, und Matrixeigenschaften stellten sich während der physiologischen Belastung als abhängig von Tier- und Gewebealter heraus, die Veränderungen waren jedoch weniger ausgeprägt als jene der Knochenmasse und Geometrie. Schließlich zeigten unerwartete Ergebnisse, dass sich Calcein-Fluoreszenzfarbstoffe möglicherweise nicht nur mit mineralisierenden Oberflächen verbinden, sondern sich auch hemmend auf das Mineralwachstum des Knochens auswirken. Des Weiteren stellten sich Mineralpartikel in der Nähe von Blutgefäßen als dünner und weniger gleichmäßig ausgerichtet dar.

Die im Rahmen dieser Arbeit erlangten Ergebnisse liefern ein tiefergehendes Verständnis der Anpassungsfähigkeit von Knochen an mechanische Belastung und darüber, inwieweit das Alter damit im Zusammenhang steht. Interessanterweise zeigte sich, dass das neu entstandene Knochengewebe sowohl bei zusätzlicher Belastung als auch bei physiologischer Belastung ähnliche Materialeigenschaften aufweist, und dass sich zusätzliche mechanische Belastung insbesondere bei älteren Mäusen positiv auf die Materialeigenschaften auswirkt. Die Daten weisen also darauf hin, dass, trotz gewisser Unterschiede bezüglich des Alterungsprozesses von Knochen zwischen Menschen und Mäusen, physische Aktivität eine vielversprechende, nicht-invasive Behandlungsmethode zur Verbesserung der Knochenqualität und zur Erhaltung der Knochenmasse darstellt.

Contents

Acknowledgements 1
Abstract 3
Kurzfassung 5
Contents 7
List of Figures 9
List of Tables 13
Acronyms 14
1 Introduction 15
1.1 Motivation 15
1.2 Aims and structure of the thesis 16
1.2.1 Aims of the thesis 16
1.2.2 Structure of the thesis 17
2 Background 18
2.1 Bone as a hierarchically structured material 18
2.2 Aging effects on bone 23
2.2.1 Osteoporosis (clinical motivation) 23
2.2.2 Age-related changes in bone mass 25
2.2.3 Age-related changes in bone mineral and collagen 26
2.3 Mechanical loading effects on bone 30
2.3.1 Bone adaptation to mechanical loading 30
2.3.2 Mechanotransduction and the osteocyte lacuno-canalicular network (LCN) 34
2.3.3 Mechanical loading effects on bone mineral and matrix properties 37
2.3.4 Age-related changes in bone's adaptive response 38
3 Materials and methods 40
3.1 Animal handling 40
3.2 *In vivo* loading 40
3.2.1 *In vivo* load-strain calibration (strain gauging) 40
3.2.2 *In vivo* loading protocol 41
3.3 Measures of bone mass and geometry 41
3.3.1 *In vivo* micro-computed tomography (microCT) 42
3.3.2 Dynamic histomorphometry 43
3.4 Measures of bone mineral and matrix properties 44
3.4.1 Scanning small angle X-ray scattering (sSAXS) 44
3.4.2 Backscattered electron (BSE) imaging 50
3.4.3 Correlation of images 51
3.4.4 Multiphoton confocal microscopy 52
3.4.5 Fourier transform infrared imaging (FTIRI) 52
3.5 Osteocyte lacuno-canalicular network (LCN) topology and associated perilacunar material properties 54
3.5.1 Confocal laser scanning microscopy (CLSM) 54
3.5.2 Nanoindentation 56
4 Results 57

4.1 Cortical bone - mass and geometry 57
4.1.1 *In vivo* strain gauging 57
4.1.2 The effect of animal age on cortical bone mass and geometry 57
4.1.3 The effect of *in vivo* loading on cortical bone mass and geometry 58
4.2 Cortical bone - mineral and matrix properties 63
4.2.1 Synchrotron sSAXS - Selection criteria for measured points 63
4.2.2 The effect of animal age on bone mineral and matrix properties 63
4.2.3 The effect of tissue age on bone mineral and matrix properties 67
4.2.4 The effect of *in vivo* loading on mineral and matrix properties of pre-existing bone 70
4.2.5 The effect of *in vivo* loading on mineral and matrix properties of newly formed bone 71
4.2.6 Relationship between mineral properties and calcein labeling in mineralizing bone surfaces 78
4.2.7 Mineral in the vicinity of blood vessels 79
4.3 Cortical bone osteocyte lacuno-canalicular network (LCN) and perilacunar tissue 81
4.3.1 The effect of *in vivo* loading on the topology of the osteocyte LCN of newly formed bone 81
4.3.2 The mechanical properties of the perilacunar tissue 84
5 Discussion 86
5.1 The effect of additional *in vivo* mechanical loading on cortical bone mass and geometry 86
5.2 The effect of additional *in vivo* mechanical loading on cortical bone mineral and matrix properties 88
5.2.1 Mineral and matrix properties of newly formed tissue with additional *in vivo* loading 90
5.3 The topology of the osteocyte lacuno-canalicular network (LCN) and perilacunar material quality 92
5.4 The effect of animal age on cortical bone mass and geometry during normal physiological loading 93
5.5 The effect of animal age on cortical bone mineral and matrix properties during normal physiological loading 95
5.6 The effect of tissue age on cortical bone mineral and matrix properties during normal physiological loading 96
5.7 Relationship between mineral properties and calcein labeling in mineralizing bone surfaces and mineral in the vicinity of blood vessels 97
5.8 Limitations of the study 98
6 Conclusions 99
Outlook 101
References 103

List of Figures

Figure 1: Bone's hierarchical structure from the whole bone level down to its basic components: the mineral particles and the collagen molecules (adapted from [15]). 18

Figure 2: The arrangement of collagen molecules in bone. A) The collagen molecules are made of three polypeptide chains and they are B) staggered by a periodic distance of 67 nm, with overlap zones of 32 nm and gap zones of 35 nm (adapted from [19] with permission from Prof. Banaszak Holl). 19

Figure 3: The mineralized collagen fibril (reproduced from [25] with permission of The Royal Society of Chemistry). 19

Figure 4: Organization of the mineralized fibril arrays into distinct patterns: A) parallel fibrils arrays, B) woven fiber structure, C) plywood-like structure, D) radial fibril arrays (adapted from [1]). 20

Figure 5: Scheme of A) cortical and trabecular bone of a long bone, B) Cross-section of cortical bone, C) Cross-section of trabecular bone. The main bone cells can be seen: the osteoblasts (bone forming cells), osteocytes (mechanosensors) and osteoclasts (bone resorbing cells) (adapted from [39]). 21

Figure 6: Human skeleton with some of the composing bones identified. Bones can be classified according to their shape as long bones (e.g. tibia), flat bones (e.g. bones of the skull), short bones (e.g. carpus), irregular bones (e.g. vertebrae) and sesamoid bones (e.g. patella). 22

Figure 7: Scanning electron microscope (SEM) image of normal trabecular bone of a 30 year old woman and of osteoporotic trabecular bone of a 71 year old woman (adapted from [41] with permission of Prof. Timothy Arnett). 23

Figure 8: Scheme of the mechanostat mechanism described by Frost in which bone (re)modeling is activated due to differences between actual and target strains (adapted by permission from Macmillan Publishers Ltd: [IBMS BoneKEy] [138]) 32

Figure 9: Extrinsic non-invasive loading models. A) rat tibial four point bending model [164] (reproduced with permission of the Journal of Experimental Biology from [173]), B) mouse ulna loading model [163], C) mouse tibial loading model [176, 179] ([181] - reproduced by permission of The Royal Society of Chemistry). Arrows represent the loading direction. . 34

Figure 10: A) Osteocyte LCN associated with a blood vessel; BV = blood vessel (adapted from [10] with permission of John Willey and Sons), B) Scheme of an osteocyte located inside its lacunae and its connections with the surrounding space (adapted with permission of Endocrine Society from [187]; permission conveyed through Copyright Clearance Center, Inc.). 35

Figure 11: Photograph of a strain gauge positioned at the medial surface of the tibial midshaft of a 10 week old C57BL/6J mouse (left) and an isolated strain gauge (right). 40

Figure 12: Photograph of a 10 week old C57BL/6J mouse undergoing *in vivo* loading of the left tibia. 41

Figure 13: A) Photograph of a C57BL/6J mouse inside the *in vivo* microCT, **B)** Photograph a C57BL/6J mouse placed in a costume-made "microCT mouse bed". 42

Figure 14: Cortical bone analyzed with microCT at the tibial midshaft of a C57BL/6J mouse. The length of the tibia is approximately 17 mm. 43

Figure 15: Fluorescence microscopic image of a tibial cross-section of a C57BL/6J mouse. Calcein labels which allow tracking new bone formation can be seen in green color. 44
Figure 16: Scheme of the SAXS principle: the incident beam with wave vector $\vec{k}$ is transmitted through the sample and scattered with wave vector $\vec{k'}$. The scattering vector is represented as $\vec{q}$. 45
Figure 17: A) T parameter corresponds to mean mineral thickness, B) ρ parameter varies between 1 (perfectly aligned mineral particles) and 0 (randomly oriented mineral particles). 45
Figure 18: Region at the tibial midshaft (inside red box) measured with sSAXS (left) and the three studied regions of interest: intracortical, endocortical and periosteal (right). 46
Figure 19: Experimental setup for synchrotron sSAXS measurements at the ESRF. 47
Figure 20: A) Porod and B) Krakty plot obtained from radially integrated sSAXS patterns. A_2 is obtained from real data, while A_1 and A_3 are obtained through approximations; P is the Porod constant. 49
Figure 21: Azimuthal plot I(χ) of the scattering intensity. The real data points are in red and the blue line represents the fitting Gaussian function. A_1 and A_2 correspond to the fraction of aligned mineral particles and A_0 represents the fraction of randomly aligned mineral particles. 50
Figure 22: Two-dimensional contour map of the T parameter at the tibial midshaft of one C57BL/6J mouse (plotted with OriginPro 9.0). 50
Figure 23: Merged BSE and fluorescence image at the tibial midshaft of a C57BL/6J mouse. 52
Figure 24: Typical FTIRI spectrum of cortical bone. 53
Figure 25: Photographs of the tibia of a C57BL/6J mouse after different steps of the sample preparation for imaging of the osteocyte LCN with CLSM: A) Intact tibia, B) One half of the tibia after being cut into two halves with a diamond saw, C) Tibia after being in pre-infiltration and infiltration medium with rhodamine dissolved, D) Tibia after being in embedding solution for 24 hours at +4 ^{o}C. The length of the tibia is approximately 17 mm. 55
Figure 26: Strain-load regression curves for 10, 26 and 78 week old C57BL/6J mice. 57
Figure 27: MicroCT images of the cross-section of cortical bone at the midshaft of 10, 26 and 78 week old C57BL/6J mice. 58
Figure 28: Ct.Ar, Tt.Ar, Ct.Ar/Tt.Ar, Ct.Th, Imax, Imin, Ct.vTMD of the control and loaded tibial midshaft of 10, 26 and 78 week old mice at day 0, 5, 10 and 15 of the *in vivo* loading experiment (bars are standard deviations of n = 6-11 mice). 59
Figure 29: Representative fluorescence image of the cross-section of a control and loaded tibia of one 10 week old, one 26 week old and one 78 week old C57BL/6J mouse. 61
Figure 30: Histogram of the sSAXS integral intensity of one 10 week old, one 26 week old and one 78 week old mouse. The red lines in the graphs indicate the value which corresponds to half of the median and below which all points were excluded from analysis. 63
Figure 31: Mineral:matrix ratio, carbonate:mineral ratio, crystallinity, acid phosphate and collagen maturity at the intracortical region of the control tibial midshaft of 10, 26 and 78 week old C57BL/6J mice (bars are standard deviations of n = 5 mice; * = significant difference). 64

Figure 32: A) T parameter and B) ρ parameter maps at the intracortical region of the control tibial midshaft of one 10 week old, one 26 week old and one 78 week old C57BL/6J mouse. 65
Figure 33: Stack plots of A) T parameter and B) ρ parameter at the intracortical region of the control tibial midshaft of 10, 26 and 78 week old C57BL/6J mice (for each age, approximately 12000 points were measured; n = 2 mice/age). 66
Figure 34: Mineral:matrix ratio is higher in the intracortical (IC) region than in the endocortical (Endo) or periosteal (Peri) regions of the control limbs of a 26 week old mouse. A) Image of the distribution of mineral:matrix ratio in the different regions and B) respective FTIRI spectra. 67
Figure 35: Regional differences reflecting tissue age in mineral:matrix ratio, carbonate:mineral ratio, crystallinity, acid phosphate and collagen maturity for the control limbs of 10, 26 and 78 week old C57BL/6J mice (bars are standard deviations of n = 5 mice; * = significant difference). 68
Figure 36: A) Map of T parameter and B) respective graph of T parameter profile through cortex starting at the endocortical surface in the control tibia of a 26 week old mouse. The red line in the graph corresponds to the average T parameter and the shadowed pink area above and below the line represents the standard deviation. 70
Figure 37: Acid phosphate content, collagen maturity and mineral:matrix ratio in the intracortical region of the control and loaded limbs of 10, 26 and 78 week old C57BL/6J mice (bars are standard deviations of n = 5 mice; * = significant difference). 71
Figure 38: Mineral:matrix ratio, carbonate:mineral ratio, crystallinity, acid phosphate and collagen maturity of the tissue at the endocortical and periosteal regions is similar between loaded and control limbs of 10 week old mice. Averages comprise tissue at endocortical and periosteal regions and bars represent standard deviations of n = 5 mice. 72
Figure 39: T and ρ parameters of the newly formed tissue at the endocortical and periosteal regions are similar between loaded and control limbs of 10 week old mice. Averages comprise tissue at endocortical and periosteal regions and bars represent standard deviations of n = 2 mice/age. 73
Figure 40: Newly formed tissue at the endocortical region of the loaded limbs of two 10 week old mice had lower A) T parameter and B) ρ parameter than newly formed tissue at the periosteal region. 74
Figure 41: Histogram of T parameter (binning = 0.02) and ρ parameter (binning = 0.0005) of all the measured points at the endocortical and periosteal regions of the loaded limbs of two 10 week old mice. 75
Figure 42: A) Second harmonic generation by multiphoton confocal microscopy for collagen visualization in one 10 week old mouse at the tibial midshaft, B) Zoomed-in images of the endocortical and periosteal regions at the tibial midshaft. 76
Figure 43: Mineral:matrix ratio and carbonate:mineral ratio of the newly formed tissue at the endocortical and periosteal region of the loaded tibial midshaft of 10 week old mice (bars are standard deviations of n = 5 mice; * = significant difference). 77
Figure 44: T parameter of the newly formed tissue at the periosteal region of the loaded tibial midshaft of 10, 26 and 78 week old C57BL/6J mice. 77

Figure 45: Graph of the T parameter profile 30 μm through the cortex starting at the periosteal surface in the loaded tibiae of a A) 26 week old and a B) 78 week old mouse and respective C), D) T parameter map of the first 30 μm of the tibial sections. The red line in the graphs corresponds to the average T parameter and the shadowed pink area above and below the line represents the standard deviation [294]. 78
Figure 46: Lower A) T parameter and B) ρ parameter near blood vessels in the control tibia of a 10 week old mouse; BV = blood vessel [294]..... 79
Figure 47: BSE image of a control tibia of a 26 week old mouse. Lower degree of mineralization can be seen around the blood vessels; BV = blood vessel. 80
Figure 48: CLSM image of the control tibia of a 10 week old mouse rotated 90^0 in relation to bone's longitudinal direction (on the left would be the knee joint). Calcein labels can be observed in green color. 81
Figure 49: Projection of a series of CLSM images (z-stacks) at the control tibial midshaft of a 10 week old mouse. The new bone tissue is located between the calcein labels. 81
Figure 50: Graph of the decay of the cumulative node degree distribution in the new tissue at the loaded and at the control tibiae of three different 10 week old mice. The cumulative distribution establishes that the value of the probability for the degree of a specific node includes also all larger degrees. Each symbol represents a different animal. 83
Figure 51: Graph of the decay of the cumulative canalicular length distribution in the new tissue at the loaded and at the control tibiae of three different 10 week old mice. Each symbol represents a different animal. 83
Figure 52: A) Overview of a loaded tibia of a 26 week old mouse obtained by merging a series of BSE images, B) Magnified BSE image at the tibial midshaft; osteocyte lacuna chosen to be indented at the intracortical region is squared in red, C) Topographic image of the bone surface after indentation in the vicinity of the osteocye lacuna. Indents were performed with a spacing of 3 μm between each other. 84
Figure 53: A) Elastic modulus and B) hardness of tissue located up to 3 μm away and tissue located more than 9 μm away from osteocyte lacunae at the intracortical region of the loaded tibia of one 26 week old mouse (bars are standard deviations of n = 5 lacunae). . 85

List of Tables

Table 1: Mean values and standard deviations of microCT cortical bone parameters of the loaded and control tibial midshaft of 10, 26 and 78 week old mice at day 0, 5, 10 and 15 of the *in vivo* loading experiment. [a]Different from 26 week old, unpaired t-test $p<0.05$; [b]different from control, paired t-test $p<0.05$; [c]between-subject effects of animal age (10, 26 and 78 week old); [d]within-subject effects of loading (loaded, control limbs); [e]interactions between these terms, repeated measures ANOVA, $p<0.05$ [293]. 60

Table 2: Mean values and standard deviations of endocortical and periosteal bone formation indices at the loaded and control tibial midshaft of 10, 26 and 78 week old mice. [a]Different from 26 week old, unpaired t-test $p<0.05$; [b]different from control, paired t-test $p<0.05$; [c]between-subject effects of animal age (10, 26 and 78 week old); [d]within-subject effects of loading (loaded, control limbs); [e]interactions between these terms, repeated measures ANOVA, $p<0.05$. Note: Although ten, 10 week old and 26 week old mice and five, 78 week old mice were studied, some mice did not have double calcein labels present; in this case the number of mice with labels is indicated in the table [293]. 62

Table 3: Mean values of T and ρ parameters at the intracortical region of the control tibial midshaft of 10, 26 and 78 week old C57BL/6J mice (n = 2 mice/age). 66

Table 4: Mean values and standard deviations of parameters measured with FTIRI at the endocortical, intracortical and periosteal regions of the loaded and control tibial midshaft of 10, 26 and 78 week old mice. [a]Different from 26 week old, unpaired t-test $p<0.05$; [b]different from control, paired t-test $p<0.05$; [c]between-subject effects of animal age (10, 26 and 78 week old); [e]interactions between animal age and loading; [f]within-subject effects of region, repeated measures ANOVA, $p<0.05$; [g]different from periosteal; [h]different from intracortical, paired t-test $p<0.05$. 69

Table 5: Percentage (%) of the measured points, at the endocortical and periosteal regions of the loaded tibial midshaft of two 10 week old mice, with T and ρ parameters within defined value ranges. 75

Table 6: Canalicular density of the new tissue at the loaded and control tibiae of three different 10 week old mice. Each column in the table corresponds to one different animal. 82

Acronyms

LCN	Lacuno-canalicular network
microCT	Micro-computed tomography
FTIRI	Fourier transform infrared imaging
sSAXS	Scanning small angle X-ray scattering
BSE	Backscattered electron
CLSM	Confocal laser scanning microscopy
SEM	Scanning electron microscope
WHO	World Health Organization
aBMD	Areal bone mineral density
DXA	Dual-energy X-ray absorptiometry
pQCT	Peripheral quantitative computed tomography
MRI	Magnetic resonance imaging
XRD	X-ray diffraction
TMD	Tissue mineral density
AGEs	Advanced glycation end products
Pyr	Pyridinoline
deH-DHLNL	Dehydro-dihydroxylysinonorleucine
BMU	Bone multicellular unit
Imax	Maximum principal moment of inertia
Imin	Minimum principal moment of inertia
Ct.Ar	Cortical bone area
Tt.Ar	Total cross-sectional area inside the periosteal envelope
Ct.Ar/Tt.Ar	Cortical area fraction
Ct.Th	Cortical thickness
Ct.vTMD	Cortical volumetric tissue mineral density
PMMA	Polymethyl methacrylate
sLS/BS	Single-labeled surface per bone surface
dLS/BS	Double-labeled surface per bone surface
MS/BS	Mineralizing surface
MAR	Mineral apposition rate
BFR/BS	Bone formation rate
Ec.	Endocortical
Ps.	Periosteal
ESRF	European Synchrotron Radiation Facility
CCD	Charged-couple device
IR	Infrared
ANOVA	Analysis of variance
DPD	Deoxypyridinoline
LOX	Lysil oxidase
qBEI	Quantitative backscattered electron imaging

1 Introduction

1.1 Motivation

Bone is a specialized connective tissue that forms the skeleton of all vertebrates. The specific functions of bone depend on its location in the body, but they can be as varied as providing mechanical stability to the body and allowing movement, protecting the body's organs, supplying the framework for bone marrow and maintaining mineral homeostasis, by serving as a reservoir of ions, such as calcium, magnesium and phosphate. Bone is also a composite material with a complex hierarchical structure, through which it achieves a robust mechanical performance [1-3]. However, bone changes with advanced age, not only through a significant reduction in its quantity, but also through a series of qualitative alterations occurring from the whole bone level down to its basic components, the inorganic mineral particles and the organic extracellular collagen matrix. These alterations might compromise its mechanical competence and increase its fragility and risk of fracture [4]. The quality of the bone tissue includes its microarchitecture, microcrack number and frequency and its material properties determined by the mineral and organic matrix content, arrangement, orientation and composition. The changes in bone quantity have been extensively studied as a predictor of bone fracture risk, but in the last years it has become clear that changes in bone material quality are equally important [5-7]. The alterations in both bone quantity and quality with aging can result in osteoporosis, the most prevalent skeletal disease. Understanding such changes could provide more clues to the causes and nature of age-related bone loss and osteoporosis and possibly help in the development of more targeted therapies.

It is known that the skeleton benefits from physical exercise, which has the potential to decrease fracture risk by influencing bone at different levels of its hierarchy. However, while it is thought that moderate strain levels induce increases in bone mass and that this effect is reduced with aging [8, 9], less is known on how mechanical loading affects bone basic constituents: mineral and collagen. Understanding the process of bone adaptation and how loading effects on bone mass and bone quality differ between ages will help elucidating the reasons for the increased fragility of the skeleton with aging and help improve therapies that include exercise or other loading regimens to reduce bone loss in elderly populations.

The cells, thought to be crucial in the process of bone's adaptation to mechanical loading, by sensing and transducing mechanical stimuli, are the osteocytes. These cells are embedded within the mineralized tissue [10] in a highly interconnected network: the osteocyte lacuno-canalicular network (LCN). Assessment of the topology of this network and how it is impacted by bone's mechanical loading environment is essential, as this network is thought to influence bone quality [11] and maintain bone's integrity as a tissue. Additionally, a better understanding of the material properties of the tissue surrounding the lacunae and canaliculi is necessary; as such properties might have an impact on how osteocytes sense mechanical stimuli [12].

1.2 Aims and structure of the thesis

1.2.1 Aims of the thesis

The **overall aim** of this thesis was to investigate using a materials science approach the influence of age and mechanical loading on bone structure and material properties. To achieve these aims, an *in vivo* loading model was used, with which well-controlled physiological axial compressive loads were administered for two weeks to the left tibiae of mice, while the right tibia was used as a control, which did not undergo additional loading (only weight-bearing from ambulation of the mouse). The analysis was performed in postpubescent, young (10 weeks old), adult (26 weeks old), and elderly (78 weeks old) female C57BL/6J mice.

The **first aim** was to investigate the effect of additional *in vivo* mechanical loading on cortical bone mass, geometry, and material quality and determine how animal age modulates the adaptive response to additional loading.
Cortical bone's adaptive response was studied by comparing the *in vivo* loaded left tibiae with the contralateral right tibia in 10, 26 and 78 week old animals. Within this aim, the properties of the mineral particles and the collagen matrix, as well as the topology of the osteocyte (mechanosensory cells) lacuno-canalicular network (LCN) of the newly formed tissue with additional *in vivo* loading were investigated.

The **second aim** was to investigate the influence of animal age and tissue age on cortical bone mass, geometry, and material quality during normal physiological loading.
The effect of animal age on cortical bone was studied by comparing the right tibia, which was only under regular physiological loading, between 10, 26 and 78 week old animals. In addition, the effect of tissue age on cortical bone was studied by comparing mature tissue with new tissue across all animal ages.

The developed work in this thesis was achieved through the usage of a **multi-method approach**, with which bone material was analyzed at different hierarchical levels:

- **Bone mass and geometry** were initially assessed in the *in vivo* loaded and contralateral tibia with *in vivo* micro-computed tomography (microCT) at days 0, 5, 10, and 15 of the experiment. At day 15, bone formation indices were obtained with dynamic histomorphometry, being the newly formed tissue identified with fluorochrome labels.

- Afterwards, bone material quality, in particular the properties of **bone's basic constituents: the mineral particles and the collagen-rich organic matrix** were assessed in the *in vivo* loaded and contralateral tibia after two weeks of controlled *in vivo* loading. This was accomplished by using high-resolution position-resolved methods, such as synchrotron scanning small angle X-ray scattering (sSAXS), Fourier transform infrared imaging (FTIRI) and backscattered electron (BSE) imaging.

- Additionally, preliminary experiments were conducted towards understanding the impact of loading on the topology of the **LCN of bone's mechanosensory cells, the osteocytes** using recently developed staining techniques and confocal laser scanning microscopy (CLSM). Pilot studies were conducted to assess mechanical properties of the tissue surrounding the osteocyte lacunae (perilacunar tissue) with nanoindentation, as such material properties might have an impact on how the osteocyte senses mechanical stimuli.

1.2.2 Structure of the thesis

This thesis starts with the introductory chapter explaining the motivation, aims and structure of the thesis (chapter 1), followed by a chapter (chapter 2), which introduces relevant concepts and provides an overview of the state of the art on bone's hierarchical structure and the effect of age and loading on the different hierarchical levels. In chapter 3, the experimental work developed is described, providing detailed information on the materials and methods utilized. A theoretical background on some of the techniques used to characterize the structure and material quality of bone is provided. Chapter 4 presents the experimental findings of this work and is divided into three main sub-chapters: the first reports all results concerning cortical bone mass and geometry, the second includes the results related to cortical bone mineral and matrix properties and the final sub-chapter contains osteocyte LCN related results. Chapter 5 consists on the detailed discussion of these findings. The last sections of the thesis, Chapter 6 and 7, present respectively the general conclusions extracted from this work, highlighting the potential implications for the bone research community and suggestions regarding the future direction of research on the topic.

2 Background

2.1 Bone as a hierarchically structured material

Bone has a complex hierarchical structure that ranges from the nanometer scale: collagen molecules and mineral particles, up to the macroscopic scale: the whole bone (Figure 1). Bone achieves its stiffness and strength essentially through its mineral content, while its toughness is derived mainly from its collagen matrix. At the lowest level of the hierarchy, bone is defined as a composite material with an inorganic and an organic phase. Approximately 60% (in weight) of bone tissue is inorganic matter, 8 to 10% is water and the rest is organic matter [13]. The organic phase is mainly composed of collagen type I (85-90% of total protein) [3, 14], but also by a variety of noncollageneous proteins and lipids. The inorganic phase consists of mineral particles of a carbonated analogue to hydroxyapatite.

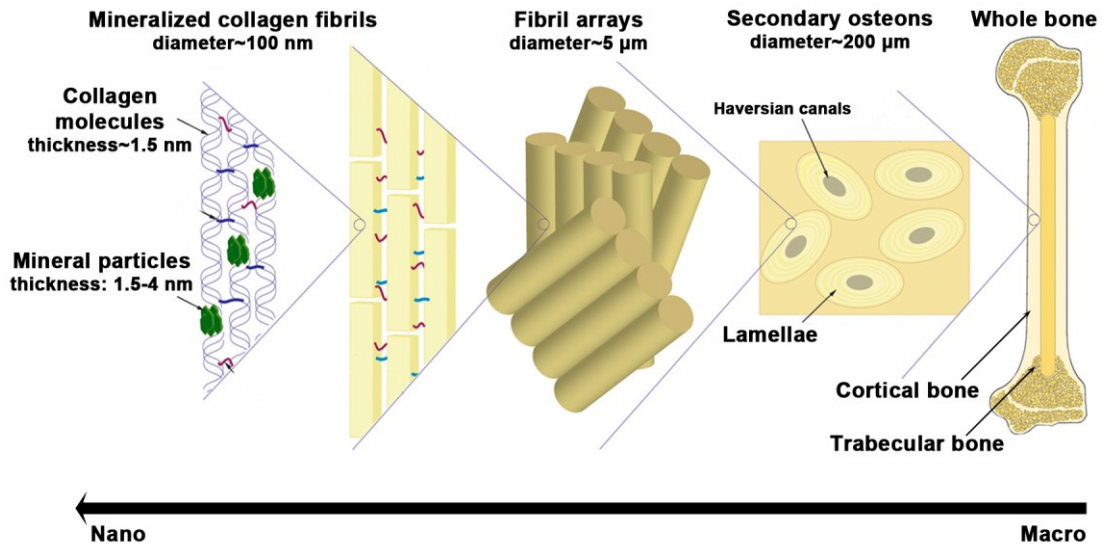

Figure 1: Bone's hierarchical structure from the whole bone level down to its basic components: the mineral particles and the collagen molecules (adapted from [15]).

The type I collagen molecule consists of three polypeptide chains which take the form a triple helix with a length of 300 nm and a thickness of 1.5 nm [1, 2] (Figure 2A). The collagen molecules are staggered along the axial direction by a periodic distance of around 67 nm (Figure 2B), forming collagen fibrils with diameters of approximately 100 nm. The fibrils form a characteristic banded structure, with overlap zones of approximately 32 nm and gap zones of around 35 nm, which are formed between the ends of each molecule [16-18] (Figure 2B).

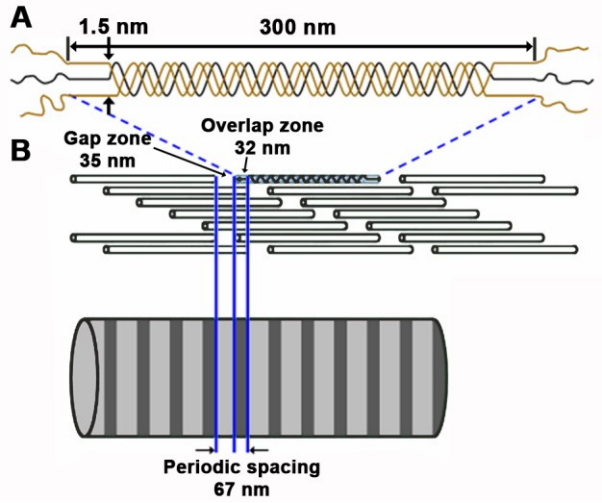

Figure 2: The arrangement of collagen molecules in bone. A) The collagen molecules are made of three polypeptide chains and they are B) staggered by a periodic distance of 67 nm, with overlap zones of 32 nm and gap zones of 35 nm (adapted from [19] with permission from Prof. Banaszak Holl).

Nucleation of mineral particles is thought to start in the gap zones [20], but recently it was suggested that nucleation starts in the overlap zones, as well [21]. Nevertheless, the mineral particles deposit on the collagen array as thin plates [22] and mainly parallel to the axis of the collagen fibrils, at regular intervals of approximately 67 nm, which correspond to the distances between the collagen molecules [23]. The carbonated hydroxyapatite particles are small and very thin, with thicknesses ranging from 1.5 to 4 nm [2, 24]. These particles can contain different impurities or inclusions, which can be absorbed onto the crystal surface and/or substituted in the lattice for constituent ions. Carbonate is the most common substitute [1, 25] but also magnesium, acid phosphate, along with other elements can be present [26, 27]. Bone's mineral is therefore poorly crystalline [28], which has implications in its solubility and in the role it plays in mineral homeostasis in the body. Apart from mineral particles embedded in the collagen fibrils, the existence of extrafibrillar mineral, possibly coating the collagen fibrils was also reported [29, 30].

The collagen-rich organic matrix and the small mineral particles constitute the basic and universal building block of the bone, the mineralized collagen fibril [1, 25], which has a thickness of 0.1 to 3 μm [3] (Figure 3).

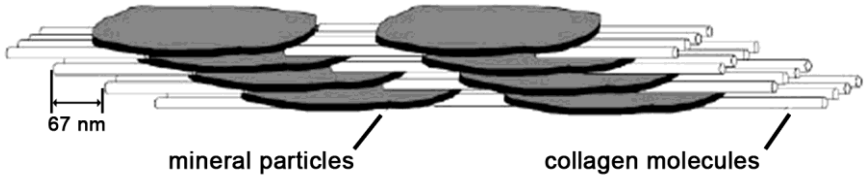

Figure 3: The mineralized collagen fibril (reproduced from [25] with permission of The Royal Society of Chemistry).

The mineralized fibrils assemble to form fibril arrays with diameters of 1 to 10 µm [2] (Figure 1). These fibril arrays can be organized into four different main patterns, classified by Wagner et al. [1] as: arrays of parallel fibrils, woven fiber structure, plywood-like structures and radial fibrils arrays (Figure 4). These patterns are characteristic, respectively, of different types of bone such as woven bone, lamellar bone, parallel-fibered bone (also called fibrolamellar bone) and the bulk of dentin [1].

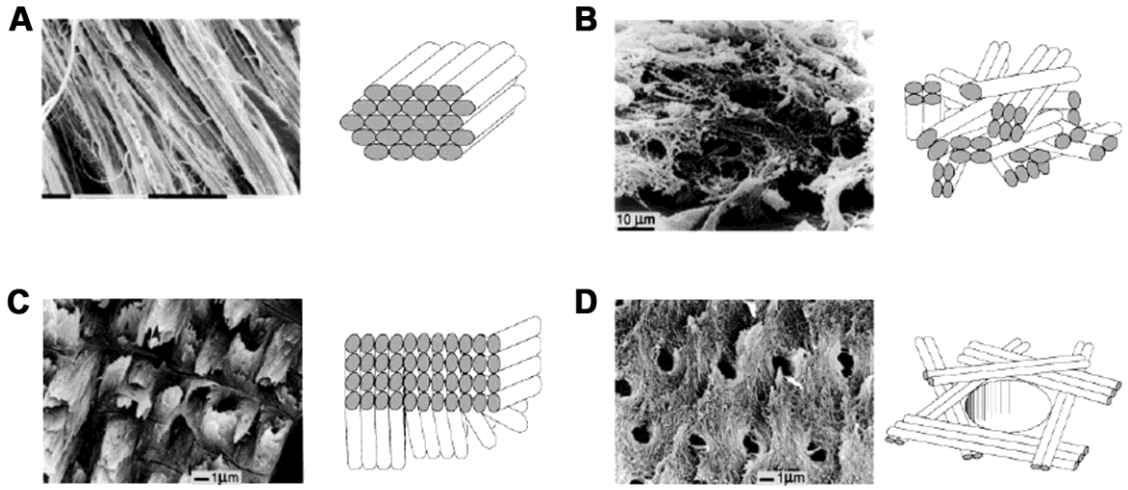

Figure 4: Organization of the mineralized fibril arrays into distinct patterns: A) parallel fibrils arrays, B) woven fiber structure, C) plywood-like structure, D) radial fibril arrays (adapted from [1]).

Woven bone is a collection of randomly oriented fibril arrays (Figure 4B) and is normally found in rapidly formed bone, for example in fracture callus or in the embryonic or newborn skeleton. Lamellar bone is formed more slowly and it results from the remodeling of woven bone or pre-existing lamellar tissue. This type of bone is made of individual layers of fibril arrays (which can also be called lamellae) often stacked in a rotated plywood fashion (Figure 4C). The rotated plywood structure is characterized by an alternation of the orientation of the fibrils between the individual layers around an axis perpendicular to the layers [1, 25, 31, 32]. However, it should be pointed out that it is still debated how in detail the tissue is arranged in lamellar bone [32, 33]. Lamellar bone is often found in mammals concentrically arranged around a canal, which contains blood vessels and nerves and which runs in the direction of the long axis of bone [34]. The unit of the central canal and the bone lamellae around is called osteon. Osteons can be classified as primary osteons, when built up during new bone formation and secondary osteons (or Haversian osteons), when formed during replacement of existing bone by new bone. Osteons are typically present in cortical bone while in trabecular bone the lamellae are organized not concentrically, but parallel along a common direction [35] (Figure 5B and C).

Cortical bone (also known as compact) and trabecular bone (also known as spongy or cancellous) define bone at a higher hierarchical level (Figure 5). Cortical bone can be found at the outer surface of bones and its thickness ranges from tenths of millimeters, at the vertebrae

to several millimeters or centimeters at the midshaft of long bones [2], while trabecular bone typically comprises the internal structures of bones, such as flat bones or the ends of long bones. Trabecular bone has been described as a foam-like network of trabeculae with a porosity of approximately 80%. Trabeculae have a thickness of 1 to 300 µm [2] and are surrounded by bone marrow, which assures the nutrition of bone cells. Cortical bone, in contrast, is fairly dense with a porosity of only approximately 6% [2], caused by blood vessels and cellular spaces. The mineral particles in cortical bone are predominantly oriented parallel to bone's long axis [25] and parallel to the collagen fibrils [2, 36], while in trabecular bone the orientation of mineral and collagen seems to follow the orientation of the trabeculae [35, 37, 38]. Approximately 80% of skeleton is cortical bone and 20% cancellous, but the relative proportions of the two vary among different skeletal sites.

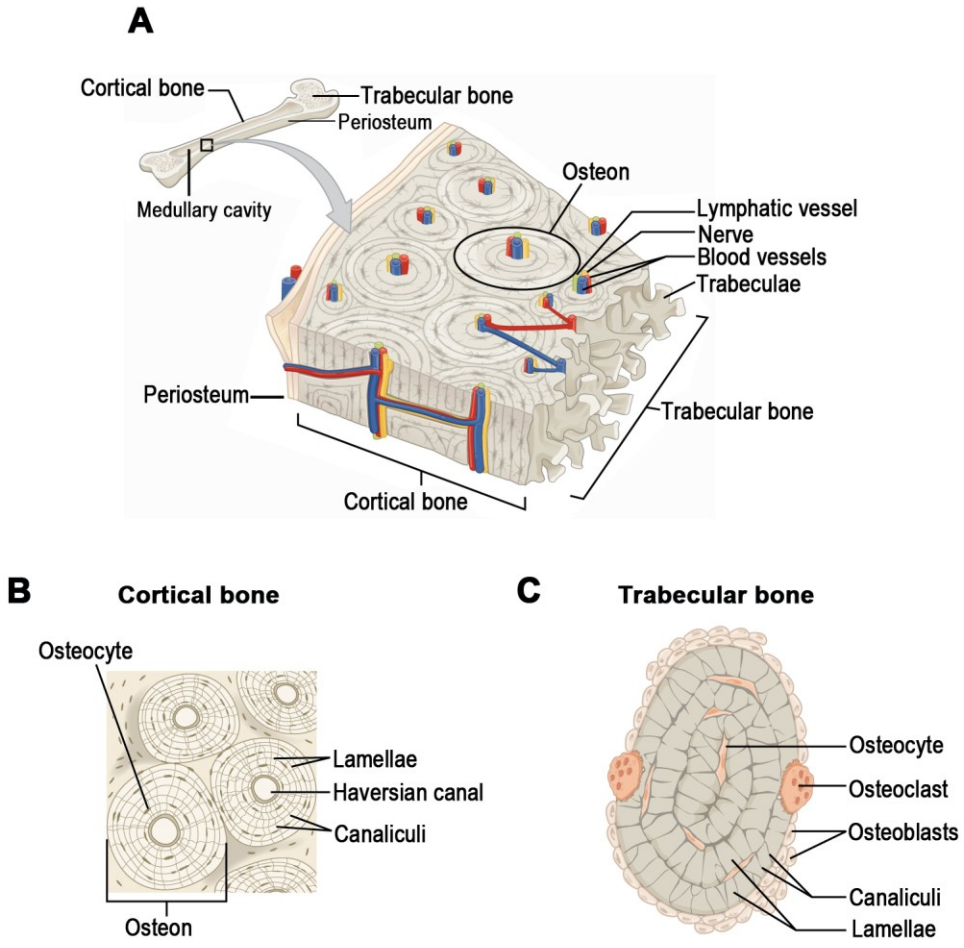

Figure 5: Scheme of A) cortical and trabecular bone of a long bone, B) Cross-section of cortical bone, C) Cross-section of trabecular bone. The main bone cells can be seen: the osteoblasts (bone forming cells), osteocytes (mechanosensors) and osteoclasts (bone resorbing cells) (adapted from [39]).

At the final level of the hierarchy bones can be divided, according to their shape, into long and flat bones, but also short, irregular and sesamoid bones (Figure 6). Long bones, such as the tibia, femur and radius are found in extremities and provide stability against bending and buckling [2]. Flat bones, such as the cranium of the skull, pelvis, rib cage and scapula, are typically found in locations where extensive protection or surface for muscular attachment is required.

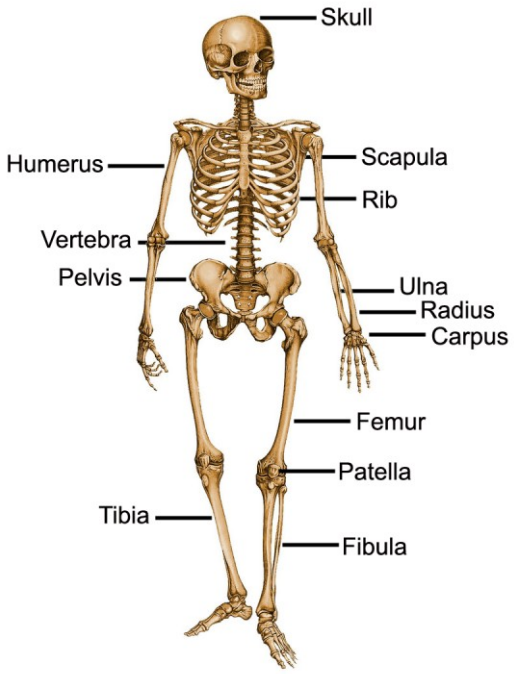

Figure 6: Human skeleton with some of the composing bones identified. Bones can be classified according to their shape as long bones (e.g. tibia), flat bones (e.g. bones of the skull), short bones (e.g. carpus), irregular bones (e.g. vertebrae) and sesamoid bones (e.g. patella).

All the described structural levels of hierarchy have important effects on the mechanics of bone [5, 15, 25] and they are all interrelated.

2.2 Aging effects on bone

Aging leads to a series of changes in bone tissue material quantity and quality, which might result in osteoporosis, a skeletal disease that affects the lives of millions of people throughout the world. Bone quality is a broad term, which includes microarchitecture (trabecular and cortical porosity), microcrack number and frequency and material properties, determined by mineral and organic matrix content, arrangement, orientation and composition.
In chapter 2.2.1 osteoporosis is introduced and a brief overview of diagnosis, prevention and treatment of the disease is provided. The alterations in bone mass with aging are presented in chapter 2.2.2 and in chapter 2.2.3 the state of the art of the changes occurring with aging in one important aspect of bone material quality, the properties of bone mineral particles and collagen matrix is described.

2.2.1 Osteoporosis (clinical motivation)

Overview of osteoporosis and scope of the clinical problem

Osteoporosis, which literally means porous bone, is associated with loss of bone mass and bone quality (Figure 7) and a consequent increase in bone fragility and susceptibility to fracture. Osteoporosis associated fractures (most common in the distal radius, the lumbar spine and the proximal femur) are estimated to occur every 3 seconds and the risk of their occurrence is 1 in 3 women and 1 in 5 in men over 50 years of age, worldwide [40]. Fractures are responsible for most of the morbidity and mortality resulting from osteoporosis.

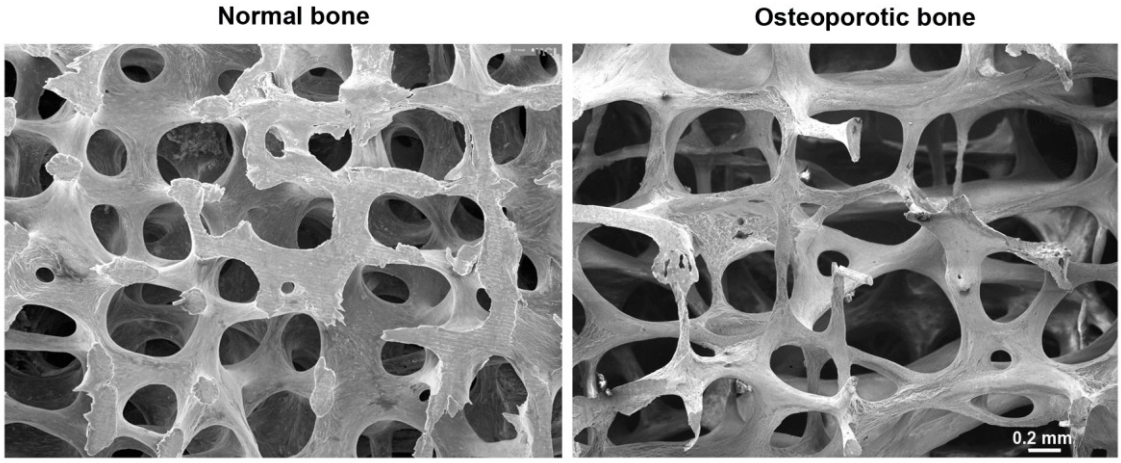

Figure 7: Scanning electron microscope (SEM) image of normal trabecular bone of a 30 year old woman and of osteoporotic trabecular bone of a 71 year old woman (adapted from [41] with permission of Prof. Timothy Arnett).

In 2003, the number of osteoporotic individuals in the world exceeded 100 million, 80% of which were women [42]. In Germany, the number amounted to 7.8 million, from which 6.5 million were women and 4.3% experienced at least one clinical fracture. More recent data (2010) estimated that 22 million women and 5.5 million men have osteoporosis in the European Union [43]. The

economic impact of osteoporosis-related fractures is enormous, with total costs reaching approximately €37 billion per year in the European Union [43] and $17.9 billion per year in the USA [44]. The aging of the population is increasing the prevalence of osteoporosis even further. However, it is interesting to note that osteoporosis is not a disease of aging, but rather an age-associated disease, with greater prevalence in older individuals.

Classifying osteoporosis into different types is not straightforward, as this is a complex disease, with a variety of causes. Primary osteoporosis was, in the 80s [45], suggested to be divided into two main different types: osteoporosis I or postmenopausal osteoporosis and osteoporosis II or senile osteoporosis. Osteoporosis type I is characterized by the loss mainly of trabecular bone after menopause in females and it results directly from the lack of the endogenous hormone, estrogen. Osteoporosis II affects both females and males and it's characterized by the loss of trabecular and cortical bone. Other types of osteoporosis, which don't start as a skeletal condition, but instead as a consequence of other diseases or of therapies used to treat other diseases, such as long-term corticoid steroid usage, are classified as secondary osteoporosis. The definition established for osteoporosis in 1994 by the World Health Organization (WHO) [46] was based only on bone mass, which is clinically measured as grams of mineral per area: areal bone mineral density (aBMD). The definition stated that if aBMD was 2.5 standard deviations below the mean for healthy young adult women, the patient was considered osteoporotic. In addition, it was proposed that if aBMD is only 1 to 2 standard deviations below, the patient is considered osteopenic, in risk of developing osteoporosis in the future. A more recent definition of osteoporosis states that it is "a disease characterized by low bone strength, leading to enhanced bone fragility and a consequent increased risk of fracture" [47]. This definition abandons the limited view of osteoporosis as purely based on bone mass, since bone strength is determined not only by the quantity, but also by the quality of the bone tissue [5, 7].

The causes of osteoporosis are very diverse. Factors that lead to a decreased peak bone mass during childhood and adolescence or to an increase in bone's loss during menopause and aging are important contributors to osteoporosis development. Bone loss is influenced during life by a variety of factors, such as nutrition (calcium intake, vitamin D status), hormones (estrogen levels, growth hormone levels), lifestyle (smoking, inactivity, loss of muscle mass) and even illnesses and medication [48]. However other factors than reduced bone mass, contribute to osteoporosis associated fractures. In fact, it was shown that fracture risk increases independently of bone mass [49-51]. The quality of the bone tissue, which includes the material properties of bone's mineral and matrix, is thought to be an important contributor to osteoporotic fracture risk [6].

Diagnosis and treatment of osteoporosis

In the past, the diagnosis of osteoporosis was very difficult, since in radiographs this condition was only possible to detect at a very advanced stage. A big step occurred with the introduction of a non-invasive bone mass measurement technique, dual-energy X-ray absorptiometry (DXA), with which aBMD is obtained. This parameter became the most common indicator of

osteoporosis and fracture risk, as the reduction in aBMD was shown to be inversely related to fracture risk in patients with osteoporosis [52-54]. However, assessing aBMD is not sufficient to totally understand the causes and nature of osteoporosis. Relying only on aBMD and the WHO definition presents several limitations, such as the fact that aBMD varies a lot according to the skeletal site (diagnosis based only on one skeletal site might be misleading) and the fact that the reference aBMD values were established only for Caucasian populations. In addition, many osteoporosis-associated fractures occur in individuals with bone mass in the normal to osteopenic range [55, 56]. Different qualitative features of the bone are only partially reflected or totally excluded from aBMD measurements. As an example, aBMD doesn't allow a distinction between thicker bones (greater quantity) and bones with higher mineralization (altered quality) [57]. However nowadays some aspects of bone quality, such as its microarchitecture can be assessed with techniques such as high resolution peripheral quantitative computed tomography (pQCT), high resolution magnetic resonance imaging (MRI) and microCT. Nevertheless, a series of other bone's qualitative features are still excluded from current diagnosis.

Different pharmacological approaches were developed with the aim to reduce further bone loss and even reverse bone loss in osteoporotic patients. Currently, the most common therapy to prevent and treat osteoporosis is hormone (estrogen) replacement therapy. However, there are various antiresorptive or antiremodelling drugs in use, such as calcitonin, bisphosphonates, and selective estrogen receptor modulators [58]. In addition, osteoporosis can be treated by intermittent parathyroid hormone administration [59], which promotes bone formation. Other anabolic agents such as sclerostin neutralizing antibody (inhibitor of sclerostin) are currently being investigated and showing promising results [60, 61].

2.2.2 Age-related changes in bone mass

The phenomenon of age-related bone loss is universal. It affects not only every person, but also every bone, although at different rates and amounts. Bone mass is known to increase during growth, until it reaches a peak value at around 20 to 30 years old [62]. Peak bone mass is followed by a plateau during young adulthood. After this plateau, bone mass starts to decrease. This onset of bone-loss in young adulthood has been demonstrated in men and women using densitometry and computed tomography [63-65]. Riggs et al. [64] have shown that before 50 years old, women have already experienced 37% and men 42% of their lifetime trabecular bone loss and 6% and 15% of their total lifetime cortical bone loss. For women, in their early postmenopausal years there is a great loss of trabecular bone (particularly at the vertebrae) [66]. This stage is followed by a more gradual bone loss at both cortical and trabecular bone sites, characteristic not only of women but also men [67]. An interesting fact is that at the age of 70, less than 70% of young adult mass can remain. In the eighth and ninth decades of life, the rate of bone loss is comparable to that occurring in the peri and postmenopausal stages for some women [68, 69].

Bone loss in cortical bone seems to occur mainly at the endocortical surface and to a smaller degree due to enlargement of Harversian canals [70]. The result is the thinning of the cortex, as

well as the expansion of the marrow cavity. There is however a small gain of bone mass at the periosteal surface [71, 72], which leads to an increased diameter of the bone [70, 73]. Bone loss at trabecular bone sites results from increased resorption depths and perforation or even loss of trabeculae, which translates into decreased trabecular interconnectivity [74-76].

2.2.3 Age-related changes in bone mineral and collagen

Changes in bone mass alone do not explain the increased fragility and fracture risk of elderly individuals. It has become apparent that also the quality of bone material, which includes the micro and nanoscopic properties of the mineral particles and the collagen organic matrix, contributes to the increased fragility of bone with advanced age [77]. The diversity of techniques used, as well as the difference in bones and species analyzed, contributes to the lack of agreement on how certain properties, such as mineral particle size and perfection, degree of mineral alignment or collagen maturity, change with animal age or tissue age.

Age-related changes in bone mineral

Degree of mineralization

The degree of mineralization of bone has a large impact on its mechanical properties. An increase in degree of mineralization confers bone tissue with higher stiffness and strength, but mineralization above an optimal level can lead to excessive brittleness [78-80].
In general, bone's degree of mineralization seems to increase sharply during the first years of growth and to reach a plateau at an adult age. The sharp increase was seen by Miller et al. [81], who reported that during the first 40 days of life, tissue mineral density (TMD) and mineral:matrix ratio in murine tibia increased and reached 62% and 80%, respectively of the values of the 450 day old mice (defined as adult mice in the study). In addition, an increase in mineral:matrix ratio was shown to occur until adult age in mice calvariae [82] and in femora of baboons [83, 84]. While the increase in the degree of mineralization up to adulthood seems to be consistent in the literature, the same doesn't hold true for the changes occurring after this stage. Studies on the femora of baboons showed either no relationship between mineral:matrix ratio and animal age [84] or a decrease of this ratio after adulthood [83]. In contrast, it was shown that there was still an increase in mineral:matrix ratio in elderly mice, when compared with young and middle-aged animals [85] and also in humans, aged between 52 to 85 years old [86]. An interesting finding was that the variations about the mean mineral:matrix ratio became tighter with individual's age and shifted towards higher mineralization values [87].
The increase in degree of mineralization with bone's tissue age seems to be consensual in the literature. Already in the 60s, BSE imaging studies revealed a gradient of mineral density around osteons, with younger bone close to the blood vessels having the lowest degree of mineralization [88, 89]. Similar findings were obtained when measuring the parameter mineral:matrix ratio in studies with rat femora [90] and tibiae [91], baboon femora [83] and both trabecular and cortical human bone [92].

Carbonate and acid phosphate in the mineral particles

Carbonate is the most common constituent impurity of bone mineral, which substitutes hydroxide (OH^-) and phosphate (PO_4^{3-}) and also adsorbs on the surface of the mineral particles. Acid phosphate is also usually present. Both play a relevant role in the chemical and physical interaction properties of the mineral particles and therefore also in their mechanical functions. It was shown that the substitution of carbonate for phosphate ions can alter the mineral shape, deteriorate the symmetry of the crystal lattice and create lattice vacancies, which can have relevant mechanical impact, as the strain environment local to mineral particles changes [93, 94].

Carbonate substitution was shown to increase slightly with individual's age in homogenized bone of iliac crest biopsies of individuals aged 0 to 90 years [95]. A series of Raman and FTIR spectroscopic studies, in which different bones and different animals were analyzed, also showed an increase in the parameter carbonate:mineral ratio with animal age [82, 83, 85, 86, 96, 97]. Distinct trends of alteration in carbonate content of mineral particles were shown to occur in baboon femora, where carbonate:mineral ratio increased only up to sexual maturity (remaining independent of animal age after this stage) [84] and mice tibia, where no significant change on carbonate content occurred with aging [81]. As with mineral:matrix ratio, the variations in carbonate content seem to be become smaller with age [87].
Studies that analyzed the carbonate content as a function of tissue age revealed conflicting results. Donnelly et al. [90] reported an increase in the parameter carbonate:mineral ratio with tissue aging in young rat femora and Burket et al. [84] reported only a trend of increase of this parameter in the femora of young and mature baboons. In contrast, a decrease in carbonate:mineral ratio with tissue aging was observed in the femora of young and middle-aged rats [85] and also in individual human osteons [92] and human trabeculae [97]. In synthetically formed crystals (similar to bone apatite), the earliest formed crystals were shown to have low concentration of carbonate [98].

The number of studies analyzing the alterations of acid phosphate content in the mineral particles with animal aging is limited, however a decrease in acid phosphate content was observed in mice up to 6 months old [99] and also in homogeneized bone biopsies of humans aged 0 to 90 years old [95]. Acid phophate content also decreases with tissue aging. Increased acid phosphate content was reported in areas of new bone formation and in early formed synthetic crystals [99-101].

Mineral particles size and perfection

Mineral crystallinity reflects the size and/or how well the atoms and ions of the mineral particles are ordered. Although the increase in mineral particles dimensions is known to induce residual stresses in their vicinity, the relation between mineral crystallinity and bone's tissue mechanical properties is not yet known. Theoretical mechanical models predicted that an increase in the mineral particles length/width ratio and in the spacing between particles led to an increase in

bone's tissue elastic modulus [102] and an experimental study showed partial correlation between mineral crystallinity and bone's elastic and post-yield mechanical properties [86].

Studies analyzing bone mineral crystallinity either show an increase in this parameter in early stages of growth [81] and up to sexual maturity [103], an increase even in elderly animals [84, 85, 96] or no relation between crystallinity and age [97]. Miller et al. [81] showed that at 1 day old, the mineral in the tibiae of BALB mice already reached 87% of their adult crystallinity value. Boskey [103] showed that bone's mineral crystallinity increased in mice during adolescence, reaching a plateau at sexual maturity. However, mineral crystallinity was reported to increase in elderly 19 month old C57BL/6 mice, when compared to 4 and 5 months old (grouped together) mice [96] and similar results were reported for the femora of female rats [85] and female baboons [84]. A different study on the baboon femora showed, in contrast, no correlation between animal age and mineral crystallinity [83] and the same was detected in human trabecular bone [97].
Most of the existing studies reported increased mineral crystallinity with increased tissue age. In the femora of baboons, there was an increase of crystallinity from the center of the osteon to approximately half its radius and a plateau afterwards, independent of animal age [83]. In a different study also with baboon femora, the increase was dependent on animal age (greater in young than in mature animals) [84]. In both trabecular and cortical human bone, crystallinity was higher in more mature tissue [92, 104].

The length of bone mineral particles in the human femora was shown to increase only up to 20 years of age and in human iliac crest up to 30 years of age (85-90 years old was the maximum age studied) [95, 105]. However, Chatterji et al. [106] showed, using X-ray diffraction (XRD), that the percentage of large mineral particles in human femora increased after 40 years old, while the percentage of small particles increased up to this age.
The smallest dimension of bone, its thickness, has also been investigated with techniques such as SAXS. Bone's mean mineral thickness was shown to negative correlate with bone's stiffness in human dentine [107]. Bone's mean mineral thickness increases in early years of skeletal growth [108] and afterwards this increase is thought to slow down, possibly reaching a plateau at an adult age, as reported by Fratzl et al. [109, 110]. Similarly, Grabner et al. [111] reported a significant increase in bone mean mineral thickness in the femora and tibiae of mice, but only up to 2 to 3 months of age (6 to 8 month old was the maximum age studied). Roschger et al. [38] in a study of vertebrae from 15 week old up to 97 years old individuals, showed a rapid increase in mineral thickness up to the age of four years old, followed by only subtle increases in thickness after this age. Bone mean mineral thickness also remained substantially the same in femora of humans between 13 and 97 years old [106].
With tissue aging, bone's mean mineral thickness seems to increase. Lower mineral thickness was detected in younger tissue adjacent to the endocortical bone surface in rat femora (compared to intracortical tissue) [112] and also in young tissue close to the center of osteons in human femora, when compared to tissue further away from the center [113].

Mineral particles degree of alignment

The mineral particles degree of alignment increases in early phases of skeletal growth [36, 108], but after this stage it is not clear how this parameter relates with age. Mineral particles degree of alignment was shown to increase with age in vertebrae of humans aged between 15 week and 97 years old [38]. However, no correlation between the degree of mineral alignment and age was seen in the human femora after 10 years of age (97 years old was the maximum age studied) [106] and also in mice aged between 1 and 8 month old [111]. Chatterji et al. [106, 114] point out that there is only a correlation between degree of mineral alignment in human femora and age in the first years of life, since at this stage the degree of preferred alignment results from the alternate stressing and relaxation of bone during limb's usage and after these early years, no changes are expected as the limb is in full usage (fully weight bearing in locomotion).
The degree of mineral alignment seems to increase with tissue age. In tissue close to the center of osteons of human femora, the degree of mineral alignment is smaller than in tissue further away from the center [113]. In addition, smaller degree of mineral alignment was measured in tissue close to the trabeculae surface (compared to older tissue in the middle of the trabeculae) [115].

Age-related changes in bone's collagen

Collagen plays an essential role in bone's mechanical features, contributing majorly to its toughness and ultimate strength [116-119]. Alterations in collagen properties seem to relate to the reduced mechanical properties of bone with advancing age and disease [25, 120, 121]. It is known that the content of collagen, in terms of % of tissue weight, gradually decreases with aging, after reaching a peak in adolescence [122] and that its stability also decreases. The orientation of collagen fibrils seems to also depend on age, at least, on tissue age. It was shown that collagen fibril orientation increases with tissue age in baboon osteonal bone [123].

One of collagen's most distinct features is its cross-linking chemistry. Whether and how the different bone's collagen cross-links—enzymatic (mature and immature cross-links) and non-enzymatic (advanced glycation end products (AGEs))—change with age and how they impact bone's mechanical properties is still a matter of discussion. Nevertheless, it seems that impaired enzymatic cross-linking and/or an increase in non-enzymatic cross-links play an important role in the decline of bone's mechanical properties with aging and osteoporosis [122]. An increase in the rate of AGEs with age was reported [124] and this was related to decreased bone's strength and toughness [125]. In addition, recent data suggests that the accumulation of AGEs cross-links within the bone tissue can only be removed by bone resorption, which leads to an increased activity of osteoclasts and decreased bone formation by osteoblasts [126]. Enzymatic mature cross-links were shown to correlate positively with ultimate stress [127] and a reduction in immature cross-links was associated with a decrease in femoral strength [128].
Age-related changes in enzymatic cross-links can be studied with FTIRI. The intensity ratio of amide I sub-bands, 1660 and 1690 cm^{-1}, the so-called collagen maturity, correlates with the ratio of nonreducible (mature)/reducible (immature) collagen enzymatic cross-links in bone, in specific with the ratio of pyrdinoline (PYD) and dehydro-dihydroxylysinonorleucine (deH-DHLNL)

[129]. For different animal species, collagen maturity was show to increase from birth up to a young age and to remain constant in adult life [84, 91, 96, 130]. In contrast, Miller et al. [81] showed no change in collagen maturity in mice between 1 and 450 days old and Paschalis et al. [129] reported increased collagen maturity between 4 month old and 2 years old bovine demineralized femora.
With tissue aging, most studies showed an increase in bone's collagen maturity [83, 129, 131, 132].

2.3 Mechanical loading effects on bone

Bone adapts to its mechanical environment during skeletal growth and development in order to attain an optimized structure in terms of size, shape and/or mineral and matrix properties, which assures its mechanical competence and resistance to fracture during normal activities. However, bone's adaptive response is modulated by an individual's age.
Bone adaptation can occur through processes of bone modeling and/or remodeling, commonly referred to as bone (re)modeling. Bone modeling corresponds to the deposition or removal of bone from periosteal, endocortical or trabecular surfaces and it doesn't require the coordinated action of bone cells. Bone remodeling can affect all bone surfaces, including vascular cavities and it requires the action of the bone multicellular unit (BMU), which involves the coordinated action of osteoclasts, the cells that initially resorb bone and osteoblasts, the cells that form bone, which replaces the resorbed bone. Bone (re)modeling occurs at approximately 1 to 2 million microscopic sites in the adult skeleton [2]. For bone's adaptation to occur there has to be a pathway of cellular events, which connect the local mechanical strains to bone (re)modeling and the osteocyte LCN is thought to play an essential role in this process.
In chapter 2.3.1, the basic principles of bone adaptation to mechanical loading and some classic studies on the topic are presented, followed by a description of the animal pre-clinical loading models used to study bone adaptation. In chapter 2.3.2 the process of mechanotransduction in bone and in particular the role of the osteocyte LCN is described. Chapter 2.3.3 focuses on the changes in bone mineral and matrix properties, after mechanical loading, an aspect which has received less attention, since mostly changes in bone mass and geometry have been studied. Finally, the age-related changes in bone's adaptive response are described in chapter 2.3.4.

2.3.1 Bone adaptation to mechanical loading

Basic principles/ Classic experiments

A classic experiment which can be used to introduce the topic of bone adaption to mechanical loading included the transplantation of a cartilage model of a femur [133] from a fetal mouse into the spleen (not subjected to mechanical loads). The bone that developed from the cartilage had a similar shape to a normal femur, but at the same time presented very distinct features, such as thinner cortices, less organized trabeculae and a short and wide femoral neck, which corresponded to weaker bones that couldn't withstand normal loads without having risk of damage. The differences were probably a reflex of the lack of the usual mechanical stimuli, which didn't allow the organ to develop into the normal functional femur. While the gross

features of the bone seemed to be genetically determined, the attributes essential to structural competence were likely dependent on the mechanical environment. In fact, the general shape of bones already suggests that the mechanical loads that act upon them lead to structural adaptation. In the 17th century, Galileo related the shape and internal structure of bone with the mechanical loading during normal functionality. Later, at the end of the 18th century, Julius Wolff studied the structure of trabecular bone in the proximal femur. He and Wilhem Roux are still remembered for "Wolff's law" or "Wolff-Roux law" [134, 135]. According to this law, the arrangement of the trabeculae in the proximal femur is in alignment with the principal stress directions subjected to the tissue during normal skeletal function. The law states that bone is deposited wherever it's needed and resorbed where there is no mechanical need, defining this way that bone (re)modeling is not random, but rather mechanically driven.

Frost further developed the idea that bone (re)modeling is mechanically driven, proposing that the principal determinant of bone adaptation was local mechanical strain. In 1987, he suggested that bone adaptation was regulated by a mechanically controlled feedback loop, which he called the mechanostat [136, 137] (Figure 8). The analogy with a thermostat, that switches heating on and off according to set points, helps understanding how the mechanostat functions (it's only on in response to "errors" and off if there are no "errors"). When there is mechanical overloading or increased strain-related stimulation due to high strains, high strain rates and unusual strain distributions, the mechanostat will evoke bone deposition and/or apparently increased strain-resistant architecture, which will occur until regular strains in the region are reestablished. The same principle is applied if there is decreased strain-related stimulation associated with mechanical disuse or a persistent underload. The mechanostat will signal for bone resorption and bone mass will diminish to a level corresponding to the lower load. For both cases, the goal seems to be to locally alter the bone in a way that the same applied forces result in different and more adequate strains in bone. The set points are defined as a range of strain values where no response occurs. This set points can however be altered by nonmechanical factors, such as drugs and hormones, which can make the mechanostat either more or less robust.

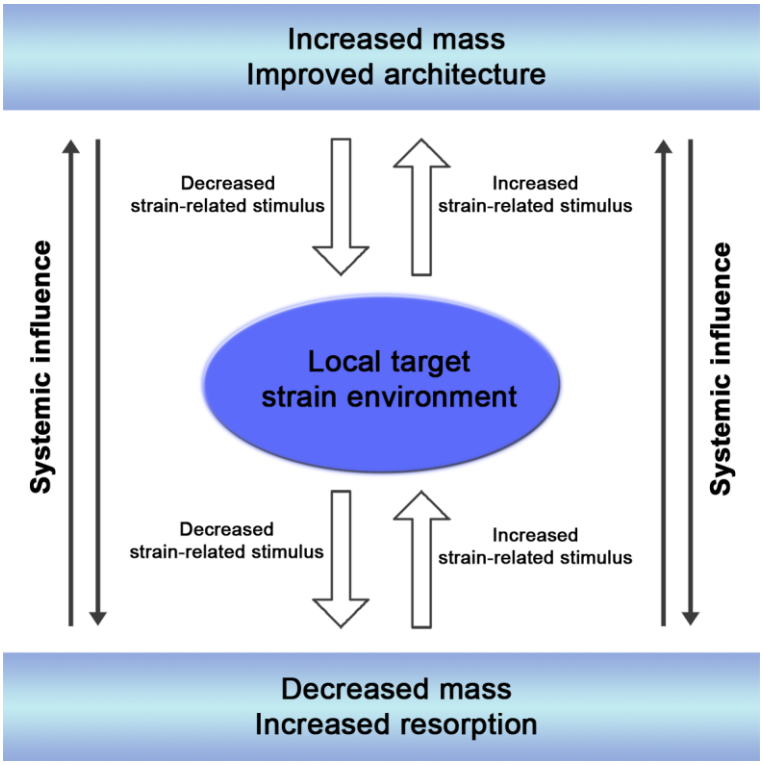

Figure 8: Scheme of the mechanostat mechanism described by Frost in which bone (re)modeling is activated due to differences between actual and target strains (adapted by permission from Macmillan Publishers Ltd: [IBMS BoneKEy] [138])

The general response of the skeleton to increased or decreased activity has been well characterized in a series of studies. Withdrawal or reduction of load bearing in bones, such as during bed rest [139] or weightlessness, such as in space flight [140, 141] were shown to result in a decrease in bone mass and growth rate of bone, which translated into a reduction in its stiffness, strength and energy absorbing ability [142]. The opposite effect, local increase in bone mass, occurred in bones that were intensively or unusually highly loaded. The classic example is the increased bone density and diameter of the playing arm of tennis players, when compared to the contralateral arm [143-145]. Also, ballerinas were shown to have more bone mass in their legs [146], middle-aged runners to have more bone mineral than sedentary people [147] and soccer players to have higher mineral density in their lower limbs, compared to control individuals [148].

Finally, the ability of a loading regimen to result in adaptive changes in bone is determined by how different the strain environment is to the habitual strain distributions to which the bone is usually exposed. It was shown that activities like jumping, tennis, weight lifting are more osteogenic than activities such as swimming and cycling, since these activities result in rapid accelerations and decelerations and unusual loading configurations [149-151].

Animal pre-clinical loading models

Animal loading models, with which the response of bone to enhanced loading environments could be studied, contributed to a significant progress in the understanding of bone adaptation to mechanical loading. *In vivo* loading models can be divided into four main categories, according to the origin of the loading and according to whether surgical intervention was used or not: intrinsic non-invasive (exercise), intrinsic invasive (osteotomy), extrinsic invasive (surgical) and extrinsic non-invasive models (external mechanical actuator) [152] (Figure 9).

Intrinsic non-invasive loading models include exercise regimes such as treadmill running [153] or jumping [154], where loading is determined by the animal's own activity. These models are limited by the lack of controlled loading parameters. Intrinsic invasive models—surgical procedures where a bone or part of a bone is removed in order to increase the mechanical loading of the bone nearby—are also limited by the noncontrolled loading conditions, as well as by the potential surgery-induced inflammation and consequent production of woven bone [155, 156]. Using a dog ulnar osteotomy model, Takano et al. [157] showed that collagen orientation in the new secondary osteons of the canine radius was determined by the new strain fields.

From one of the earliest extrinsic invasive models—rabbit tibia with surgically inserted wires—we learned that only dynamic, rather than static loading stimulates bone formation [158]. This finding was confirmed by Lanyon's group [159] using the ulnar osteotomy loading model, where pins were surgically inserted through the ends of the ulna of mature turkeys. Other extrinsic invasive loading models were developed in order to the study the trabecular bone's mechanical response to loading, such as the rat [160] and the mouse [161, 162] tail vertebral model. The major limitation of extrinsic invasive models is the potentially confounding effects of trauma associated with the surgery.

Non-invasive extrinsic loading models overcame most of the limitations of the other types of models, allowing the exact mechanical loads applied to bone to be controlled, not requiring any surgical procedure. For the rat, an axial compressive loading of the ulna model [163] and a tibial four point bending model [164] (Figure 9A) were developed in 1994 and 1991, respectively and later these models were adapted to the mouse [165, 166] (Figure 9B). The ulnar compression model creates physiological strains distributions within the bone similar to those occurring during locomotion [167], but this is not the case for the tibial four point bending model. Both loading models have contributed to the knowledge of the loading conditions that elicit bone formation. Turner et al. [168, 169] showed that increased strain rate led to increased bone formation in the rat tibia. Furthermore, the loading effect was reported to saturate with increasing number of loading cycles [170], with a short duration mechanical loading being sufficient to initiate an adaptive response. Dividing up the daily loading into a series of short bouts was also more effective in eliciting bone formation than the same stimulus applied in one burst on one day [171]. The positive effects of division of the loading cycles might be related to a loss of bone's cell sensitivity to repeated mechanical loading. In fact, not only the recovery between bouts increased the effects of loading, but also the recovery between each individual cycle [172, 173]. The insertion of a 10 second pause between cycles increased periosteal bone

formation in the *in vivo* loaded ulna of turkey [172] and similar results were obtained using the four point rat tibial loading model [173]. The benefits of insertion of pauses between cycles is not clearly understood, but it might be related to intracellular calcium signal mechanisms [174]. More recently, an axial compressive mouse tibial loading model was developed [175, 176] (Figure 9C), which uses *in vivo* strains within a physiological range and allows the study of both trabecular and cortical bone adaptation. Studies with the tibial loading model showed that a strain of 1200 με elicited an osteogenic response in the mouse tibia [177, 178]. This value corresponds to approximately two to three times the strain engendered on the medial tibiae of mice during normal walking [176, 179]. Strain gauging is commonly used to calibrate the *in vivo* loading experimental setup, by obtaining the relation between the applied loads and the strain engendered at the strain gauge location [176, 179]. Even if the strain values obtained correspond only to a specific site in bone (where the strain gauges are surgically implanted), finite element models allow the extrapolation of strains for other sites in bone [177, 180].

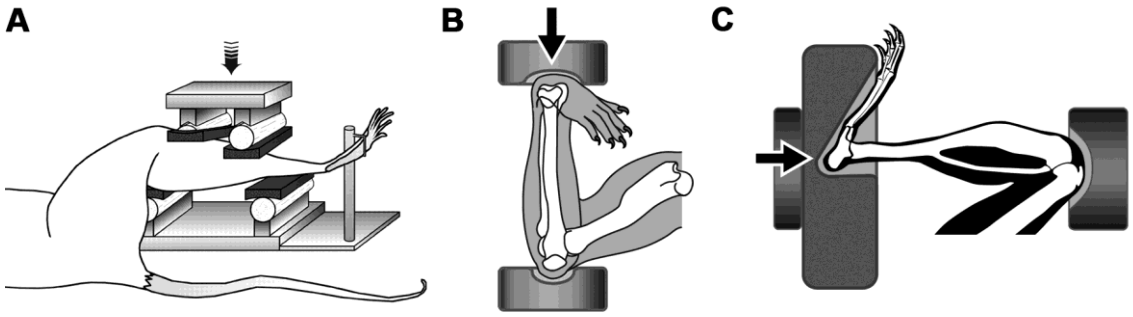

Figure 9: Extrinsic non-invasive loading models. A) rat tibial four point bending model [164] (reproduced with permission of the Journal of Experimental Biology from [173]), B) mouse ulna loading model [163], C) mouse tibial loading model [176, 179] ([181] - reproduced by permission of The Royal Society of Chemistry). Arrows represent the loading direction.

2.3.2 Mechanotransduction and the osteocyte lacuno-canalicular network (LCN)

The process of sensing the external mechanical stimuli and converting them into biochemical signals (mechanotransduction) of bone resorption or formation is still a matter of debate. However, it is generally accepted that osteocytes, with their dense distribution throughout the bone matrix and their lacuno-canalicular interconnectivity, are the cells that orchestrate this process [182]. Osteocytes, reside within lacunae and are connected to each other, to cells on the bone surface and also to the bone marrow through long dendritic processes that reside in and travel through canals in the bone tissue called canaliculi (100-550 nm diameter) [183, 184] (Figure 10). The osteocytes and their lacunae seem to align in the principal mechanical loading direction, as such the osteocyte and osteocyte lacuna morphology and orientation were shown to be different for flat and long bones in 3 to 6 month old adult C57BL/6 mice [185]. Namely, fibular osteocytes show an elongated morphology with the long axes of the lacunae in alignment with the principal mechanical loading direction, whereas osteocytes in calvariae are spherical and without any particular lacunar alignment (calvariae are loaded in different directions and at lower amplitudes). In addition, it seems that the osteocytes develop a well-organized LCN

during normal bone (re)modeling. It was shown that osteocyte lacunae in murine femoral bone of 3 week old animals have a round shape and no perceptible alignment, with their canaliculi extending in arbitrary directions, while older animals show spindle-shaped lacunae organized parallel to the longitudinal axis of the bone, with canaliculi extended perpendicularly to the bone surface [186].

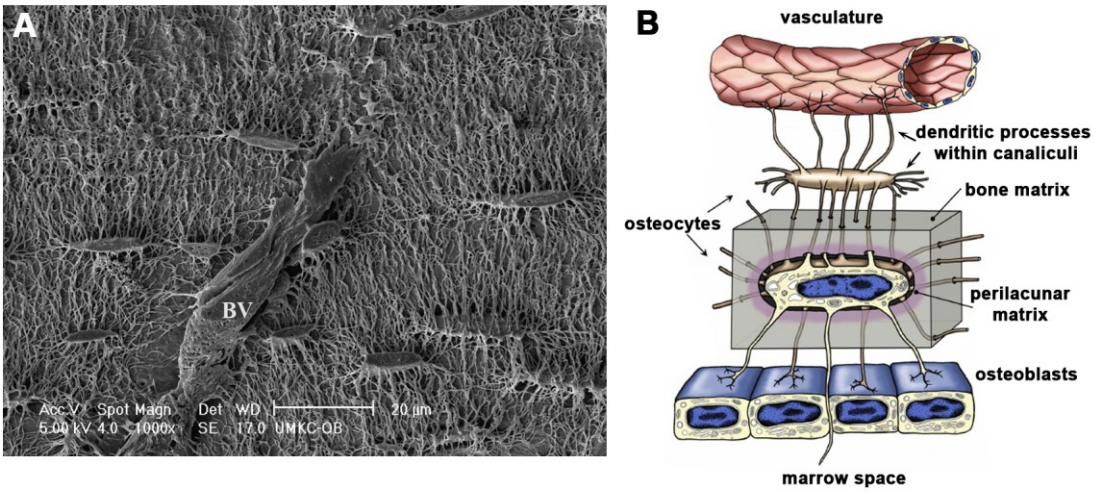

Figure 10: A) Osteocyte LCN associated with a blood vessel; BV = blood vessel (adapted from [10] with permission of John Willey and Sons), B) Scheme of an osteocyte located inside its lacunae and its connections with the surrounding space (adapted with permission of Endocrine Society from [187]; permission conveyed through Copyright Clearance Center, Inc.).

Different studies have suggested the involvement of osteocytes in mechanosensation and mechanotransduction, by demonstrating that mechanical loading activates cellular processes in osteocytes such as energy metabolism, gene activation and growth factor production [188, 189]. Direct demonstration of the involvement of the osteocytes in mechanosensation and mechanotransduction was shown by Tatsumi et al. [190], who reported that osteocyte-ablated mice were resistant to unloading-induced bone loss and moreover presented osteoporotic-type bone. It is, however, not yet clear how the mechanical loading is sensed by the osteocyte, but different mechanisms have been proposed. Mechanical loading has been suggested to induce extracellular fluid flow [191, 192], which results in shear strains on the osteocyte plasma membrane [193-195] or in deformation of the dendrites [196, 197], leading to the activation of intracellular signaling pathways. The fluid flow theory has been supported by *in vitro* experiments, which reveal the larger mechanosensitivity of osteocytes to fluid flow, when compared to osteoblasts and fibroblasts [198]. In addition, osteocytes seem to be more responsive to fluid flow shear stress than to other forms of mechanical strain (like substrate stretching). Alternatively or at the same time, osteocytes are thought to directly sense the local substrate strains. The direct strain sensation theory was initially contradicted by studies in which strain levels correspondent to the strains measured *in vivo* on the bone surface (physiological loading causes strains in the whole bone in the range of 0.04-0.03% and seldom exceed 0.01% [199, 200]), did not stimulate osteoblasts [198, 201]. However, these values represented the

average strain that would act on thousands of osteocytes and provided no information about variations in the local strain field, which are likely to happen due to microstructural inhomogeneities in the bone, such as lacunae and canaliculi. The strain amplification effects at these sites were suggested to occur by different *in vitro* and numerical studies [12, 202, 203]. Recently, a finite element model based on synchrotron X-ray phase nano-tomography showed that the strain applied globally was amplified up to factors of 10 and 70 in the extracellular matrix and in the osteocytes, respectively [203]. In addition, the authors reported that the cell body-dendrite junction was the location of major cell deformations (magnitudes similar to the *in vitro* stimulatory threshold for osteocytes) [204]. A different theory suggests that the recruitment of osteoclasts and initiation of (re)modeling in bone occurs after microdamage of the extracellular matrix and consequent disruption of the canalicular network and osteocyte death [205, 206].

Not only are the mechanical signals that reach the osteocytes not clearly identified, but also how intracellular signaling cascades are initiated and how the mechanical signals are converted into cellular events. It is however, thought that the adhesion proteins integrins, gap junctions and/or stress induced ion channels mediate strain of extracellular matrix to intracellular signaling pathways and that primary cilium might also play a role by sensing fluid flow [207]. Important intracellular mediators of mechanical loading include intracellular calcium signaling, nitric oxide and prostaglandins [207]. It is likely that the osteocytes are able to respond to mechanical stimuli through a variety of sensor and signaling mechanisms.

The perilacunar tissue of the osteocyte

The total lacunar and canalicular surface area in adults is two orders of magnitude greater than the surface directly remodeled by osteoblasts and osteoclasts [208]. The bone tissue, which directly surrounds the osteocyte, the perilacunar tissue, forms a unique environment. The removal of only a few angstroms of mineral per osteocyte would possible lead to significant effects on the levels of circulating ions and also on bone's mechanical properties [182].
Different studies have suggested the osteocyte has the ability to remove mineral from its perilacunar tissue [209]. In 1962, Baud [210] showed by electron transmission microscopy that the lacunar walls of osteocytes had irregular borders, result of osteolytic activity. In 1967, the concept of "osteocytic osteolysis" was introduced by Belanger [211] in association with the finding that the perilacunar mineral surrounding the osteocyte has a greater solubility. Some contemporary studies have also shown that the osteocyte can modify its microenvironment in response to environmental factors. Breeding female snakes during the period of embryo development and hibernating snakes showed significantly enlarged lacunae and a perilacunar area of decreased mineral density, thought to be reminiscent of mineral resorbing activity [212]. This enlargement and removal of mineral from the perilacunar space was also observed in male glucocorticoid-treated and female ovariectomized mice [213]. More recently, Qing et al. [214] suggested the occurrence of the same phenomenon in both the tissue surrounding lacunae and canaliculi in lactating mice. Blaber et al. [215] reported that osteocyte osteolysis occurred in the pelvis of C57BL/6J mice after 15 days of space flight. A small number of studies have

suggested that osteocytes have also mineral apposition abilities. Osteocyte lacunae were shown to uptake tetracycline, indicating the ability to calcify or form bone [216]. Laying hens in calcium repletion after a depletion period, showed increased mineralization, as well as enrichment in collagen fibrils in the lacunae [217].
The osteocyte dendrites might also be involved in removal and replacement of bone mineral, as different studies suggest [11, 208, 214, 218]. The fact that the canalicular surface area is much larger than the lacunar surface area, with more direct access to the mineralized bone tissue, supports this idea. However, due to the small dimensions of the canaliculi the numbers of studies assessing this topic are more limited.

The capacity of osteocytes to remove and add mineral from the tissue surrounding the lacunae and canaliculi might have important implications in mineral metabolism, but also in the local lacuna strain field influencing the osteocyte and its responsiveness to mechanical loading. In fact, it was shown that the amplification of the macroscopic strain applied to a whole bone by the osteocyte lacuna is a function of perilacunar tissue material properties [12]. A decrease in the perilacunar tissue modulus might amplify the perilacunar tissue strain and also canaliculi deformation, while an increase in the modulus might have the opposite effect. Furthermore, aging seems to be accompanied by lacunar hypermineralization [219], which might reduce the strain signal acting on the osteocytes under normal loading conditions and contribute to the progression of osteoporosis.

2.3.3 Mechanical loading effects on bone mineral and matrix properties

Numerous studies have assessed changes in bone mass and/or geometry after exercise and mechanical loading. However, the impact of mechanical loading on bone might not be restricted to changes in mass and geometry, but also to alterations in material quality. In particular, the effect of mechanical loading on the properties of bone's basic constituents, the mineral particles and the collagen matrix is largely unknown.

Pre-clinical and human exercise studies suggest that exercise might lead to an increase in volumetric bone mineral density (assessed with pQCT) [220, 221]. In postmenopausal women, exercise was shown to lead to a reduction in bone loss, possibly by maintenance of trabecular and cortical volumetric bone mineral density [222]. Mechanical loading has been also suggested to impact the collagen matrix through increased collagen synthesis [223] or altered tensional properties of the collagen network [224, 225]. In addition, a series of studies have shown that microgravity might alter bone mineralization and and/or organic matrix composition, leading to deterioration of bone material properties in young rodents [226-229].
Most of the studies analyzing the impact of mechanical loading on bone's mineral and matrix properties did not differentiate between material quality changes in newly formed and pre-existing tissue. However, one study by Kohn et al. [230] used a short-term exercise regime (30 minutes/day of treadmill running for 21 days) in 16 week old C57BL/6 male mice which did not increase bone formation, assessed by histomorphometry. The authors showed loading increased structural and tissue level mechanical properties by altering bone quality of pre-

existing tissue via enhanced mineralization (increased mineral:matrix ratio) and altered mineral composition (decreased carbonate:mineral ratio). One possible mechanism behind the changes in the quality of pre-existing tissue might be the perilacunar and pericanalicular remodeling [208, 209], described in chapter 2.3.2.

The quality of new bone tissue formed with additional mechanical loading has not been yet characterized. Since extra mechanical loading often leads to enhanced mineral apposition rate, the new tissue formed in such conditions could have altered mineral and matrix properties. This is the case in bone tissue formed rapidly via intramembranous ossification during healing [231, 232]. In 1981, Woo et al. [233] analyzed the quantity and quality of femoral bone in immature pigs, which trotted 40 km a week for 12 months. The authors suggested that the new bone tissue formed when bone mass was increased after exercise had similar quality to the original bone. However, the authors could not analyze separately the quality of the new tissue formed with exercise and the pre-existing tissue.

2.3.4 Age-related changes in bone's adaptive response

Different human exercise [145, 234-242] and pre-clinical studies [176, 177, 243-250] indicate that age modulates the adaptive response to mechanical loading.
In general, exercise seems to lead to an increase in bone mass in young individuals [234, 236, 240, 241], while in older individuals it only induces small increases in bone mass or prevents bone loss [237-239, 251, 252]. High impact and high velocity exercise led to an increase in trabecular bone mass in prepubescent girls and premenopausal women [234-236], but only to a marginal increase and a maintenance of bone mass in postmenopausal women [237-239]. Pre-clinical studies showed that loading regimens which were osteogenic in young animals, lost their potential in senescent animals [246] or that the strain magnitude required to engender bone formation in elderly animals was much higher than the one needed in young animals [244]. Adult mice responded anabolically to mechanical loading, but their adaptive response was reduced relative to young mice [249]. The mechanisms behind the reduction in bone's adaptive response to its mechanical environment with aging has been attributed to a reduced capacity of aged individuals to form new bone [67], but also to a non-perception of the stimulus required for bone formation. It is known that with aging different phenomena occur which might contribute to the reduction of bone's mechanoresponsiveness [244, 246, 253, 254], such as a decrease in the populations of osteoblasts, lining cells [255-257], alteration of the levels of circulating hormones and a reduction of basal cell function [258-265]. Additionally, changes in the osteocyte network and in the material properties of the perilacunar tissue could impair the ability of osteocytes to sense and translate mechanical stimuli [219, 266-268], but this is still matter of discussion.
There are, however, some pre-clinical studies which oppose the theory of reduced adaptive bone response with aging and suggest that bone's responsiveness to mechanical loading is not decreased in elderly animals [220, 245, 250, 269-271]. Brodt et al. [270] have reported that the adaptive response in the endocortical surface of the bone was higher in aged than in middle-aged mice, but similar between the two ages in the periosteal surface. A recent study compared

trabecular and cortical bone's adaptive response in 5, 12 and 22 month old C57BL/6 mice and concluded that the response was higher in the young than in the adult and elderly animals, but comparable between adult and elderly mice [272].

The number of studies investigating how age affects the impact of loading on bone mineral and matrix properties is limited. The effect of loading on bone's collagen organic matrix was assessed in decalcified humeri from 2, 4, 6 and 18 month old C57BL/6 male mice, after voluntary exercise (continuous access to a running wheel beginning at age 1 month old) in two separate studies [224, 225]. No difference was measured between running mice and sedentary controls in the collagen content or cross-links (measured via high-performance liquid chromatography). However, exercise led to improved tensional properties of the collagen network in young and growing mice (2 and 4 month old), but not in adult mice (6 month old). The authors attributed the exercise-related improved mechanical properties in the young mice to increased remodeling of the bone, along with increase in the rate of alignment of the collagen fibrils in the longitudinal direction. In 18 month old mice exercise lead to reduced collagen tensile properties, reduced diaphyseal cortical bone mineral density, but increased diaphyseal cortical bone stiffness. Nevertheless, the authors could not establish a direct comparison on how age (2, 4, 6 and 18 month old mice) influenced the effect of exercise on bone composition, as the duration of exercise for each group was different (1, 3, 5, and 17 months of voluntary exercise, respectively). Some additional studies have speculated on the age-modulated effects of mechanical loading on bone mineral and matrix properties, after analyzing changes in bone's mechanical properties with exercise. Huang et al. [273] showed that endurance running lead to an increase in femur's ultimate toughness and post-yield toughness in old rats, but not in growing rats. They have associated the changes detected in old rats with alterations in bone's collagen orientation with loading. Raab et al. [271] also compared the effect of exercise on young and old rats and detected higher ultimate femoral stress only in the old rats, when compared to sedentary controls.

The majority of the studies assessing changes in adaptive response of bone to loading with aging used models such as voluntary exercise which may have included varied levels of physical activity between animals and did not allow for controlled loading conditions, such as strain or load-matched comparisons between age groups. However, the number of studies analyzing bone's adaptive response by using controlled non-invasive extrinsic animal loading models (described in chapter 2.3.1), has been increasing in recent years [247, 249, 270, 272].

3 Materials and methods

3.1 Animal handling

Female young postpubescent 10 week old, adult 26 week old and elderly 78 week old C57BL/6J mice were received and acclimatized at the Institute's animal core facility during the course of the experimental procedure. The animals were group-housed in cages with *ad libitum* access to water and a maintenance diet in a 12:12 hour light/dark cycle. Body weight was measured every day, except during the weekends. All animal experiments were carried out according to the policies and procedures approved by the local legal research animal welfare representative (LAGeSo - Landesamt für Gesundheit und Soziales Berlin, G0333/09).

3.2 *In vivo* loading

3.2.1 *In vivo* load-strain calibration (strain gauging)

The relationship between applied compression and bone tissue deformation for the right and left tibiae of 10, 26 and 78 week old female C57BL/6J mice (n = 7/age) was determined. The aim was to obtain the applied load, which elicited a strain of 1200 με (osteogenic) at the medial midshaft of the tibia. Single element strain gauges (EA-06-015LA-120, Micromeasurements, Wendell, USA) were prepared and attached to the medial surface of the tibial midshaft in alignment with the bone's long axes [274] (Figure 11). A range of dynamic compressive loads, with peak loads varying from -2 to -12 N, were applied to the mice under anaesthesia (ketamine 60 mg/kg and medetomidine 0.3 mg/kg) using an *in vivo* loading device (Testbench ElectroForce LM1, Bose, Framingham, USA), with simultaneous load and strain recording (WinTest software). After measurement, the slopes of the strain-load regressions were calculated.

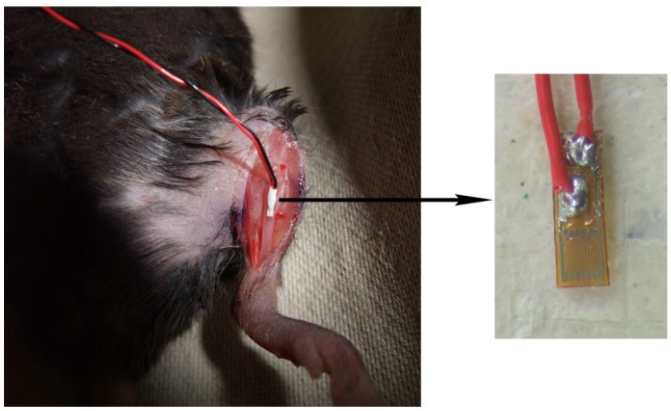

Figure 11: Photograph of a strain gauge positioned at the medial surface of the tibial midshaft of a 10 week old C57BL/6J mouse (left) and an isolated strain gauge (right).

3.2.2 *In vivo* loading protocol

Cyclic compressive loading was applied on the intact left tibia of 10, 26 and 78 week old mice, using an *in vivo* loading device (Testbench ElectroForce LM1, Bose, Framingham, USA). The right tibia of the mice was used as an internal control. The loading device includes an electromagnetic linear displacement actuator controlled by WinTest software, which applies loads to the tibia at the foot, and it incorporates a feedback loop to keep consistent load magnitudes. The applied loads were measured by a load cell, which is in series with the tibia and the actuator.

The mouse's left flexed knee and ankle were placed into the concave cups of the loading device (Figure 12, Figure 9C) and the tibia was held in place by applying a continuous static pre-load of -1.0 N, immediately before the dynamic loading. Loading parameters included: 216 cycles applied daily at 4 Hz, 5 days/week (Monday - Friday), for 2 weeks, delivering -9 N (78 week old mice) or -11 N (10 and 26 week old mice) peak loads. The triangle waveform applied consisted of 0.15 seconds of symmetric active loading/unloading with 0.1 seconds rest insertion (at -1 N) between load cycles and a 5 seconds pause between every four cycles. During the loading period, mice were anesthetized with isofluorane inhalation (2.5% in 1L/min O_2), except mice scanned with *in vivo* microCT, who were injected at days 0, 5 and 10 of the experiment with an anesthetic/analgesic cocktail of 60 mg/kg ketamine and 0.3 mg/kg medetomidine. Between the loading sessions, mice were allowed unrestricted cage activity. At day 15, 3 days after the last loading session, mice were sacrificed under anesthesia (ketamine 60 mg/kg and medetomidine 0.3 mg/kg) through an overdose of potassium chloride. After sacrifice, both the left and right tibiae of the animals were dissected from the surrounding soft tissues.

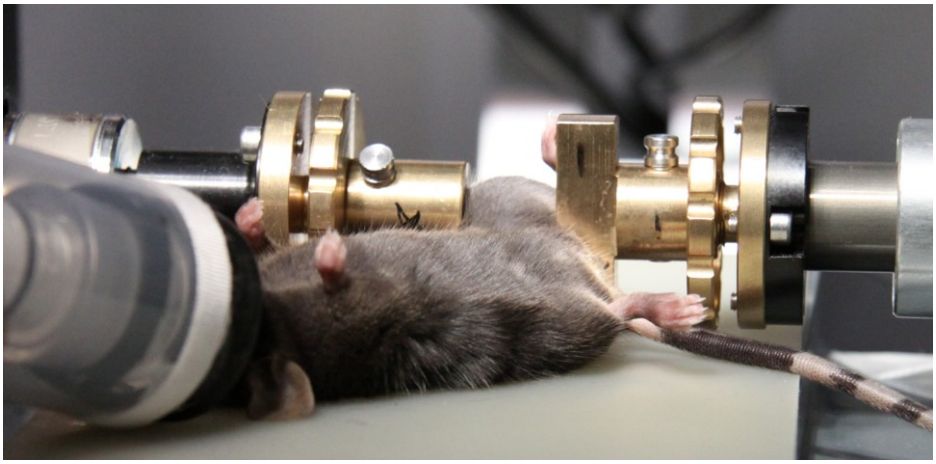

Figure 12: Photograph of a 10 week old C57BL/6J mouse undergoing *in vivo* loading of the left tibia.

3.3 Measures of bone mass and geometry

MicroCT is a non-destructive imaging technique with which high-resolution 3D images of internal structures of an object can be obtained. Its basic principle relies on the interaction of X-rays with matter, which during a microCT scan is dominated by the photoelectric effect. This

effect causes the attenuation of X-rays while passing through matter and this attenuation is dependent on the atomic number of the specimen in study [275]. The sum of all local attenuations along the X-ray beam results in a 2D X-ray projection of the specimen. By either rotating the specimen or the X-ray source, a set of 2D projections from multiple viewing angles are acquired and a final 3D image is obtained. MicroCT is extensively used in the study of bone, since there is an excellent contrast between mineralized bone and the surrounding soft tissues (due to the difference in their atomic numbers). *In vivo* microCT, in particular, is used to longitudinally study and track the changes occurring in bone, for example, in the time scale of weeks [276]. In this work, by scanning the same animal at different time points, the longitudinal effect of aging and of *in vivo* loading on cortical bone mass and geometry was studied. Dynamic histomorphometry provided us with complementary information on bone's remodeling rates, data that is not possible to obtain, at least directly with microCT. Both *in vivo* microCT and dynamic histomorphometry were performed together with the other group members.

3.3.1 *In vivo* micro-computed tomography (microCT)

Longitudinal *in vivo* microCT (vivaCT 40, Scanco Medical, Brüttisellen, Switzerland) was performed at day 0, 5, 10 and 15 of the experiment to assess cortical bone in 10, 26 and 78 week old mice. MicroCT scans were performed on the left (loaded) and right (control) tibiae of the mice (n = 7 mice/age) (Figure 13). Additional mice were loaded (n = 4 mice/age) for two weeks and imaged only at day 15. Scans were run at 55 KVp, 145 µA and 600 ms integration time, with an isotropic voxel size of 10.5 µm.

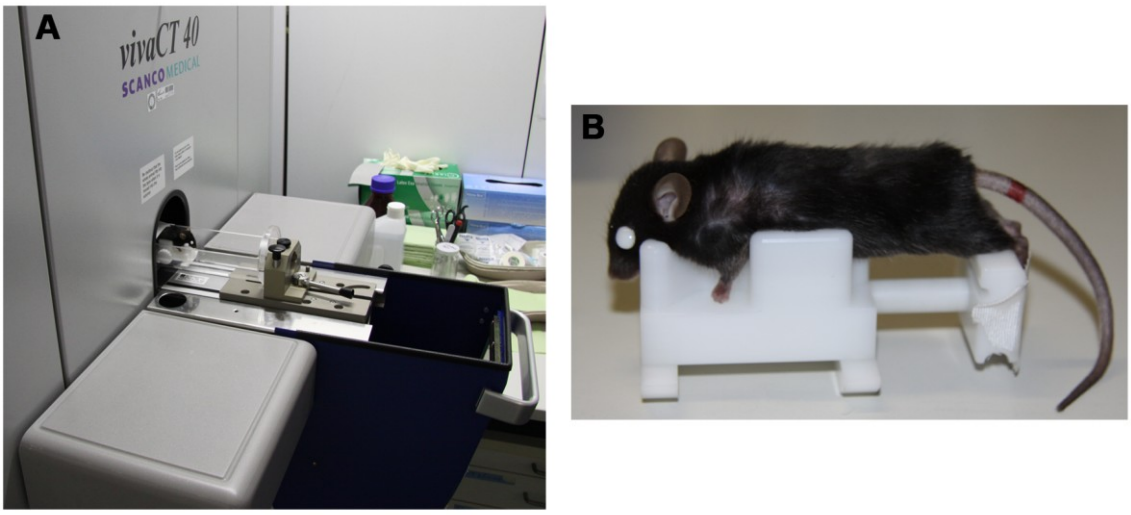

Figure 13: A) Photograph of a C57BL/6J mouse inside the *in vivo* microCT, **B)** Photograph a C57BL/6J mouse placed in a costume-made "microCT mouse bed".

The microCT volume of interest selected to study cortical bone was centered at the tibial midshaft and extended along the bone's long axis 2.5% of the tibia length (Figure 14). Cortical bone was segmented with a global threshold of 4446 HU (813 mg HA/cc). The outcome parameters were obtained using Scanco software and included: principal moments of inertia

(Imax, Imin), cortical bone area = cortical volume/(number of slices x slice thickness) (Ct.Ar), total cross-sectional area inside the periosteal envelope (Tt.Ar), cortical area fraction (Ct.Ar/Tt.Ar), cortical thickness (Ct.Th) and cortical volumetric tissue mineral density (Ct.vTMD), as recommended [276].

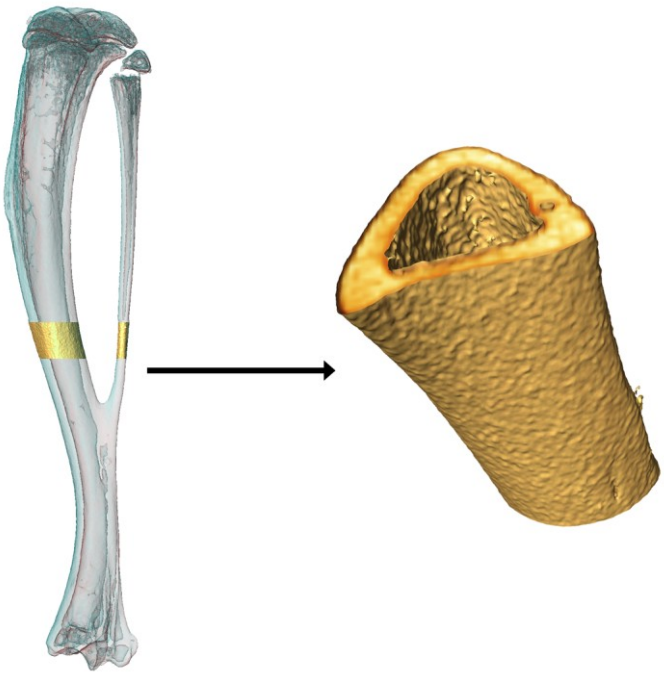

Figure 14: Cortical bone analyzed with microCT at the tibial midshaft of a C57BL/6J mouse. The length of the tibia is approximately 17 mm.

3.3.2 Dynamic histomorphometry

At day 3 and 12 (3 days before the sacrifice of the animals) of the *in vivo* loading experiment, each mouse was administered, via intraperitoneal injection, with the fluorochrome label calcein at a dose of 30 µg/g. At day 15, their tibiae were collected, fixed in 100% ethanol, cleared in xylene, infiltrated and embedded in polymethyl methacrylate (PMMA). Transverse sections with a final thickness of approximately 20 µm were prepared to analyse the calcein labels at the cortical bone at the midshaft (n = 5-10/age). These sections were imaged and analysed with a fluorescent microscope (Leica DMRB, Munich, Germany and AxioCam MRc, Zeiss, Oberkochen, Germany) at a magnification of 200x (Figure 15). Outcome parameters were: single- and double-labeled surface per bone surface (sLS/BS, dLS/BS), mineralizing surface (MS/BS), mineral apposition rate (MAR) and bone formation rate (BFR/BS), which were analyzed as recommended [277]. MAR (µm/day) was obtained by dividing the distance between midpoints of the consecutive labels by 9, the number of days between the two calcein injections. MS/BS, the extent of actively mineralizing surface per bone surface at the time of calcein label administration, was calculated as the length of the double-labeled perimeter plus one half the length of the single-labeled perimeter (0.5 x sLS + dLS). BFR/BS was calculated as the product

of MAR and MS/BS. For cortical bone, the entire endocortical (Ec.) and periosteal (Ps.) surfaces were measured.

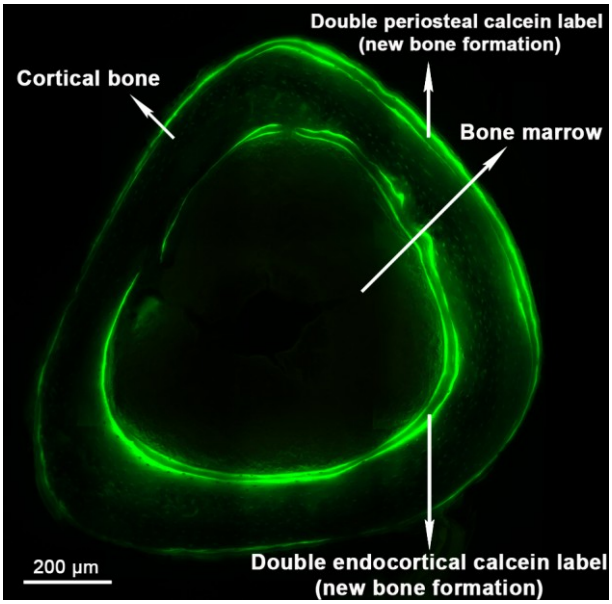

Figure 15: Fluorescence microscopic image of a tibial cross-section of a C57BL/6J mouse. Calcein labels which allow tracking new bone formation can be seen in green color.

3.4 Measures of bone mineral and matrix properties

3.4.1 Scanning small angle X-ray scattering (sSAXS)

SAXS is one of the possible results of interaction between X-rays and matter. It is characterized by diffuse elastic scattering of a primary X-ray beam at scattering angles of up to 5^0. SAXS occurs when the exposed sample is composed of phases with different electron densities with sharp interfaces between each other, where the sub-volumes are in the range of 1 nm up to 1 µm [278]. This is the case in bone, which is considered as a two phase system with a high electron density phase, the mineral particles and a low electron density phase, the collagen-rich organic matrix. Information on bone's mean mineral thickness (T parameter) and degree of mineral alignment (ρ parameter) can be derived from the resulting scattering patterns, in particular from the scattering intensity distribution in function of the length of the scattering vector $\vec{q}$ or the azimuthal angle χ. The scattering vector is defined as:

$$\vec{q} = \vec{k} - \vec{k'}$$

where $\vec{k}$ is the wave vector of the incident beam and $\vec{k'}$ the wave vector of the scattered beam (Figure 16), with

$$|\vec{k}| = |\vec{k'}| = \frac{2\pi}{\lambda}$$

for elastic scattering. The length of the scattering vector is related to the scattered angle and defined by the formula:

$$|\vec{q}| = 2k.\sin\theta = \frac{4\pi}{\lambda}.\sin\theta$$

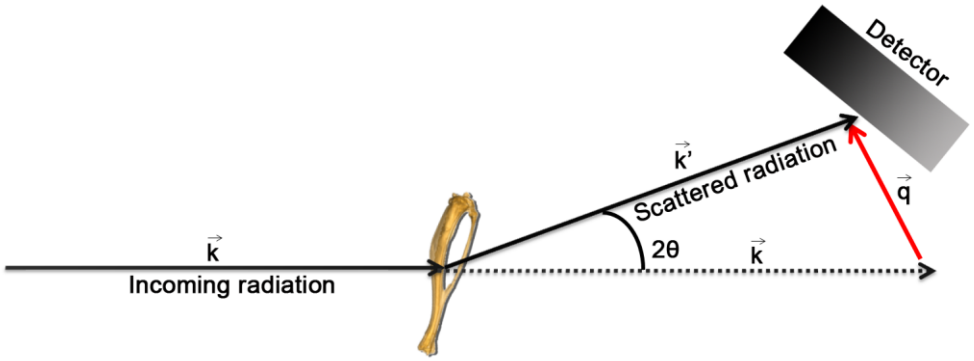

Figure 16: Scheme of the SAXS principle: the incident beam with wave vector $\vec{k}$ is transmitted through the sample and scattered with wave vector $\vec{k'}$. The scattering vector is represented as $\vec{q}$.

The T parameter, bone's mean mineral thickness can be defined as:

$$T = \frac{4\Phi\,(1-\Phi\,)}{\sigma}$$

where Φ is the volume of mineral per tissue volume and σ the surface area of mineral per tissue volume [37]. For thin platelet mineral crystals where the volume fraction of the mineral phase is 0.5, T is a measure of the particles smallest dimension, the mineral thickness (Figure 17A). The ρ parameter corresponds to the degree of alignment of the mineral particles within the plane perpendicular to the primary X-ray beam (Figure 17B). The detailed description of the ρ parameter is provided later in this chapter.

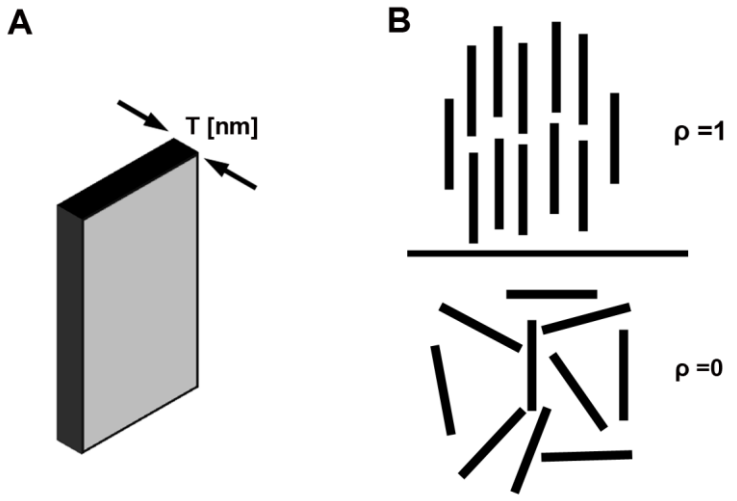

Figure 17: A) T parameter corresponds to mean mineral thickness, B) ρ parameter varies between 1 (perfectly aligned mineral particles) and 0 (randomly oriented mineral particles).

In scanning SAXS (sSAXS), a specimen is moved stepwise in directions perpendicular to the X-ray beam and in each step the scattering patterns are recorded. This allows detection of local changes in bone's mineral properties, which can vary on the micrometer length scale [37].

sSAXS with synchrotron radiation was used in this work to study bone's nanoscale mineral properties in a position-resolved way.

Sample preparation for sSAXS

The right (control) and left (loaded) tibia of six 10, 26 and 78 week old mice (n = 2 mice/age) were studied with synchrotron sSAXS. A region at the midshaft of the tibiae (125-300 µm x 30-77.5 µm) was examined and three regions of interest within the midshaft were studied: periosteal, endocortical, and intracortical regions (Figure 18). Based on the calcein labeling of the mice studied and the high resolution of the method, the periosteal and endocortical regions were defined as regions with a width of approximately 10 µm starting from the respective borders of the bone. Intracortical region included all the bone tissue starting 40 µm away from the bone borders, to assure a separation from the endocortical and periosteal regions.

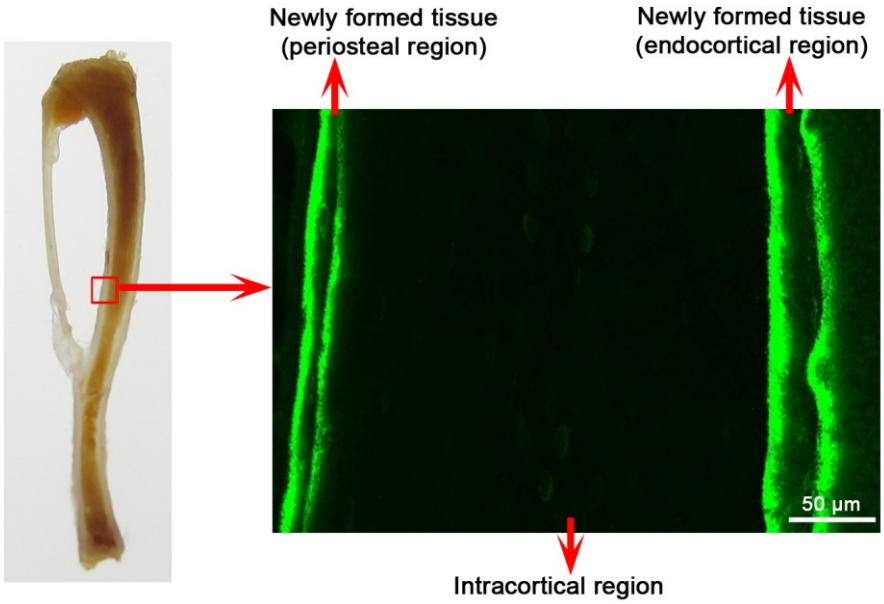

Figure 18: Region at the tibial midshaft (inside red box) measured with sSAXS (left) and the three studied regions of interest: intracortical, endocortical and periosteal (right).

After the *in vivo* loading experiment, the tibiae were fixed in 100% ethanol, cleared in xylene, infiltrated and embedded in PMMA. Ten micron thick sections were cut in a direction parallel to the longitudinal axis of the long bones with a microtome (Leica SM2500S; knife: Leica VMH 400, Nussloch, Germany). All the sample preparation was performed under water-free conditions, which is thought to be effective in preserving bone mineral [279]. The common water based solutions used to moisture the blade or to straighten the cut samples during microtome cutting were not used. Instead, a filtered solution of double distilled water saturated with calcium phosphate powder was used. Due to its saturation, the prepared solution avoided the mineral dissolution of exposed surfaces.

Before the sSAXS measurement, the tibial sections were framed with a lead tape and placed on a magnetic sample holder. The sections were sequentially imaged with fluorescence microscopy, measured with sSAXS and finally imaged with BSE imaging.

sSAXS data acquisition

The sSAXS measurements were performed at the Nanofocus beamline (ID 13) at the European Synchrotron Radiation Facility (ESRF, Grenoble, France) (Figure 19). A monochromatic high energy (15 keV) X-ray beam with a wavelength of 0.0812 nm and a diameter of 1 µm was incident to the tibial sample, which was placed at approximately 540 mm from the detector. The sample was attached to a sample holder magnetically mounted onto the sample stage, which was translated in the yz direction, perpendicular to the incident beam. Through the use of a long-distance optical microscope, sample scan locations were defined. The sSAXS patterns were acquired with an ESRF FReLoN detector with an active area of 2048 x 2048 pixels and a pixel size of 51.7 x 51.5 μm^2. A detector binning of 4 was used, which corresponded to a pixel size of 206.9 x 206.2 μm^2. The exposure time was set between 0.6 and 0.8 seconds and the scans were performed with a step size of 1 µm between the measured points, resulting in the collection of a maximum of 20000 sSAXS intensity patterns per sample. For the position calibration of the X-ray beam at the sample position, a silver behenate (AgBh) standard was used.

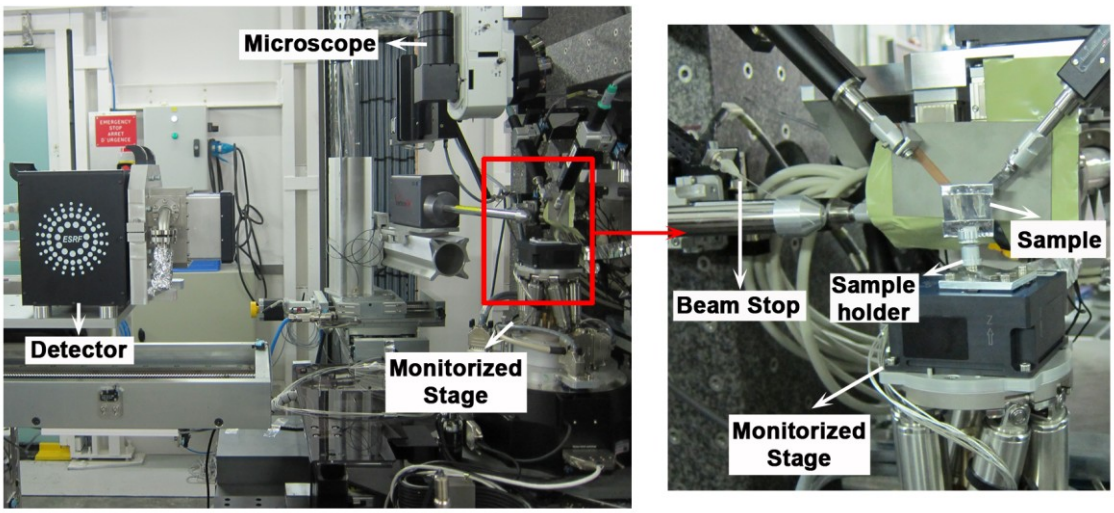

Figure 19: Experimental setup for synchrotron sSAXS measurements at the ESRF.

sSAXS data correction

The beam center position and the exact sample-to-detector distance were calculated from the diffraction patterns of the standard silver behenate (AgBh) with the software Fit2d [280] and Autofit (custom-made software, C. Li, Max Planck Institute of Colloids and Interfaces, Potsdam-Golm, Germany).

All the 2D sSAXS patterns were corrected for dark current (charged-couple device (CCD) readout noise) and rescaled for beam intensity fluctuations during measurements. In addition, absorption effects in the sample and the consequent need to rescale the measured scattering intensities were considered by determining the transmission coefficients at each measuring point, for one of the samples. The ratio between transmitted intensity of the sample and the intensity of the direct beam without the sample (empty beam), both measured with a photodiode, was calculated. Since the coefficient of transmission was close to 1 (mean value = 0.987±0.014) for all the points (including points at border regions), its value was set to 1 for all the measured samples. Finally, to minimize the background scattering, the intensity of the empty beam measured with the detector was subtracted to the rescaled scattering intensity for each sample. The final corrected scattering intensity at each measuring point was calculated automatically with Autofit, following the formula:

$$Icorrected = \frac{Isample}{t} - Iempty\ beam$$

where t is the correction factor for absorption effects and beam intensity fluctuations during measurements.

sSAXS data analysis

The obtained 2D sSAXS patterns were radially and azimuthally integrated to a function I(q) and I(χ), respectively, being I the scattering intensity, q the scattering length and χ the azimuthal angle. The radial intensity profiles were obtained by binning all pixel values from the detector with the same radial distance to the beam center, while the azimuthal intensity profiles were obtained by binning all pixels at the same azimuthal degree with respect to the zero direction. These calculations were performed with Autofit.

The T parameter, mean mineral particle thickness in the scattering volume, was derived from the resulting sSAXS intensity function I(q). The calculation was performed with Autofit, based on Porod's law (valid for two phase-like systems such as bone), which states that the scattering intensity decreases with q^{-4}. T is defined as:

$$T = \frac{4}{\pi P}\int_0^\infty q^2 I(q)dq$$

where P is the Porod constant, which can be obtained from the $Iq^4(q^4)$ curve, the Porod plot (Figure 20A) as the intercept of the fit of the linear region with the y-axis. The integral is solved by determining the area under the function $Iq^2(q)$, the so-called Krakty plot (Figure 20B). However, this calculation requires some approximations for small and large q values, for which

scattering intensity can't be obtained directly from the measurement. The first approximation consists in considering the Krakty plot linear for small q values and the second approximation considers the scattering intensity proportional to q^{-4} for large q values. The area under the Krakty plot can now be calculated by the sum of the three different areas depicted in the plot (Figure 20B):

$$\int_0^\infty q^2 I(q)dq = \int_0^{qKrakty,min} q^2 I(q)dq + \int_{qKrakty,min}^{qPorod,min} q^2 I(q)dq + \int_{qPorod,min}^\infty q^2 I(q)dq$$

where $q_{Krakty,min}$ is the smallest accessible q value and $q_{Porod,min}$ the starting value for the approximation I(q) proportional to q^{-4}. The formula can be reduced to:

$$\int_0^\infty q^2 I(q)dq = \frac{qKrakty,min}{2} I(qKrakty,min) + \int_{qKrakty,min}^{qPorod,min} q^2 I(q)dq + \frac{P}{qPorod,min}$$

where the first term corresponds to A_1, the second to A_2 and the third to A_3 in Figure 20B. This way and by defining the different parameters (for the studied bone samples)—$q_{Krakty,min}$ was set to 0.3 nm^{-1}, $q_{Porod,min}$ was defined as 2 nm^{-1} and $q_{Porod,max}$ as 3 nm^{-1}—the total area was calculated and finally the T parameter too.

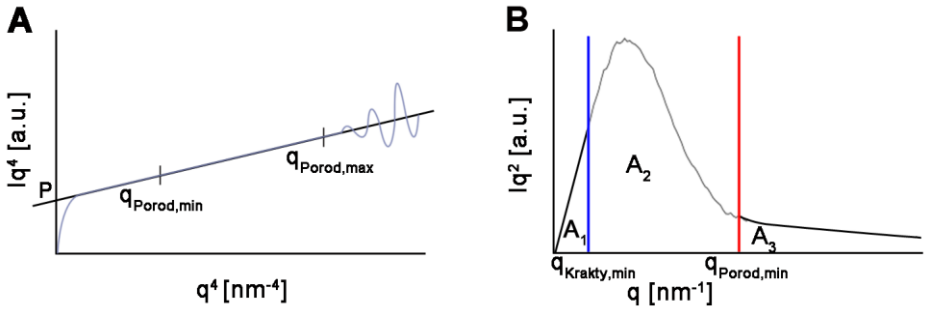

Figure 20: A) Porod and B) Krakty plot obtained from radially integrated sSAXS patterns. A_2 is obtained from real data, while A_1 and A_3 are obtained through approximations; P is the Porod constant.

The ρ parameter, the degree of alignment of the mineral particles was obtained with Autofit. The calculation was based on the azimuthal plot I(χ) which has two peaks separated by 180°, which were fitted into two Gaussian functions. The ρ parameter was defined as:

$$\rho = \frac{A1 + A2}{A1 + A2 + A0}$$

where A_0 is the total sSAXS intensity caused by randomly oriented particles and A_1 and A_2 the sSAXS intensity caused by particles aligned parallel to a certain direction (Figure 21).

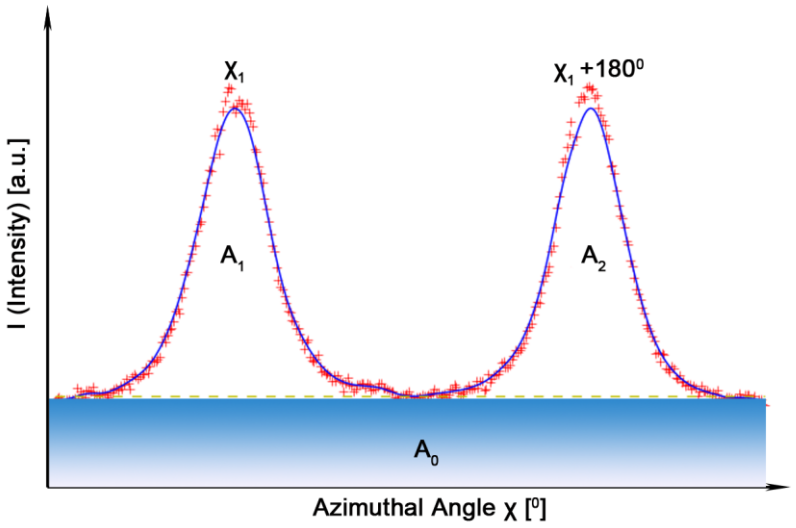

Figure 21: Azimuthal plot I(χ) of the scattering intensity. The real data points are in red and the blue line represents the fitting Gaussian function. A_1 and A_2 correspond to the fraction of aligned mineral particles and A_0 represents the fraction of randomly aligned mineral particles.

For a perfect alignment of minerals crystals ρ = 1 and the sSAXS pattern was a narrow line perpendicular to the long axis of the mineral particles. For randomly oriented minerals, ρ = 0 and the sSAXS pattern was circular (Figure 17B). All other mineral particles configurations resulted in elliptical sSAXS patterns. The detailed calculation of the T and ρ parameters has been previously described [37, 110, 281]. Using the software OriginPro 9.0 (OriginLab, Massachusetts, USA) two-dimensional contour maps were obtained for the T and ρ parameters, in order to visualize their spatial distribution in a region within the tibial midshaft (Figure 22).

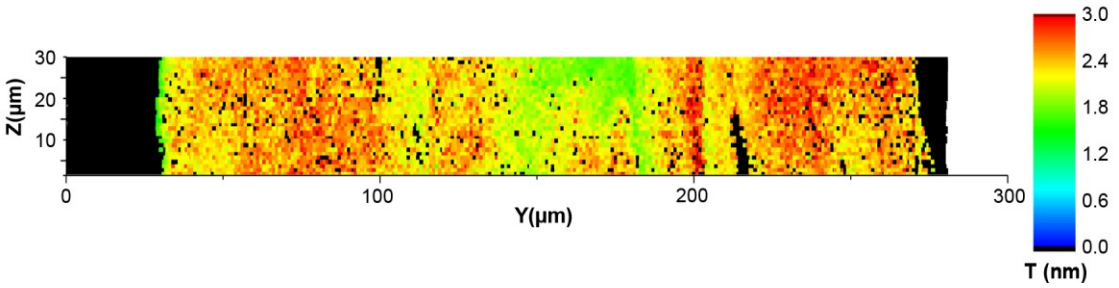

Figure 22: Two-dimensional contour map of the T parameter at the tibial midshaft of one C57BL/6J mouse (plotted with OriginPro 9.0).

3.4.2 Backscattered electron (BSE) imaging

In scanning electron microscopy, a focused beam of electrons scans across the surface of a specimen. These electrons can interact with the electrons and nuclei of the specimen in two different ways: inelastic and elastic scattering of the primary electrons. BSE electrons result from elastic scattering and their detection gives us information on the atomic composition of the scanned area. The gray levels in the BSE images are based on the atomic number of the

elements present in the scanned area. For bone tissue, the BSE signal is dominated by calcium atoms. In the BSE images of bone tissue, regions of high mineral content appear more light grey and regions of low mineral content appear more dark grey [25]. In this work, BSE imaging was used to obtain a qualitative overview of the mineral content and to pre-characterize entire bone specimens, before measuring the bone tissue in more localized regions with other techniques.

Sample preparation for BSE

After performing sSAXS, the right (control) and left (loaded) tibia of six loaded 10, 26 and 78 week old mice (n = 2 mice/age) were imaged with the scanning electron microscope (SEM) in BSE mode.
In addition, the loaded tibia of one 26 week old mouse was collected after the *in vivo* loading experiment, fixed in 100% ethanol, cleared in xylene, infiltrated and embedded in PMMA. The embedded sample was initially ground in a polishing wheel (PM5, Logitech, Glasgow, Scotland) with abrasive silicon carbide papers of decreasing particle size and after polished with a diamond suspension also of decreasing particle size (3, 1, 0.25 μm). The tibia was imaged with the SEM in BSE mode. Following SEM analysis the tibia was analysed with nanoindentation.

Measurement and analysis

The tibial samples were imaged with an environmental SEM (FEI FEG-ESEM Quanta 600, FEI Company, Hilsboro, OR, USA) in BSE mode, under low vacuum (0.8 Torr). An operating voltage of 12.5 kV was used and the working distance was set to 10 mm.

3.4.3 Correlation of images

As previously described, the loaded and control tibiae of the mice subjected to *in vivo* loading, were imaged before the sSAXS measurement, with fluorescence and after with BSE microscopy. The overview images of the entire tibia obtained with fluorescence and BSE microscopy were overlaid, after adequate rescaling. The same was done for the magnified fluorescence and BSE images of the regions at the tibial midshaft (Figure 23) which were measured with sSAXS. The images collected using the multiple methods were overlaid onto each other to correlate the degree of mineralization and calcein label location with sSAXS maps of mean mineral thickness and degree of mineral alignment from the same regions. This way, T and ρ parameter's values were related to areas of formation of new bone tissue and to specific patterns in the bone, such as blood vessels.

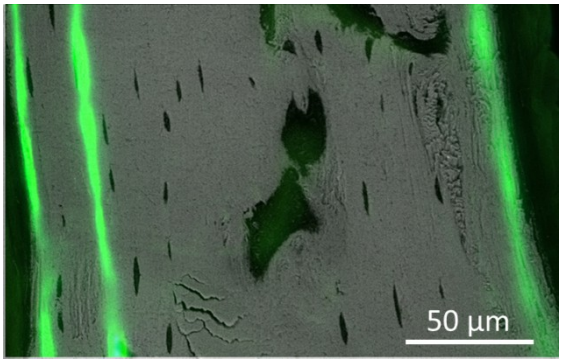

Figure 23: Merged BSE and fluorescence image at the tibial midshaft of a C57BL/6J mouse.

3.4.4 Multiphoton confocal microscopy

Multiphoton microscopy is a microscopy technique, which uses nonlinear light-matter interactions (less sensitive to scattering), involving multiple photons, to generate signal contrast [282]. It includes second harmonic generation imaging, in which an intense laser light passes through a material with a noncentrosymmetric molecular structure. Collagen can produce second harmonic generation signals [283]. In this work, second harmonic generation by multiphoton microscopy was used to obtain a qualitative overview of the collagen structure at the tibial midshaft of young mice.

Measurement

The loaded tibial samples of the 10 week old mice which were measured with sSAXS (the left-over PMMA blocks from the prepared sections for sSAXS measurements), were imaged with the confocal microscope Leica TCS SP5 II (Leica Microsystems, Wetzlar, Germany), which is equipped with a Mai Tai HP multiphoton laser and a 25x water immersion objective. The emitted light from the sample was detected with an internal photomultiplier detector. Second harmonic generation excitation wavelength was set at 910 nm and detection wavelength at 455 nm.

3.4.5 Fourier transform infrared imaging (FTIRI)

FTIRI is an imaging technique based on vibrational spectroscopy, which gives a “molecular fingerprint” of a sample. It is a well-established method in the bone field, where it is used to characterize the chemical composition of bone tissue [284]. Chemical bonds undergo vibration, which includes different types of motions of the atomic groupings within a molecular framework. If when illuminated with infrared (IR), a certain motion is accompanied by a change in dipole moment, it will absorb a specific IR frequency. FTIR absorption spectra are rich in information on bone’s IR active components: phosphate, carbonate, protein and sugars. In fact, bone’s mineral and collagen produce intense IR absorption bands that are characteristic of specific types of chemical bonds within the tissue (Figure 24). FTIRI relies on the usage of a FTIR microscope in combination with an IR focal plane array detector. With this imaging technique, 2D images are obtained, where the x and y axis are the spatial coordinates of the bone tissue section and the z axis the parameter directly measured (intensities or areas) or calculated (area

or intensity ratios). The first application of FTIRI to bone was in 1998 [285] and since then different parameters have been derived from the obtained spectra. These parameters were validated and correlated with bone's mechanical properties and fracture risk [28, 286-288]. For example, mineral:matrix ratio correlates with ash weight, collagen maturity relates to variations in collagen cross-linking and crystallinity varies with the size and perfection of mineral as determined by X-ray diffraction line broadening.
In this work, FTIRI was used as a tool to research into the compositional changes of bone in response to mechanical loading, as well as age related changes in bone's composition.

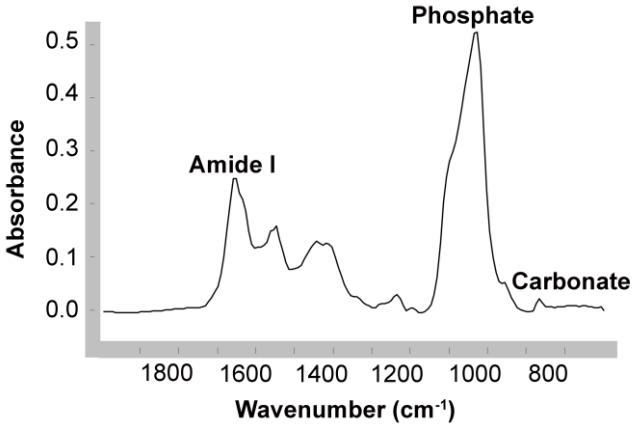

Figure 24: Typical FTIRI spectrum of cortical bone.

Sample preparation for FTIRI

FTIRI was performed on the right (control) and left (loaded) tibia of fifteen 10, 26 and 78 week old mice (n = 5 mice/age), which were a subset from the larger group of loaded mice subjected to *in vivo* microCT and dynamic histomorphometry. Three regions of cortical bone—periosteal, endocortical, and intracortical—at the posterior side of the midshaft of the tibia were analyzed. The posterior side was chosen based on a finite element model study indicating higher compressive strains in this region [289]. Based on the histomorphometry data and the resolution of FTIRI, periosteal and endocortical regions were defined as having a width of approximately 20 μm starting from the respective borders of the bone. The intracortical region included all the bone tissue within a 50 μm region, centered within approximately the middle of the bone.
Thin cross sections of the tibial midshaft were obtained from the embedded PMMA blocks left over after the sample preparation for dynamic histomorphometry. Sections with 2.5 μm thickness were microtomed (Leica SM2500S; knife: Leica VMH 400, Nussloch, Germany), placed between two Kisol-foils and stabilized between two glass slides. They were finally transferred and mounted on barium fluoride infrared windows for FTIRI. Before the measurement, each sample had been imaged with bright field and fluorescence microscopy.

Measurement and analysis

Our collaborators, the research group of Dr. Adele Boskey, who pioneered the techniques' use in studying bone, performed the FTIRI measurements at the Hospital of Special Surgery in New

York. The three defined regions of interest (periosteal, endocortical, and intracortical regions) at the tibial midshaft were analyzed with a Spectrum Spotlight 300 Imaging System (Perkin Elmer Instruments, Shelton, CT, USA) in transmittance mode at a spectral resolution of 4 cm^{-1} and a spatial resolution of 6.25 µm. The spectra obtained were base-lined and the contribution of PMMA was subtracted with ISYS software (Spectral Dimensions, Olney MD). By calculating non-dimensional ratios, different spectroscopic parameters were quantified. Mineral:matrix ratio, which relates with the amount of mineral present, was calculated by integrating the area under the apatite phosphate peak (916-1180 cm^{-1}) and normalizing this relative to the collagen (amide I) peak (1590-1712 cm^{-1}). Carbonate:mineral ratio, which reflects the level of carbonate substitution in the mineral particles, was obtained by integrating the area of the carbonate peak (852-890 cm^{-1}) and normalizing it to the phosphate band (916-1180 cm^{-1}). Crystallinity, which relates with the size and perfection of the mineral particles, was calculated as the peak intensity ratio of the subbands 1020 and 1030 cm^{-1}, within the broad phosphate contour. Collagen maturity was estimated by the intensity ratio of amide I subbands 1660 and 1690 cm^{-1}. Acid phosphate content, the level of acid phosphate substitution in the mineral particles, was calculated as the peak height ratio of the subbands 1096 cm^{-1} and 1128 cm^{-1}. Data was summarized as the parameters means and standard deviations. Apart from single spectra, a colour-coded image of the distribution of each FTIRI spectroscopic measurement was obtained.

3.5 Osteocyte lacuno-canalicular network (LCN) topology and associated perilacunar material properties

3.5.1 Confocal laser scanning microscopy (CLSM)

Visualization and quantification of the osteocyte LCN in bone samples can be achieved by staining the network with the fluorescent dye rhodamine and by scanning the samples with confocal laser scanning microscopy (CLSM) [290]. Rhodamine diffuses throughout the osteocyte LCN, as well as through blood vessels, binding to cell membranes and mineral edges, allowing visualization of even the smallest structures of the network, the canaliculi with diameters as small as 100 nm. In this work, rhodamine staining and CLSM were used to study the topology of the osteocyte LCN in the newly formed of the loaded and control tibiae of young 10 week old mice.

Sample preparation

Both the left (loaded) and right (control) tibiae of 10 week old mice (n = 3 mice/age) were stained with rhodamine and imaged with CLSM. The tibiae were initially fixed in 100% ethanol. To allow rhodamine diffusion through the entire bone sample, the tibiae were cut longitudinally into two halves (Figure 25B) prior to staining. This was achieved by fixing the samples on sample holders with dental glue and cutting them with a diamond saw (IsoMet Low Speed Saw, Buehler, Illinois, USA). The resulting two halves of the tibiae, in contrast with the bulkier entire tibiae, allow the penetration of the rhodamine. After cutting the tibia into two halves and xylene clearing, the staining took place at the same time as the embedding procedure, to avoid the blocking of the voids such as blood vessels and the osteocyte LCN with PMMA before the

staining. The procedure was based on the one previously developed [290], but adapted to the commercially available PMMA (Technovit 9100, Heraues Kulzer, Wehreim, Germany). Rhodamine 6G (Sigma-Aldrich, Missouri, USA) was dissolved (0.002% wt.) in pre-infiltration and infiltration solutions, which were prepared according to the manufacturer's instructions. The tibiae were placed inside the prepared pre-infiltration solution for one day and inside two infiltration solutions for 7 days (Figure 25C). Finally, PMMA embedding medium was poured into plastic containers where the tibial samples were placed in and these were kept at +4 ^{o}C for 24 hours to achieve hardening (Figure 25D). The embedded samples were finally ground and polished, following the procedure described in chapter 3.4.2.

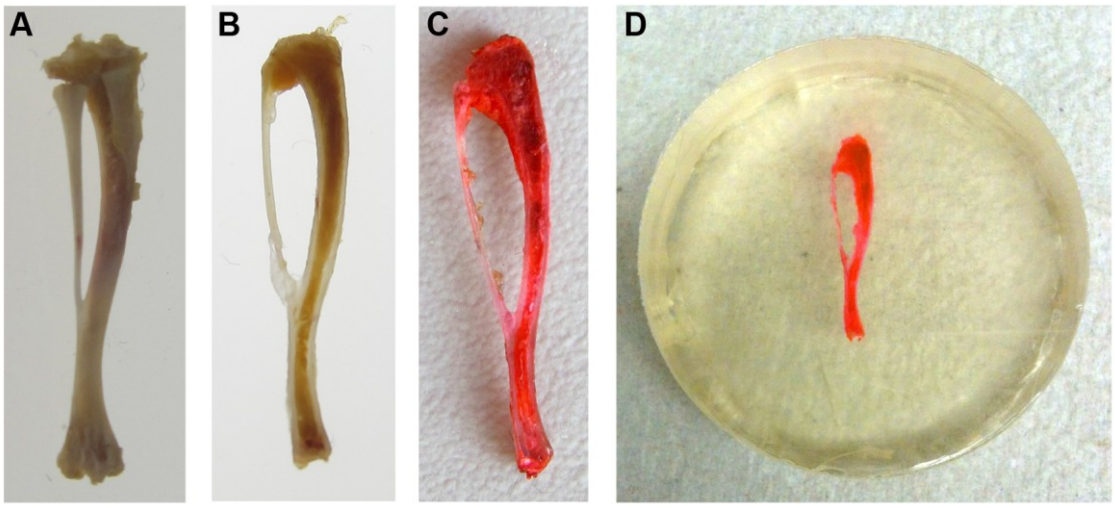

Figure 25: Photographs of the tibia of a C57BL/6J mouse after different steps of the sample preparation for imaging of the osteocyte LCN with CLSM: A) Intact tibia, B) One half of the tibia after being cut into two halves with a diamond saw, C) Tibia after being in pre-infiltration and infiltration medium with rhodamine dissolved, D) Tibia after being in embedding solution for 24 hours at +4 ^{o}C. The length of the tibia is approximately 17 mm.

Measurement and analysis

The stained and embedded tibial samples were imaged with a Leica TCS SP5 II (Leica Microsystems, Wetzlar, Germany) equipped with a 25x water immersion objective and a Leica TCS SP5 (Leica Microsystems, Wetzlar, Germany) equipped with a 100x oil immersion objective. Initially, with the 25x magnification objective, overviews of the entire tibiae were obtained and afterwards with the 100x magnification objective, images of the midshaft of the tibiae were acquired, which were used to study the osteocyte LCN. To measure the rhodamine signal, the excitation laser wavelength was set to 543 nm and the emission was measured in the range from 550 to 650 nm. To localize the fluorochrome label calcein, the excitation laser wavelength used was 488 nm and the measured emission was between 495 and 525 nm. A series of images (z-stacks), achieving a penetration depth of up to 30 µm, were obtained.
Our collaborators at the Max Planck Institute of Colloids and Interfaces in Potsdam-Golm have performed the quantification of the osteocyte LCN, extending a methodology developed at their Institute [11]. The osteocyte LCN was characterized in the newly formed tissue (tissue between

calcein labels) of both the loaded and control tibiae of the 10 week old mice. The quantification involved an adaptive thresholding of the images to distinguish between osteocyte LCN and matrix and a skeletonization of the binary data with a customized MATLAB routine to obtain the topology of the osteocyte LCN. The outcome parameters were: canalicular density, canalicular length distribution and node degree distribution. Nodes were defined as sites in the network, where two or more canaliculi meet and the node degree corresponded to the number of canaliculi meeting at one node.

3.5.2 Nanoindentation

Nanoindentation is a technology that uses a very fine and hard tip with known mechanical and geometry properties to indent a sample, such as bone, whose mechanical properties are unknown. A specific load function is applied to the indenter and a real-time load-displacement curve is obtained, from which bone elastic modulus and hardness can be extracted [291]. The load function starts with a loading period, in which the tip penetrates into the bone sample, until a defined maximum load is achieved. At this point, there is a holding period, used to dissipate the viscoelastic response of bone and to reduce the contribution of bone's plasticity. Finally, the indenter is withdrawn and the sample is unloaded. At this stage, only elastic deformation is recovered and therefore the unloading portion of the load function is used to calculate bone's elastic response. During indentation, the load and the depth of penetration in the sample are being recorded and since the geometry of the indenter tip is known, it is possible to obtain the contact area of the indents and calculate both bone's hardness and elastic modulus [291, 292].
In this work, nanoindentation was used to test the existence of gradients in the mechanical properties within the vicinity of the osteocyte lacunae, the perilacunar tissue.

Measurement and analysis

The osteocyte lacunae vicinity was studied at the intracortical region of the loaded tibial midshaft of a 26 week old mouse. Five osteocyte lacunae were chosen (based on previously obtained BSE images) and indents were performed in their vicinity with a spacing of 3 μm between each other. Nanoindentation was performed using a Scanning Nanoindenter (Hysitron Inc., Minneapolis, USA) with a Berkovich diamond indenter tip and a high-resolution microscope attached to the scanner, which allowed positioning the tip on the region of interest. The sample was mounted on a motorized table that allowed movement in the plane normal to the axial motion of the tip and automated area scans of indents were performed. The Nanoindenter was used in nanoindentation mode, which applies a specific load function and returns the resulting load-displacement curve. The load function used was characterized by a maximum of 700 μN and a holding time of 60 seconds.
The outcomes of the measurement, bone hardness and indentation modulus, were derived from the parameters of indenter force and indentation displacement with the Triboscan 7.0 software.

4 Results

4.1 Cortical bone - mass and geometry

4.1.1 *In vivo* strain gauging

The load that elicited 1200 με at the tibial midshaft of 10, 26 and 78 week old mice was determined by performing *in vivo* strain gauging. The load-strain regression curves obtained showed that the load required to attain 1200 με was approximately 11 N for 10 and 26 week old mice, while for 78 week old mice the load was lower, 9 N (Figure 26).

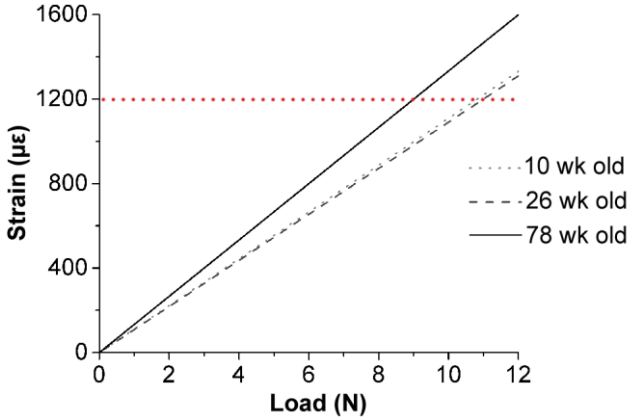

Figure 26: Strain-load regression curves for 10, 26 and 78 week old C57BL/6J mice.

4.1.2 The effect of animal age on cortical bone mass and geometry

The effect of animal age on the microCT parameters: cortical bone area (Ct.Ar), total cross-sectional area inside the periosteal envelope (Tt.Ar), cortical area fraction (Ct.Ar/Tt.Ar), cortical thickness (Ct.Th), maximum principal moment of inertia (Imax), minimum principal moment of inertia (Imin) and cortical volumetric tissue mineral density (Ct.vTMD) was assessed by comparing the control tibial midshaft of young, adult and elderly animals. Animal age had a significant effect on all the studied parameters (analysis of variance (ANOVA), $p<0.05$) (Table 1). At all the measurement days (day 0, 5, 10 and 15), adult mice had significantly higher Ct.Ar, Tt.Ar, Ct.Ar/Tt.Ar, Ct.Th, Imax, Imin and Ct.vTMD ($p<0.02$, except Ct.Ar/Tt.Ar at day 15: $p = 0.07$) than young mice. In contrast, between adult and elderly mice, there was a decrease in Ct.Ar, Ct.Ar/Tt.Ar and Ct.Th, as well as a decrease in Imax and Imin (only within the first 5 days of the experiment) (Figure 27, Figure 28). CtvTMD did not change between adult and elderly mice.

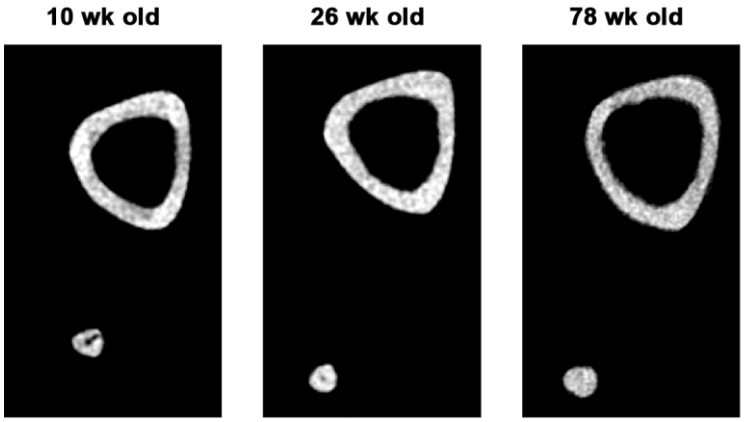

Figure 27: MicroCT images of the cross-section of cortical bone at the midshaft of 10, 26 and 78 week old C57BL/6J mice.

Different histomorphometric parameters, which characterize the amount of new tissue formed during the 15 days of the experiment, were compared between young and adult and between adult and elderly mice, at both the endocortical and periosteal regions of the control tibiae (Figure 29, Table 2). All the studied histomorphometric parameters at the endocortical region, except single-labeled surface per bone surface (sLS/BS), decreased between young and adult animals (marginally significant decrease for mineral apposition rate (MAR)), while at the periosteal region only MAR marginally significantly decreased. The statistical comparison of the different histomorphometric parameters between adult and elderly mice was limited due to the difference in the number of mice with double calcein labeling between the ages. At the periosteal region, only one elderly animal had double calcein labeling.

4.1.3 The effect of *in vivo* loading on cortical bone mass and geometry

Loading had a significant effect on Ct.Ar, Ct.Ar/Tt.Ar, Ct.Th and Ct.vTMD (ANOVA, $p<0.05$), at day 15 of the experiment. For young mice, the effect of loading was detected at day 10 and 15 of the experiment, with an increase in Ct.Ar, Ct.Ar/Tt.Ar and Ct.Th in the loaded limbs, when compared to the control limbs. The same was observed in adult animals, except that Ct.Ar increased only at day 15. Even if for young mice the Ct.Th in the loaded limbs was higher than in the control limbs already at day 0, the difference between the two was greater at day 15. In contrast to the effect of loading on young and adult animals, in elderly animals loading led to an increase in Ct.vTMD, when compared to the control limbs. In addition, loading led to an increase in Ct.Ar starting at day 5 of the experiment, an increase in Ct.Ar/Tt.Ar at day 10 and an increase of Tt.Ar at day 15 of the experiment. Already at the start of the experiment, at day 0, the Ct.Th of the loaded tibiae of elderly mice was 5% higher than the Ct.Th of the respective control tibiae. The difference in Ct.Th remained throghout the studied days, but increased up to 8% at day 15 (Figure 28, Table 1).

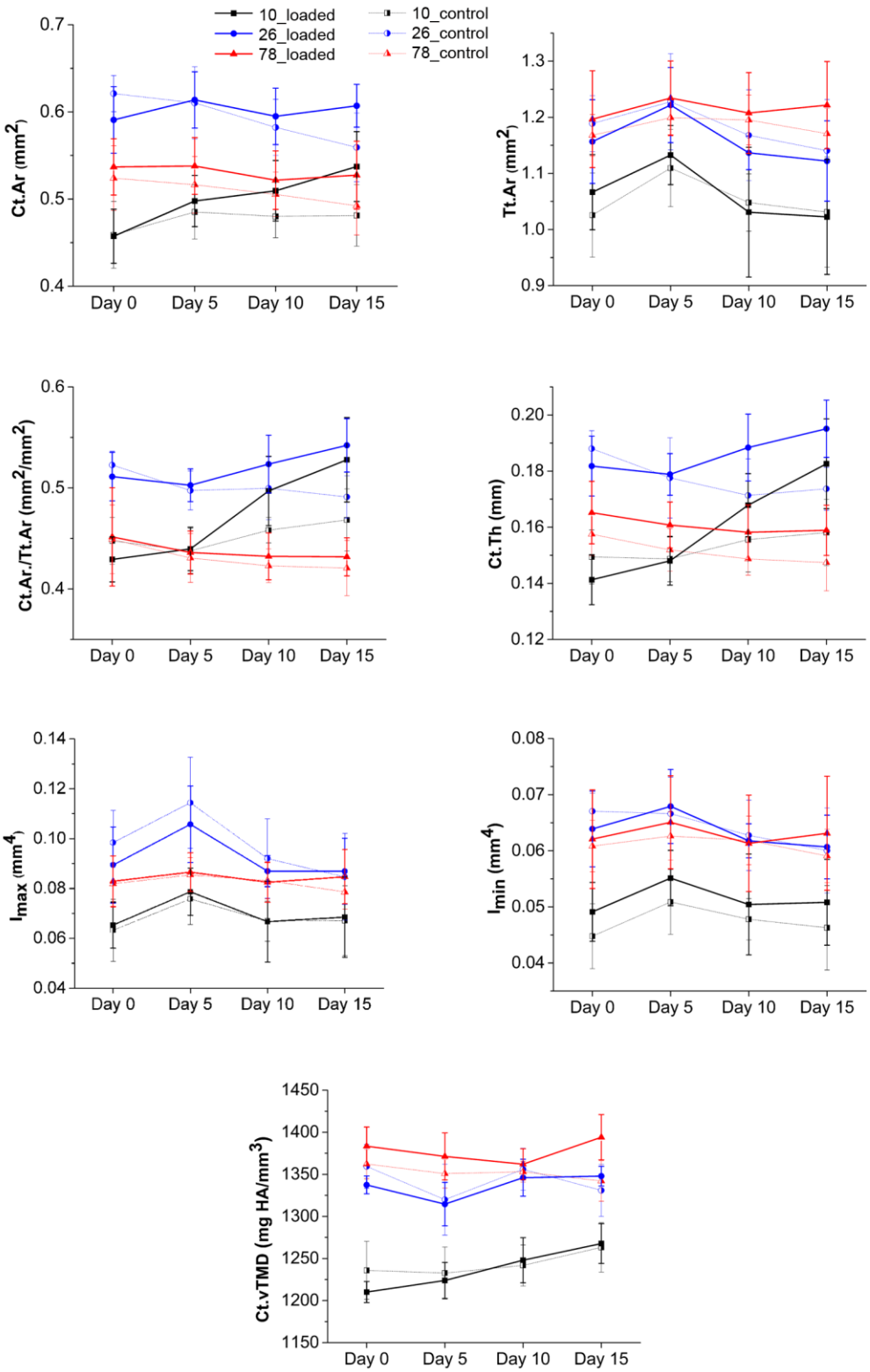

Figure 28: Ct.Ar, Tt.Ar, Ct.Ar/Tt.Ar, Ct.Th, Imax, Imin, Ct.vTMD of the control and loaded tibial midshaft of 10, 26 and 78 week old mice at day 0, 5, 10 and 15 of the *in vivo* loading experiment (bars are standard deviations of n = 6-11 mice).

	10 wk old		26 wk old		78 wk old	
Outcome	**Loaded**	**Control**	**Loaded**	**Control**	**Loaded**	**Control**
Day 0	(n=7)	(n=7)	(n=6)	(n=6)	(n=10)	(n=10)
Imax (mm^4)[c]	0.07±0.01[a]	0.06±0.01[a]	0.09±0.02	0.10±0.01	0.08±0.01	0.08±0.01
Imin (mm^4)[c]	0.05±0.01[a,b]	0.04±0.01[a]	0.06±0.01	0.07±0.00	0.06±0.01	0.06±0.01[a]
Ct.Ar (mm^2)[c]	0.46±0.03[a]	0.46±0.04[a]	0.59±0.04	0.62±0.02	0.54±0.03[a]	0.52±0.04[a]
Tt.Ar (mm^2)[c]	1.07±0.07[a]	1.03±0.07[a]	1.16±0.07	1.19±0.05	1.20±0.09	1.17±0.04
Ct.Ar/Tt.Ar (mm^2/mm^2)[c]	0.43±0.02[a]	0.45±0.02[a]	0.51±0.02	0.52±0.01	0.45±0.05[a]	0.45±0.03[a]
Ct.Th (mm)[c]	0.14±0.01[a,b]	0.15±0.01[a]	0.18±0.01[b]	0.19±0.01	0.17±0.01[a,b]	0.16±0.01[a]
Ct.vTMD (mg HA/cm^3)[c]	1210±13[a]	1236±34[a]	1337±11	1359±26	1384±23[a]	1362±18
Day 5	(n=7)	(n=7)	(n=6)	(n=6)	(n=10)	(n=10)
Imax (mm^4)[c]	0.08±0.01[a]	0.08±0.01[a]	0.11±0.02	0.11±0.04	0.09±0.01[a]	0.09±0.01[a]
Imin (mm^4)[c]	0.06±0.00[a]	0.05±0.01[a]	0.07±0.01	0.07±0.01	0.07±0.01	0.06±0.00
Ct.Ar (mm^2)$_c$	0.50±0.03[a]	0.49±0.03[a]	0.61±0.03	0.61±0.04	0.54±0.03[a]	0.52±0.03[a]
Tt.Ar (mm^2)[c]	1.13±0.05[a]	1.11±0.07[a]	1.22±0.07	1.23±0.09	1.23±0.07	1.20±0.03
Ct.Ar/Tt.Ar (mm^2/mm^2)[c]	0.44±0.02[a]	0.44±0.02[a]	0.50±0.02	0.50±0.02	0.44±0.02[a]	0.43±0.02[a]
Ct.Th (mm)[c,d,e]	0.15±0.01[a]	0.15±0.01[a]	0.18±0.01	0.18±0.01	0.16±0.01[a,b]	0.15±0.01[a]
Ct.vTMD (mg HA/cm^3)[c,e]	1224±21[a]	1233±31[a]	1315±26	1320±42	1371±28[a,b]	1351±17
Day 10	(n=7)	(n=7)	(n=6)	(n=6)	(n=10)	(n=10)
Imax (mm^4)[c]	0.07±0.02[a]	0.07±0.01[a]	0.09±0.01	0.09±0.02	0.08±0.01	0.08±0.01
Imin (mm^4)[c]	0.05±0.01[a]	0.05±0.00[a]	0.06±0.00	0.06±0.01	0.06±0.01	0.06±0.00
Ct.Ar (mm^2)[c,d]	0.51±0.03[a,b]	0.48±0.02[a]	0.59±0.03	0.58±0.03	0.52±0.03[a]	0.51±0.03[a]
Tt.Ar (mm^2)[c]	1.03±0.12[a]	1.05±0.05[a]	1.14±0.03	1.17±0.08	1.21±0.07	1.20±0.04
Ct.Ar/Tt.Ar (mm^2/mm^2)[c,d]	0.50±0.03[b]	0.46±0.01[a]	0.52±0.03[b]	0.50±0.03	0.43±0.02[a,b]	0.42±0.02[a]
Ct.Th (mm)[c,d]	0.17±0.01[a,b]	0.16±0.00[a]	0.19±0.01[b]	0.18±0.01	0.16±0.01[a,b]	0.15±0.01[a]
Ct.vTMD (mg HA/cm^3)[c]	1248±27[a]	1242±24[a]	1346±22	1356±25	1362±18[a]	1353±12
Day 15	(n=11)	(n=11)	(n=10)	(n=10)	(n=8)	(n=8)
Imax (mm^4)[c]	0.07±0.02[a]	0.07±0.01[a]	0.09±0.01	0.08±0.02	0.08±0.01	0.08±0.01
Imin (mm^4)[c,d]	0.05±0.01[a,b]	0.05±0.01[a]	0.06±0.01	0.06±0.01	0.06±0.01	0.06±0.01
Ct.Ar (mm^2)[c,d]	0.54±0.04[a,b]	0.48±0.04[a]	0.61±0.02[b]	0.56±0.04	0.53±0.04[a,b]	0.49±0.03[a]
Tt.Ar (mm^2)[c,e]	1.02±0.1[a]	1.03±0.1[a]	1.12±0.07	1.14±0.09	1.22±0.08[a,b]	1.17±0.05[b]
Ct.Ar/Tt.Ar (mm^2/mm^2)[c,d,e]	0.53±0.04[b]	0.47±0.03	0.54±0.03[b]	0.49±0.02	0.43±0.02[a]	0.42±0.03[a]
Ct.Th (mm)[c,d,e]	0.18±0.02[a,b]	0.16±0.01[a]	0.20±0.01[b]	0.17±0.01	0.16±0.01[a,b]	0.15±0.01[a]
Ct.vTMD (mg HA/cm^3)[c,d,e]	1268±24[a]	1263±29[a]	1348±12	1331±31	1394±27[a,b]	1342±24

Table 1: Mean values and standard deviations of microCT cortical bone parameters of the loaded and control tibial midshaft of 10, 26 and 78 week old mice at day 0, 5, 10 and 15 of the *in vivo* loading experiment. [a]Different from 26 week old, unpaired t-test $p<0.05$; [b]different from control, paired t-test $p<0.05$; [c]between-subject effects of animal age (10, 26 and 78 week old); [d]within-subject effects of loading (loaded, control limbs); [e]interactions between these terms, repeated measures ANOVA, $p<0.05$ [293].

At day 15, the effect of loading on the different histomorphometric parameters was assessed by comparing control and loaded tibiae at both endocortical and periosteal regions (Figure 29, Table 2). In young mice, loading led to an increase in MAR and bone formation rate (BFR/BS) in both endocortical and periosteal regions and also to an increase in double-labeled surface per bone surface (dLS/BS) and mineralizing surface (MS/BS) in the periosteal region. For adult mice all the parameters, except sLS/BS, increased in the loaded tibiae, when compared to the control tibiae at both endocortical and periosteal regions. In elderly mice, loading didn't lead to significant changes in the measured histomorphometric parameters. However, the comparisons between most of the periosteal parameters could not be established due to the reduced number of mice with double calcein labeling.

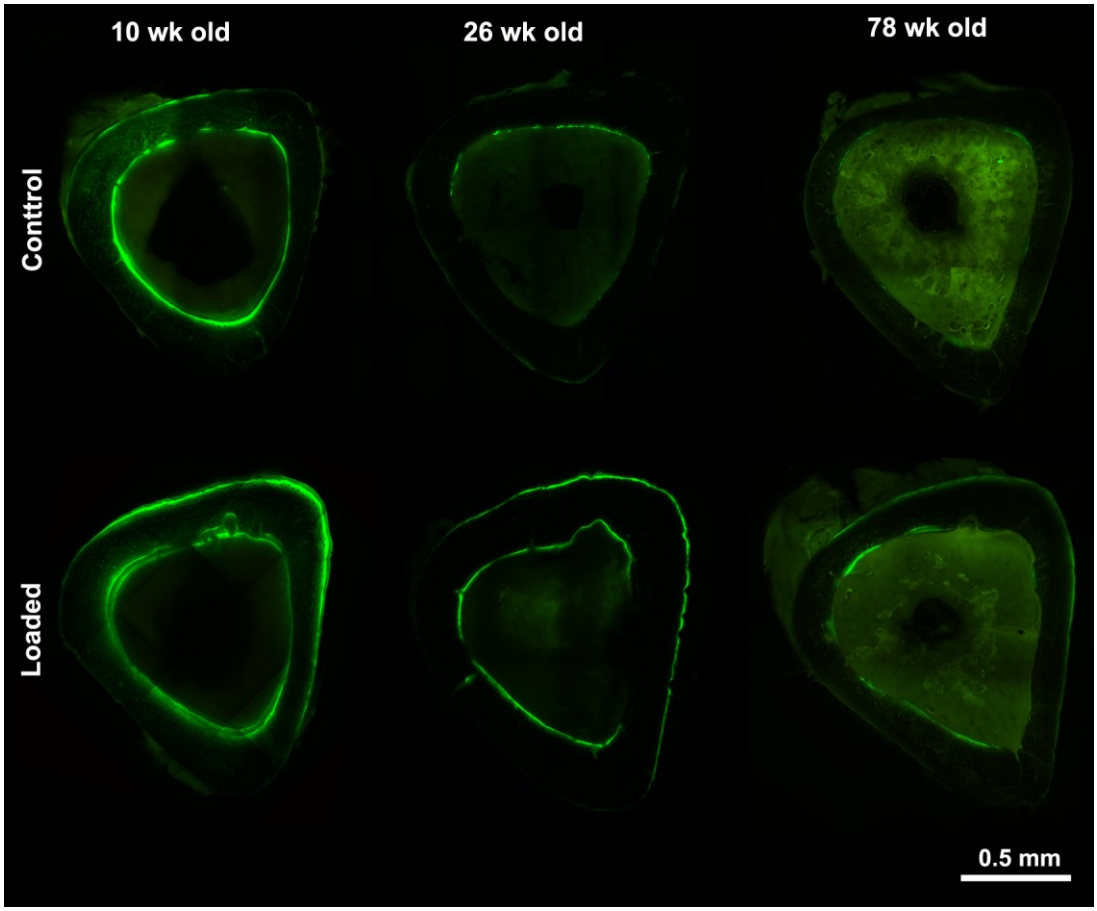

Figure 29: Representative fluorescence image of the cross-section of a control and loaded tibia of one 10 week old, one 26 week old and one 78 week old C57BL/6J mouse.

Outcome	10 wk old		26 wk old		78 wk old	
	Loaded	**Control**	**Loaded**	**Control**	**Loaded**	**Control**
	(n=10)	(n=10)	(n=10)	(n=10)	(n=5)	(n=5)
Ec.sLS/BS (%)[c]	10.9±5.5	13.0±9.5[a]	21.0±14.8	23.3±7.3	28.6±9.4	30.4±5.0
Ec.dLS/BS (%)[c,d]	87.0±6.2[a]	80.4±13.2[a]	38.6±13.8[b]	15.4±12.4(n=8)	14.3 ± 4.0[a]	12.2±10.3(n=4)
Ec.MS/BS (%)[c,d,e]	92.4±4.3[a]	86.9±8.8[a]	49.1±7.7[b]	27.1±12.3	28.6±6.4[a]	25.0±9.8
Ec.MAR (μm/day)[d,e]	2.08±0.27[a,b]	1.17±0.34	1.64±0.47[b]	0.85±0.35(n=8)	1.29±0.38	1.51±0.63(n=4)
Ec.BFR/BS(μm/day)[c,d,e]	1.92±0.26[a,b]	1.03±0.36[a]	0.81±0.27[a,b]	0.28±0.18(n=8)	0.39±0.21[a]	0.40±0.15(n=4)
Ps.sLS/BS (%)	26.9±12.1	40.3±26.5	23.7±15.3	29.7±27.1	32.1±19.0	37.4±9.2
Ps.dLS/BS (%)[c,d,e]	50.9±16.6[b]	10.0±10.8	36.4±19.6[b]	12.1±9.0	4.7±1.1(n=2)	2.4(n=1)
Ps.MS/BS (%)[c,d,e]	64.3±13.4[b]	30.2±9.7	48.3±19.8[b]	26.9±19.0	17.9±10.5[a]	19.2±4.0
Ps.MAR (μm/day)[c,d,e]	1.67±0.49[a,b]	0.57±0.15	1.03±0.30[b]	0.72± 0.17	1.22±0.67(n=2)	1.39(n=1)
Ps.BFR/BS(μm/day)[c,d,e]	1.09±0.48[a,b]	0.16±0.05	0.53±0.36[b]	0.20±0.15	0.32±0.23(n=2)	0.2(n=1)

Table 2: Mean values and standard deviations of endocortical and periosteal bone formation indices at the loaded and control tibial midshaft of 10, 26 and 78 week old mice. [a]Different from 26 week old, unpaired t-test $p<0.05$; [b]different from control, paired t-test $p<0.05$; [c]between-subject effects of animal age (10, 26 and 78 week old); [d]within-subject effects of loading (loaded, control limbs); [e]interactions between these terms, repeated measures ANOVA, $p<0.05$. Note: Although ten, 10 week old and 26 week old mice and five, 78 week old mice were studied, some mice did not have double calcein labels present; in this case the number of mice with labels is indicated in the table [293].

4.2 Cortical bone - mineral and matrix properties

4.2.1 Synchrotron sSAXS - Selection criteria for measured points

The calculation of mean mineral particle thickness, T parameter, and degree of mineral alignment, ρ parameter, was performed as described in section 3.4.1. However, for some of the points this calculation was based on bad statistics (as possibly the volume hit by the beam was not big enough), which made the obtained T and ρ values for these points unreliable. A criterion of exclusion of these points had to be defined. For that, the integral intensity of I(χ), which corresponds to the amount of mineral particles, was calculated for each measured point and afterwards an histogram of all the values obtained for each tibia was plotted. By comparing the different histograms, a reasonable criterion of exclusion—all the points whose value was below half the median of the sSAXS integral intensity distribution (Figure 30)—was defined. Approximately 9% of the points were excluded from the analysis.

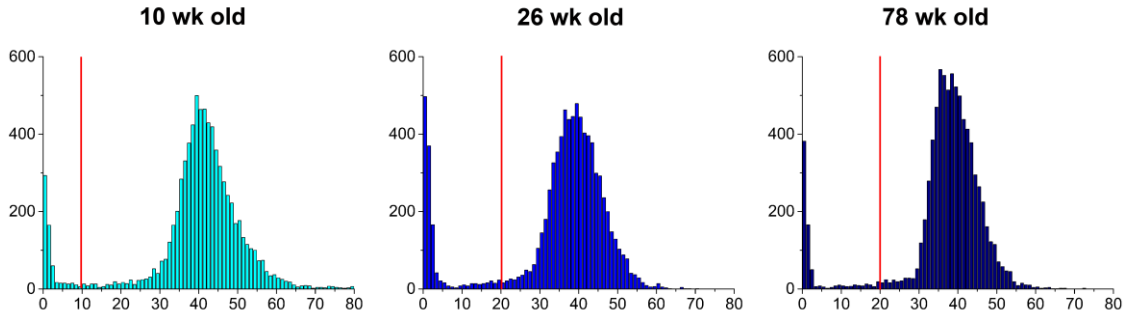

Figure 30: Histogram of the sSAXS integral intensity of one 10 week old, one 26 week old and one 78 week old mouse. The red lines in the graphs indicate the value which corresponds to half of the median and below which all points were excluded from analysis.

4.2.2 The effect of animal age on bone mineral and matrix properties

Intracortical region

To study the effect of animal age on bone mineral and matrix properties, the intracortical region of the control tibial midshaft was compared between young, adult and elderly animals using synchrotron sSAXS and FTIRI.

The mineral:matrix ratio, carbonate:mineral ratio, mineral crystallinity, acid phosphate content and collagen maturity, all parameters measured with FTIRI, were significantly affected by animal age (ANOVA, $p<0.05$). Between 10 and 26 week old mice, there was an increase in the mineral:matrix ratio (close to significant, $p = 0.07$) and carbonate:mineral ratio of the control limbs. The mineral crystallinity, in contrast decreased, when comparing 26 with 10 week old mice. Between 26 and 78 week old mice, mineral:matrix ratio remained constant, while mineral crystallinity increased and acid phosphate content decreased. No significant changes were detected in collagen maturity between the control tibiae of 10, 26 and 78 week old mice (Figure 31).

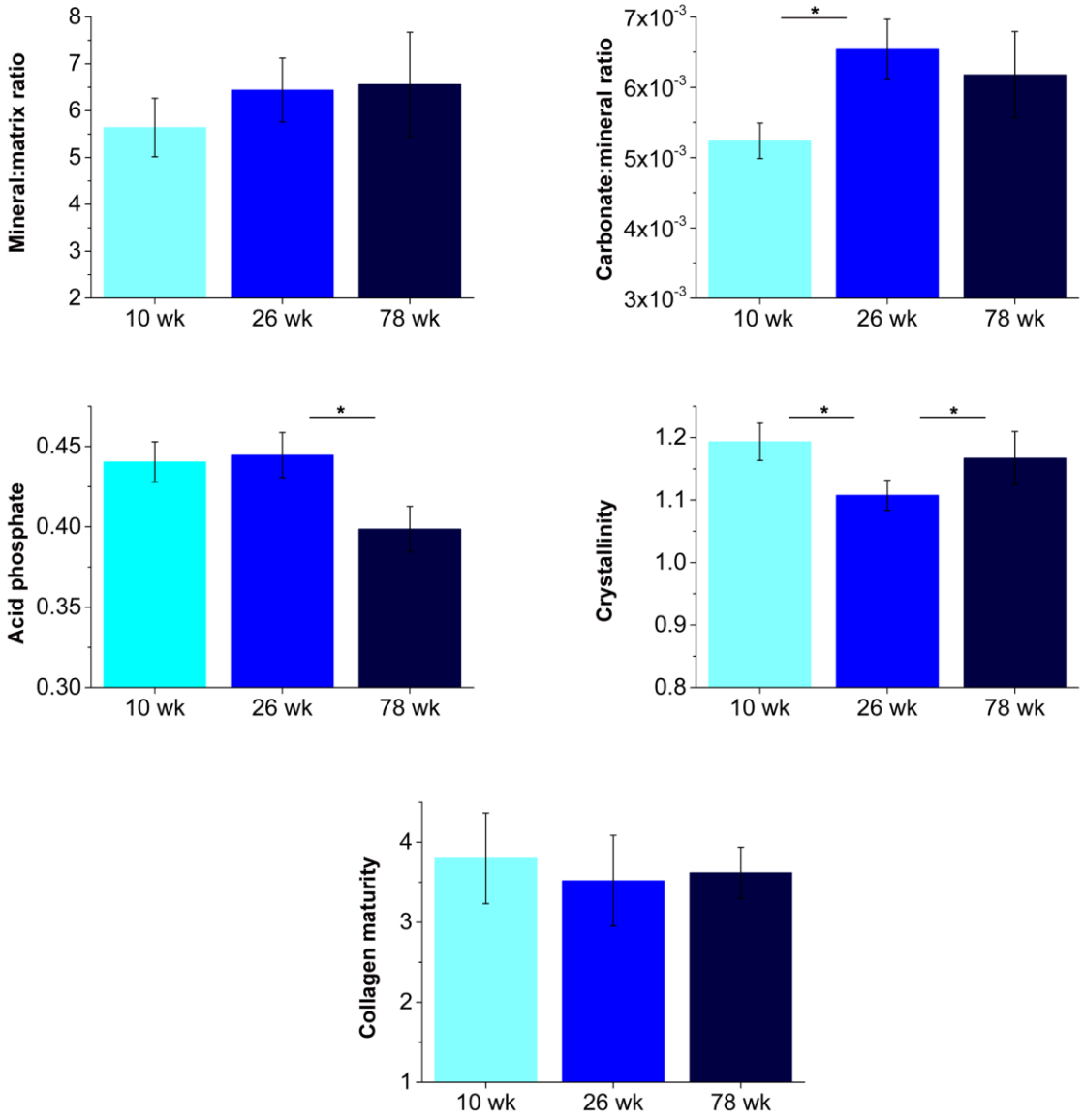

Figure 31: Mineral:matrix ratio, carbonate:mineral ratio, crystallinity, acid phosphate and collagen maturity at the intracortical region of the control tibial midshaft of 10, 26 and 78 week old C57BL/6J mice (bars are standard deviations of n = 5 mice; * = significant difference).

Using sSAXS, changes in T parameter and ρ parameter with animal age were studied. In Figure 32, maps of the distribution of T and ρ parameters at the intracortical region of the tibial midshaft of young, adult and elderly mice are presented.

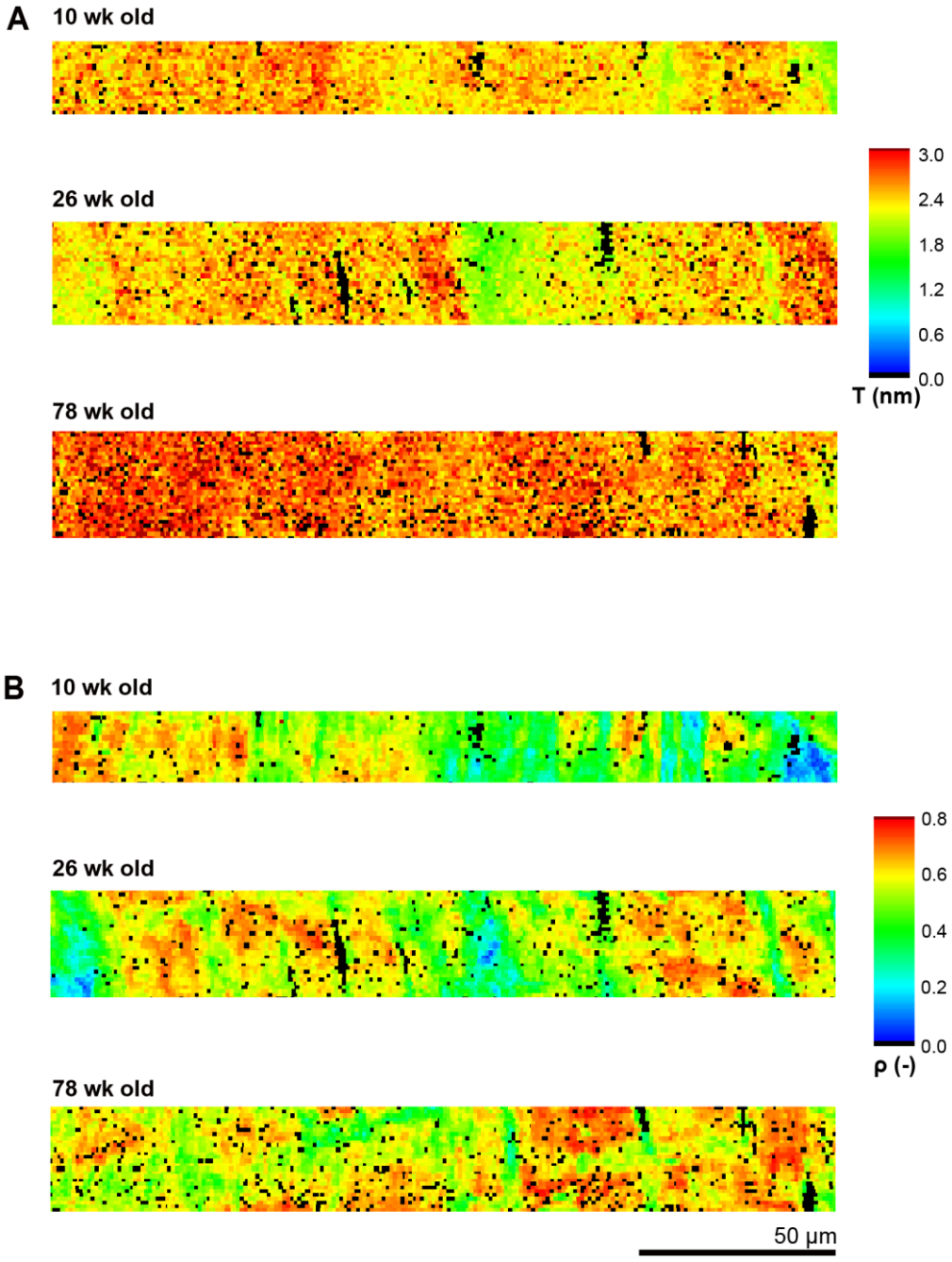

Figure 32: A) T parameter and B) ρ parameter maps at the intracortical region of the control tibial midshaft of one 10 week old, one 26 week old and one 78 week old C57BL/6J mouse.

A trend of increased mean mineral thickness with animal aging was detected. However, the changes were not very pronounced: between 10 and 26 week old mice, the difference was as small as 0.05 nm and not larger than 0.26 nm, while between 26 and 78 week old mice, the difference varied between 0.08 nm and 0.30 nm. No clear trend was detected for the mean ρ parameter with animal age (Table 3).

	10 week old	26 week old	78 week old
T (nm)	2.3/2.4	2.4/2.6	2.7/2.2
ρ (-)	0.62/0.50	0.55/0.56	0.59/0.56

Table 3: Mean values of T and ρ parameters at the intracortical region of the control tibial midshaft of 10, 26 and 78 week old C57BL/6J mice (n = 2 mice/age).

Apart from the total average T and ρ parameters, the percentages of mineral particles within a certain range of T and ρ values were also calculated. All the intracortical points of the 2 samples studied per age were combined into three bins and the percentages of mineral particles with mean thickness between 1 and 2 nm, between 2 and 2.5 nm and above 2.5 nm were calculated. In addition, the percentages of mineral particles with a degree of alignment between 0 and 0.4, between 0.4 and 0.6 and above 0.6 were determined (Figure 33). While for young and adult mice, most of the mineral particles had a thickness between 2 and 2.5 nm, for elderly mice there was a shift towards thicker mineral particles, with the highest percentage of particles having a mean thickness above 2.5 nm. For all ages, the percentage of mineral particles with mean thickness between 1 and 2 nm was low. The percentage of mineral particles with low values of degree of alignment, between 0 and 0.4, was low for young, adult and elderly mice, as well. However, no particular trend was detected in how the percentages of mineral particles within the defined ranges of degree of alignment change with animal aging (Figure 33).

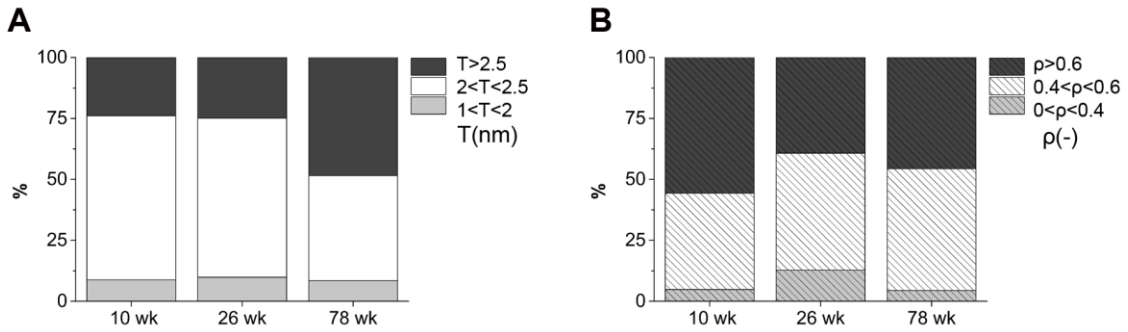

Figure 33: Stack plots of A) T parameter and B) ρ parameter at the intracortical region of the control tibial midshaft of 10, 26 and 78 week old C57BL/6J mice (for each age, approximately 12000 points were measured; n = 2 mice/age).

Endocortical and Periosteal Regions

The effect of animal age on bone mineral and matrix properties of the tissue at the endocortical and periosteal regions (0 to 20 μm away from endocortical and periosteal surfaces, respectively) was determined, by comparing these regions at the control limbs between young, adult and elderly mice using FTIRI. Although there were differences in the ratio of mineral:matrix ratio, carbonate:mineral ratio, mineral crystallinity, acid phosphate content and collagen maturity at the endocortical and periosteal regions between 10 and 26 week old or between 26 and 78 week old mice, these differences never reached significance. Between 10 and 78 week old mice, only a significant increase in carbonate:mineral ratio was detected at both the endocortical and periosteal regions (Table 4).

4.2.3 The effect of tissue age on bone mineral and matrix properties

The influence of tissue age on the bone mineral and matrix properties was investigated by comparing tissue at endocortical and periosteal regions, 0 to 20 μm away from endocortical or periosteal surfaces respectively, with tissue at the intracortical region of the control limbs. It should be noted that the tissue studied at the endocortical and periosteal regions didn't always entirely correspond to newly formed tissue, but rather to younger tissue than the intracortical more mature tissue.

Tissue age was shown to significantly influence all the parameters analyzed with FTIRI (ANOVA, $p<0.05$) (Table 4). When doing subanalyses (t-tests), the endocortical and periosteal regions of the control limbs of the 10, 26 and 78 week old mice were shown to have lower mineral:matrix ratio (Figure 34) and crystallinity (marginally significant exception for periosteal versus intracortical region comparison for 78 week old mice: $p = 0.06$) and higher acid phosphate content than the intracortical region.

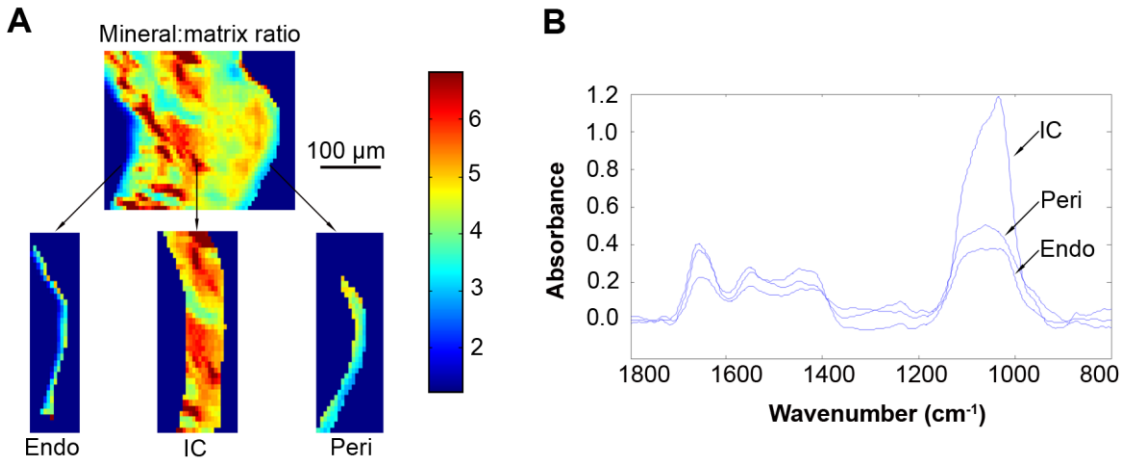

Figure 34: Mineral:matrix ratio is higher in the intracortical (IC) region than in the endocortical (Endo) or periosteal (Peri) regions of the control limbs of a 26 week old mouse. A) Image of the distribution of mineral:matrix ratio in the different regions and B) respective FTIRI spectra.

Although collagen maturity was always lower in the periosteal and endocortical regions (except in 78 week old mice) than in the intracortical region of the tibial midshaft, only for the young mice was this difference significant or marginally significant (p = 0.06, periosteal versus intracortical region). The carbonate:mineral ratio was always higher in the endocortical than in the intracortical region and always lower in the periosteal than in the intracortical region for the young and adult mice. However, these differences were only significant when comparing the periosteal and intracortical region of young mice. Differently, elderly mice showed higher carbonate:mineral ratio in the periosteal than in the intracortical region (Figure 35).

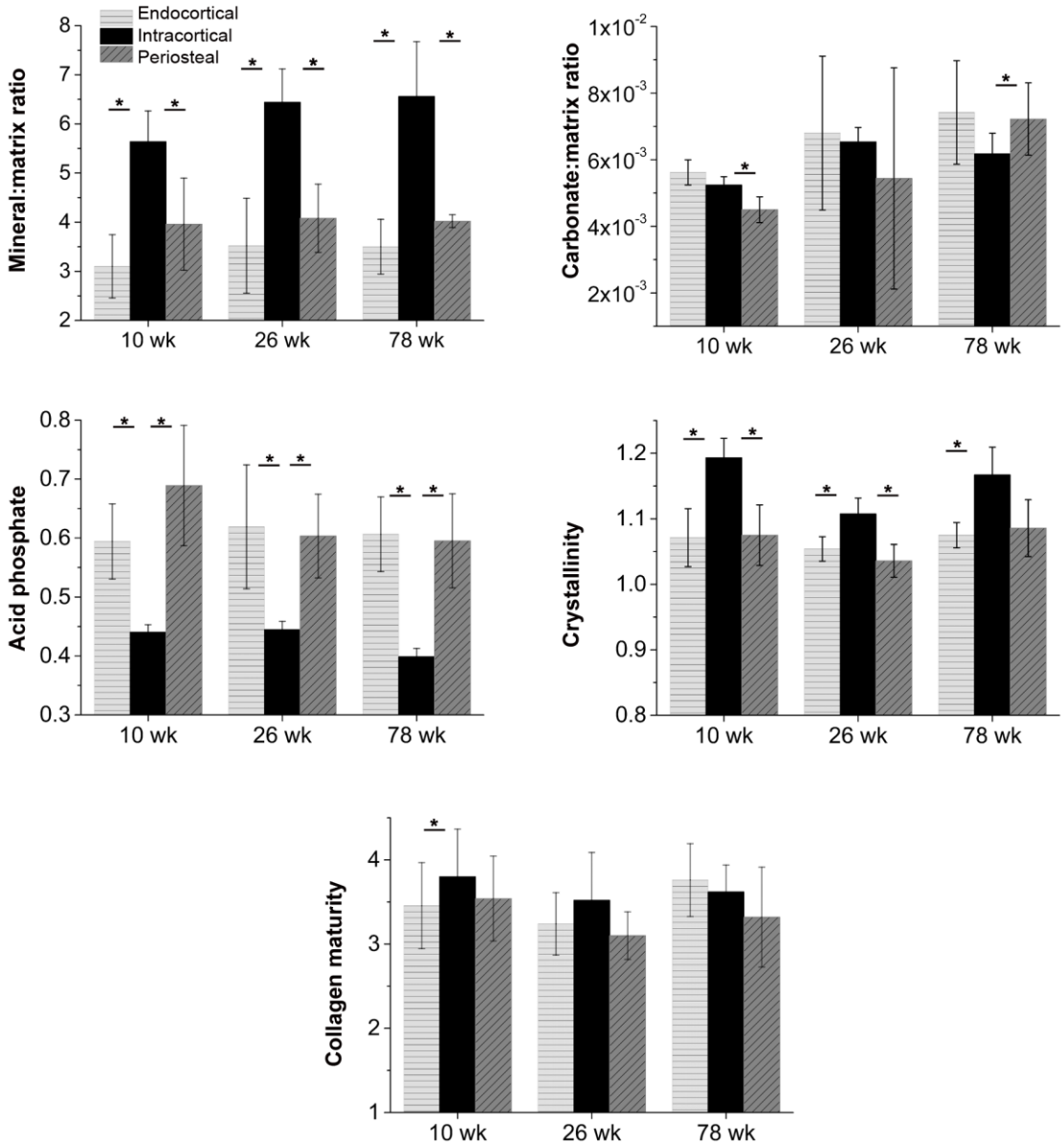

Figure 35: Regional differences reflecting tissue age in mineral:matrix ratio, carbonate:mineral ratio, crystallinity, acid phosphate and collagen maturity for the control limbs of 10, 26 and 78 week old C57BL/6J mice (bars are standard deviations of n = 5 mice; * = significant difference).

Outcome	10 wk old		26 wk old		78 wk old	
	Loaded (n=5)	Control (n=5)	Loaded (n=5)	Control (n=5)	Loaded (n=5)	Control (n=5)
Mineral:matrix[c,f]						
Endocortical	2.94±0.47[g,h]	3.10±0.64[h]	3.44±0.63[h]	3.52±0.97[h]	4.36±0.65[a,b,h]	3.50±0.56[h]
Intracortical	5.84±0.25	5.64±0.62	6.58±0.74	6.44±0.68	7.32±0.63	6.56±1.11
Periosteal	3.96±0.30[h]	3.96±0.94[h]	3.30±1.02[h]	4.08±0.69[h]	4.20±0.66[h]	4.02±0.13[h]
Crystallinity[c,f]						
Endocortical	1.08±0.03[h]	1.07±0.04[h]	1.04±0.39[h]	1.05±0.02[h]	1.08±0.04[h]	1.08±0.02[h]
Intracortical	1.18±0.04	1.19±0.03[a]	1.12±0.05	1.11±0.02	1.20±0.02[a]	1.17±0.04[a]
Periosteal	1.10±0.03[h]	1.08±0.05[h]	1.06±0.03[b]	1.04±0.03[h]	1.08±0.03[h]	1.09±0.04
Collagen maturity[c,e,f]						
Endocortical	3.4±0.3	3.4±0.3[h]	3.0±0.4	3.2±0.4	4.2±0.3[a]	3.8±0.4[g]
Intracortical	3.5±0.4	3.8±0.6	3.3±0.1	3.5±0.6	4.0±0.4[a,b]	3.6±0.3
Periosteal	3.5±0.5	3.5±0.5	3.1±0.5	3.1±0.3	4.0±0.4[a,b]	3.3±0.6
Carbonate:mineral x 1000[c,f]						
Endocortical	5.9±1.6[g]	5.6±0.4[g]	8.4±2.6	6.8±2.3	5.5±1.3	7.4±1.6
Intracortical	4.9±0.5[a]	5.2±0.3[a]	7.0±0.9	6.5±0.4	5.5±0.4[a]	6.2±0.6
Periosteal	4.1±0.4[h]	4.5±0.4[a,h]	5.6±0.7[h]	5.4±3.3	5.6±1.0	7.2±1.1[h]
Acid phosphate[c,e,f]						
Endocortical	0.61±0.06[h]	0.59±0.06[h]	0.74±0.12[h]	0.62±0.11[h]	0.54±0.04[a,h]	0.60±0.06[h]
Intracortical	0.45±0.02[b]	0.44±0.01	0.46±0.03	0.45±0.01	0.39±0.03[a]	0.40±0.01[a]
Periosteal	0.70±0.08[h]	0.69±0.10[h]	0.85±0.16[b,h]	0.60±0.07[h]	0.53±0.05[a,h]	0.60±0.08[h]

Table 4: Mean values and standard deviations of parameters measured with FTIRI at the endocortical, intracortical and periosteal regions of the loaded and control tibial midshaft of 10, 26 and 78 week old mice. [a]Different from 26 week old, unpaired t-test $p<0.05$; [b]different from control, paired t-test $p<0.05$; [c]between-subject effects of animal age (10, 26 and 78 week old); [e]interactions between animal age and loading; [f]within-subject effects of region, repeated measures ANOVA, $p<0.05$; [g]different from periosteal; [h]different from intracortical, paired t-test $p<0.05$.

The average T and ρ parameters measured with sSAXS tended to be lower at the endocortical region, but similar or higher at the periosteal than at the intracortical region of the control limbs. However, inside the intracortical region there were certain areas where the T and ρ parameters were as low as at the endocortical region. In Figure 36, both the map and the graph of T parameter profile (average of all the T parameters of each column, separated by 1 μm, starting from the endocortical surface) show that the lowest T parameter values were detected not only in the endocortical region, but also in certain areas of the intracortical region, such as at approximately 120 to 140 μm from the endocortical surface. These areas could have been in close proximity to blood vessels within the bone.

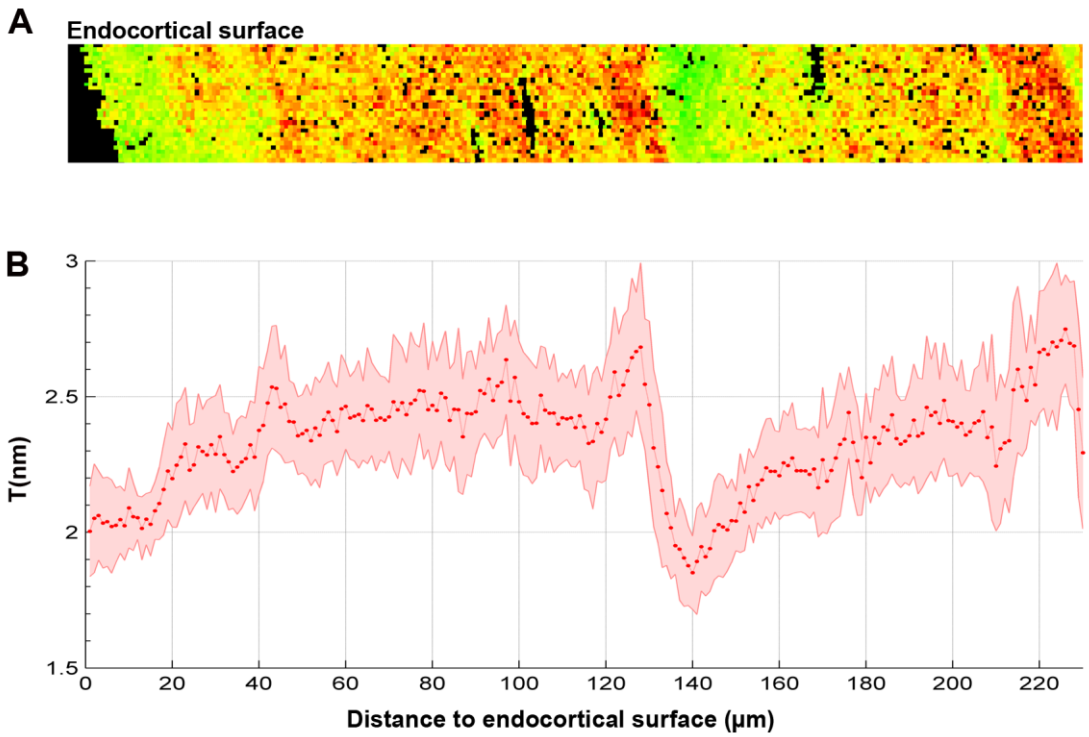

Figure 36: A) Map of T parameter and B) respective graph of T parameter profile through cortex starting at the endocortical surface in the control tibia of a 26 week old mouse. The red line in the graph corresponds to the average T parameter and the shadowed pink area above and below the line represents the standard deviation.

4.2.4 The effect of *in vivo* loading on mineral and matrix properties of pre-existing bone

The intracortical region of the control and loaded limbs was compared to determine if loading had an effect on the pre-existing bone. The endocortical and periosteal regions, where newly formed bone can be laid down were excluded from the analysis. The effect of additional *in vivo* loading on the intracortical tissue was dependent on the animal age. *In vivo* loading had no effect on the intracortical mineral and matrix properties of adult mice and in young mice, loading only caused a significant increase of 3% in acid phosphate content. In elderly mice, loading led to a 10% significant increase in collagen maturity in the loaded limbs. In addition and even if the difference was not significant, the average mineral:matrix ratio was 12% higher in the loaded limbs than in the control limbs of elderly mice (Figure 37).

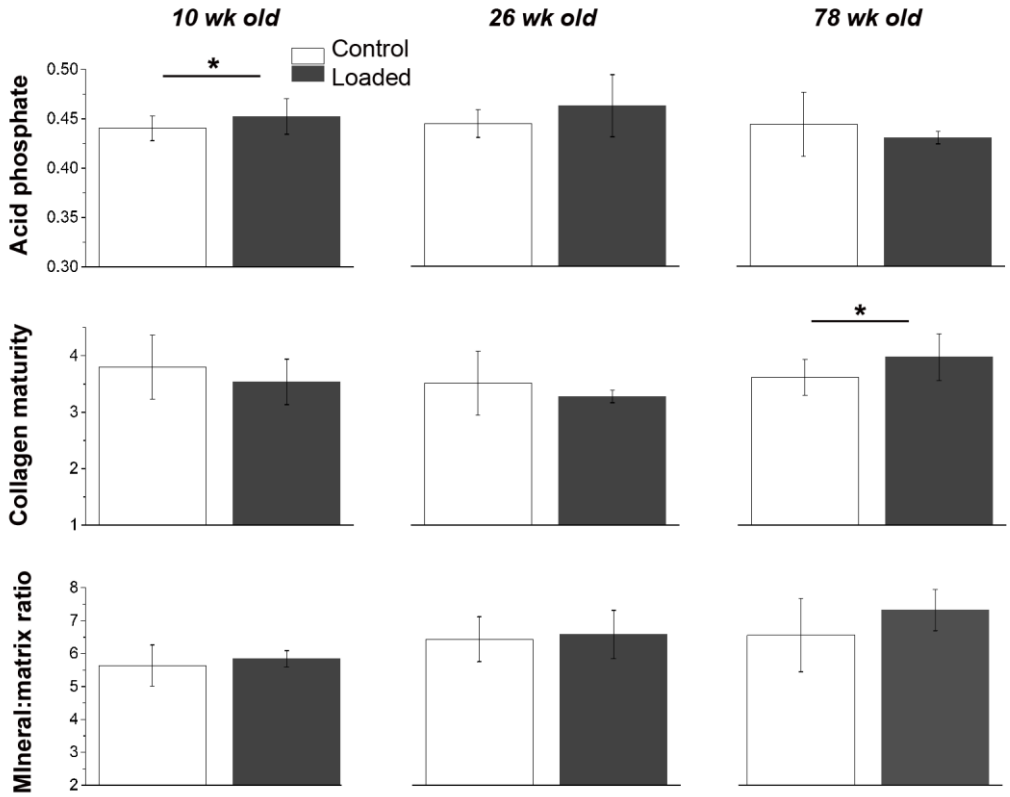

Figure 37: Acid phosphate content, collagen maturity and mineral:matrix ratio in the intracortical region of the control and loaded limbs of 10, 26 and 78 week old C57BL/6J mice (bars are standard deviations of n = 5 mice; * = significant difference).

The sSAXS measurements did not reveal any trend of alterations of T and ρ parameters between control and loaded limbs.

4.2.5 The effect of *in vivo* loading on mineral and matrix properties of newly formed bone

Are mineral and matrix properties of new bone formed in response to physiological loading and additional in vivo loading similar?

The new tissue formed in the loaded tibiae of young mice had the same mineral:matrix ratio, carbonate:mineral ratio, crystallinity and acid phosphate content and also the same collagen maturity than the new tissue formed in the control tibiae (Figure 38).

The comparison between newly formed tissue in response to additional *in vivo* loading and newly formed tissue from only physiological loading for adult or elderly mice was limited by the fact that the amount of newly formed tissue at both the control and loaded limbs of these mice was relatively low, in comparison with the FTIRI spatial resolution (6.25 μm). Nevertheless, in adult mice only at the periosteal region the mineral crystallinity and acid phosphate content were significantly greater in the loaded limbs than in the control limbs, while for elderly mice

collagen maturity in the periosteal region and mineral:matrix ratio in the endosteal region were greater in the loaded limbs, when compared to the control limbs.

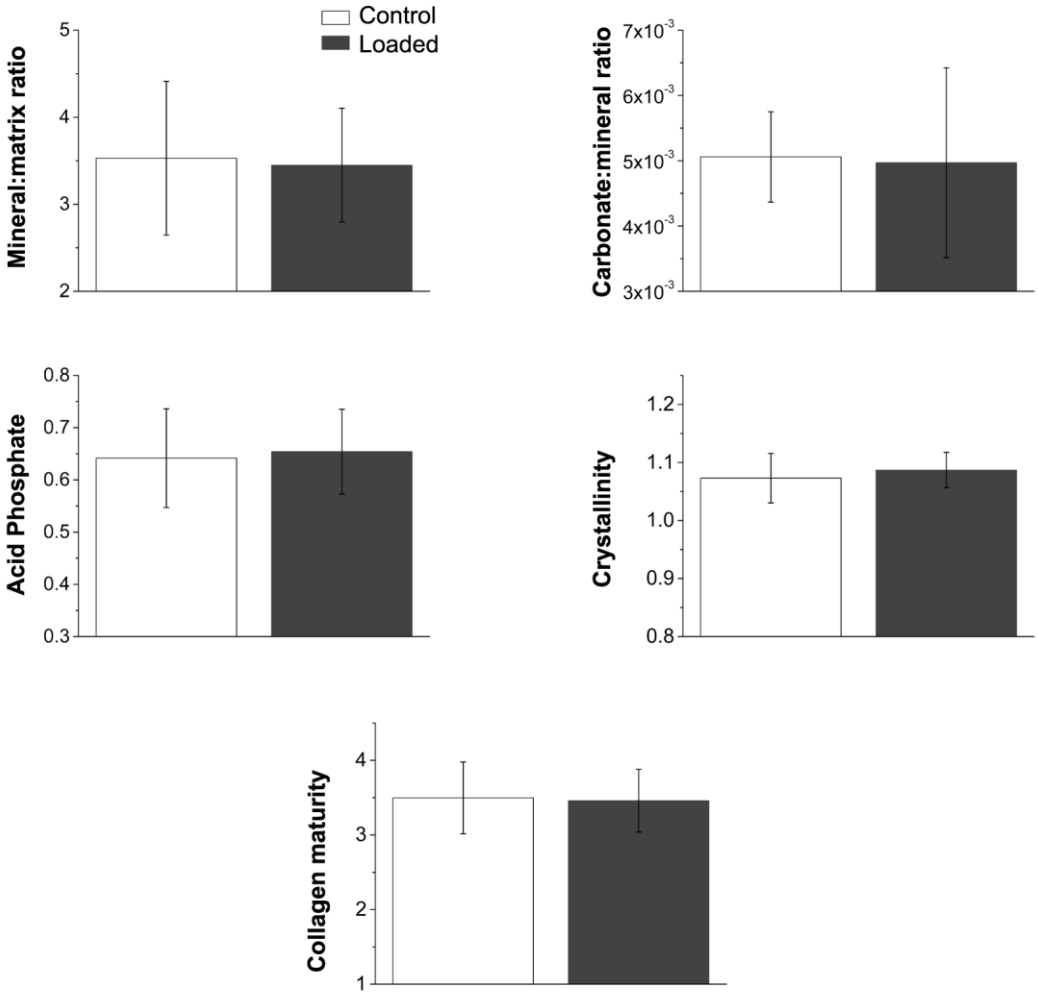

Figure 38: Mineral:matrix ratio, carbonate:mineral ratio, crystallinity, acid phosphate and collagen maturity of the tissue at the endocortical and periosteal regions is similar between loaded and control limbs of 10 week old mice. Averages comprise tissue at endocortical and periosteal regions and bars represent standard deviations of n = 5 mice.

No pronounced differences were observed for the young mice in T and ρ parameters in the endocortical and periosteal regions, between the loaded and the control limbs. The average T and ρ parameters of the loaded limbs were only 4.8% and 12.6%, respectively, greater than in the control limbs (Figure 39). No new tissue was formed during the *in vivo* loading experiment in the control tibiae of the two adult and the two elderly mice studied with sSAXS. Therefore, the comparison between newly formed tissue with *in vivo* loading and newly formed tissue from only physiological loading was established just for the young mice.

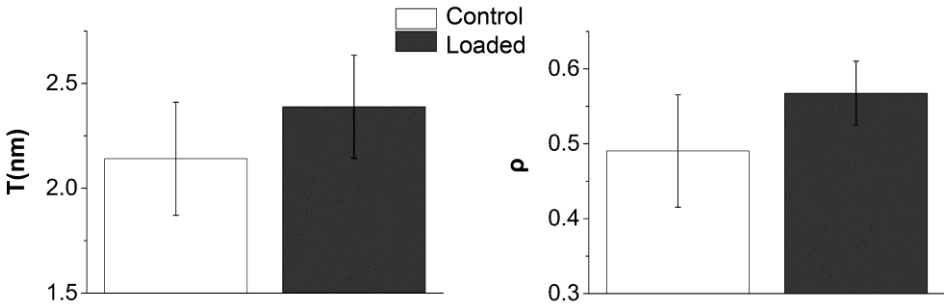

Figure 39: T and ρ parameters of the newly formed tissue at the endocortical and periosteal regions are similar between loaded and control limbs of 10 week old mice. Averages comprise tissue at endocortical and periosteal regions and bars represent standard deviations of n = 2 mice/age.

Are mineral and matrix properties of newly formed bone different according to the region where it is formed?

The newly formed tissue at the periosteal region of the tibia was distinct from the newly formed tissue at the endocortical region. This was observed in the loaded tibia of 10, 26 and 78 week old mice. Figure 40 illustrates the higher T and ρ parameters detected at the periosteal region, when compared to the endocortical region of the loaded tibia of the young 10 week old mice; the age with the highest amount of newly formed bone tissue during the experimental period.

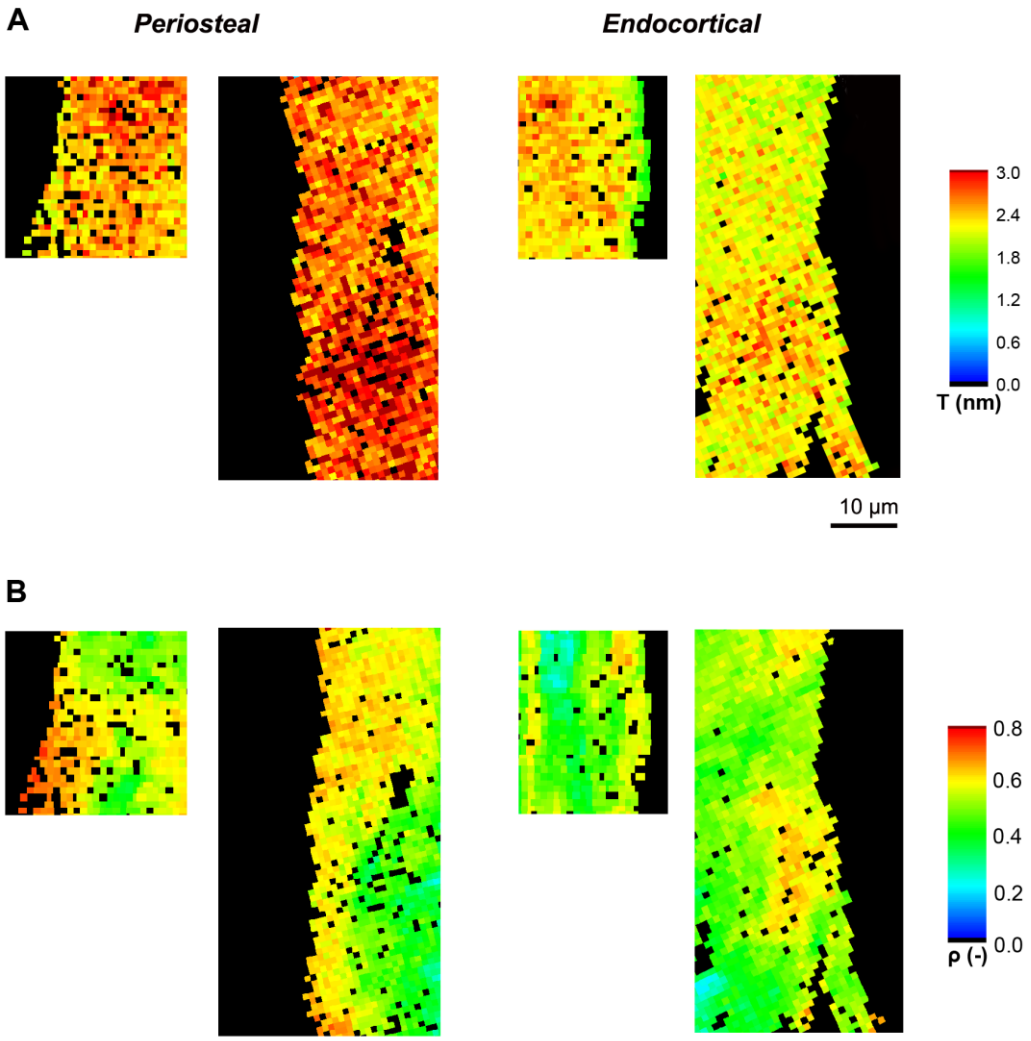

Figure 40: Newly formed tissue at the endocortical region of the loaded limbs of two 10 week old mice had lower A) T parameter and B) ρ parameter than newly formed tissue at the periosteal region.

Plotting the histograms of the T parameter and the ρ parameter of all the measured points at the endocortical and periosteal regions of the loaded limbs of the two 10 week old mice also reveals a shift towards thicker mineral particles with higher degree of alignment in the periosteal region (Figure 41). In the endocortical region, most of the mineral particles, 81.6% and 77.8% respectively, had thickness between 2 and 2.5 nm and degree of alignment between 0.4 and 0.6. Only 7.1% of the mineral particles had mineral thickness above 2.5 nm and only 19.7% had degree of alignment above 0.6 in the endocortical region. In contrast, in the periosteal region, 63.7% of the mineral particles had thickness above 2.5 nm and 56.2%, a degree of alignment above 0.6. Only 36% of the mineral particles had thickness between 2 and 2.5 nm and only 42.9% had a degree of alignment between 0.4 and 0.6 in the periosteal region (Table 5).

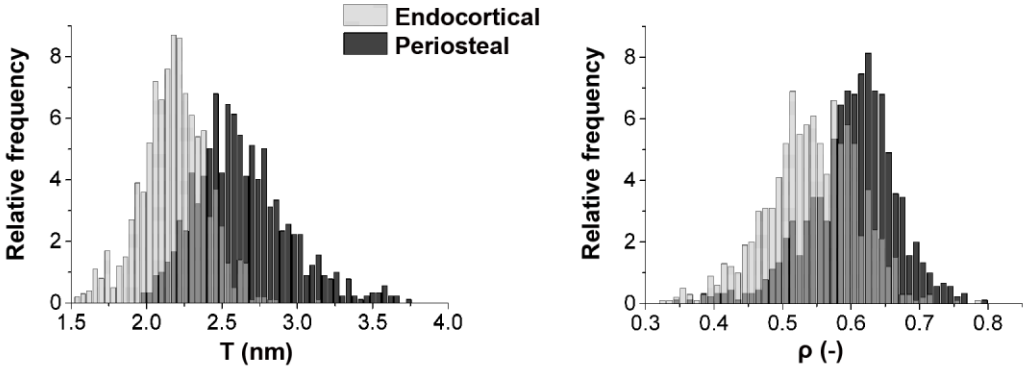

Figure 41: Histogram of T parameter (binning = 0.02) and ρ parameter (binning = 0.0005) of all the measured points at the endocortical and periosteal regions of the loaded limbs of two 10 week old mice.

	%		
	1<T<2 (nm)	**2<T<2.5 (nm)**	**T>2.5 (nm)**
Endocortical	11.3	81.6	7.1
Periosteal	0.3	36.0	63.7

	ρ<0.4	**0.6<ρ<0.4**	**ρ>0.6**
Endocortical	2.5	77.8	19.7
Periosteal	0.8	42.9	56.2

Table 5: Percentage (%) of the measured points, at the endocortical and periosteal regions of the loaded tibial midshaft of two 10 week old mice, with T and ρ parameters within defined value ranges.

The young mice were also imaged with multiphoton confocal microscopy to qualitatively detect, using second harmonic generation, differences in the arrangement of the collagen fibers between endocortical and periosteal regions. The images obtained suggested that the collagen fibers at the periosteal region were more aligned than at the endocortical region of the tibial midshaft (Figure 42).

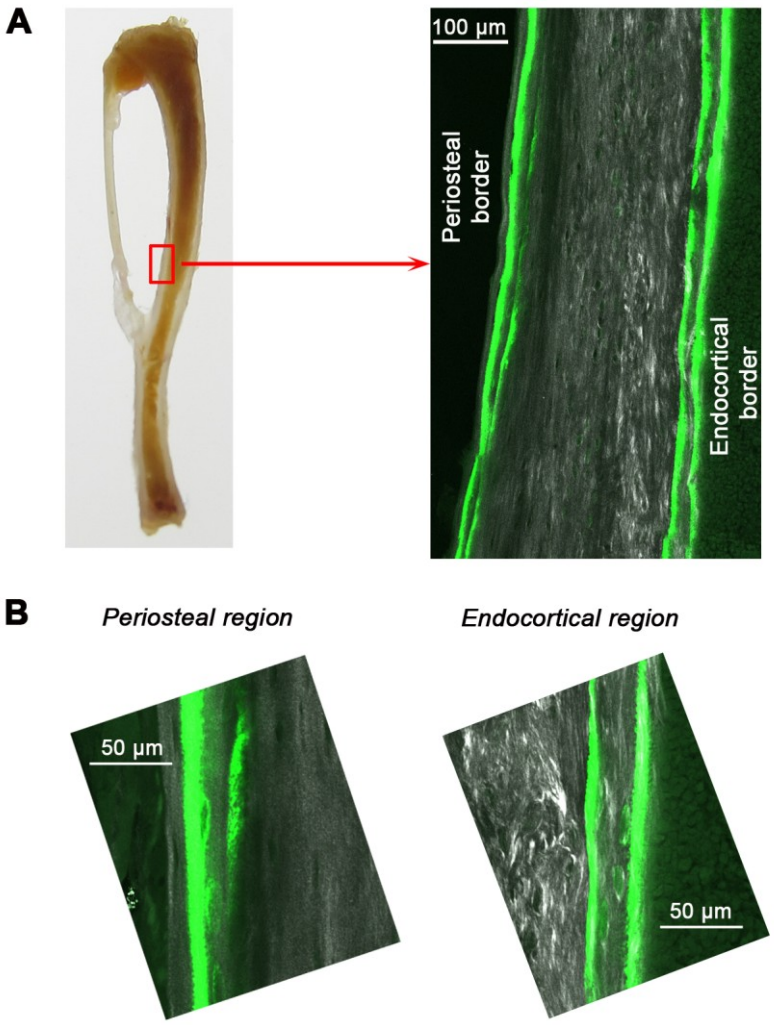

Figure 42: A) Second harmonic generation by multiphoton confocal microscopy for collagen visualization in one 10 week old mouse at the tibial midshaft, B) Zoomed-in images of the endocortical and periosteal regions at the tibial midshaft.

In addition, FTIRI analysis revealed that the new tissue at the periosteal region had 35% higher mineral:matrix ratio, as well as 44% lower carbonate:mineral ratio than the new tissue at the endocortical region of the loaded tibiae of young mice (Figure 43).

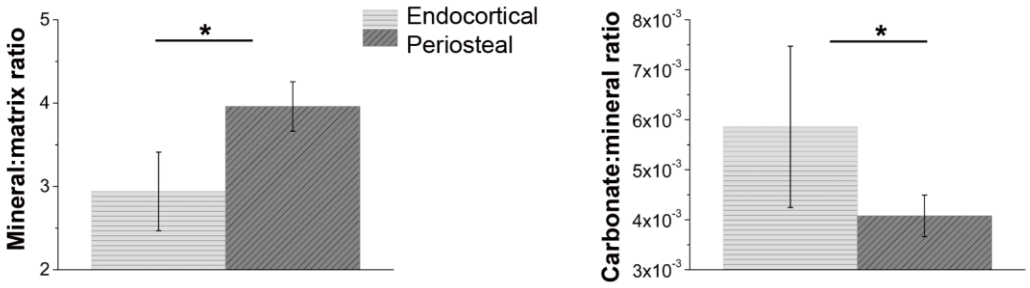

Figure 43: Mineral:matrix ratio and carbonate:mineral ratio of the newly formed tissue at the endocortical and periosteal region of the loaded tibial midshaft of 10 week old mice (bars are standard deviations of n = 5 mice; * = significant difference).

Do mineral and matrix properties of the newly formed bone with additional in vivo loading change with animal age?

As exemplified in Figure 44, no trend was detected in mean mineral thickness and also in degree of mineral alignment in the newly formed tissue from additional *in vivo* loading with animal aging. This was the case for both endocortical and periosteal regions.

As previously mentioned, the amount of newly formed tissue at the endocortical and periosteal regions of the tibiae of adult and elderly mice was relatively low, in comparison with the spatial resolution of the FTIRI (6.25 µm). Therefore, it was not possible to reliably study how the different FTIRI parameters change with animal age in the newly formed tissue of the loaded tibia.

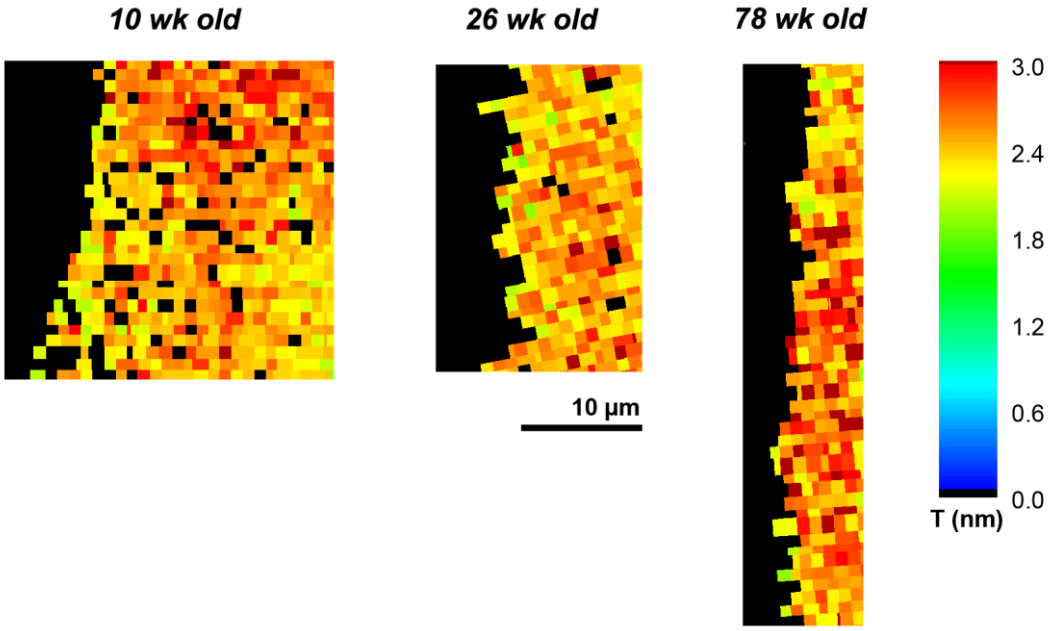

Figure 44: T parameter of the newly formed tissue at the periosteal region of the loaded tibial midshaft of 10, 26 and 78 week old C57BL/6J mice.

4.2.6 Relationship between mineral properties and calcein labeling in mineralizing bone surfaces

The overlay of T and ρ parameter maps (1 µm spatial resolution) of the tibial samples with respective backscattered (BSE) and fluorescence microscopy images, allowed the detection of very specific patterns, which would otherwise possibly not be recognized. In particular, distinct T and ρ parameters were attributed to the areas where the fluorochrome label calcein was located. These were areas with lower mean mineral thickness and degree of mineral alignment than the surrounding bone tissue. By plotting T and ρ parameters along the first 30 µm from the bone surface, a peak of low T and ρ was detected at approximately 30, 15 and 8 µm in tibia from 10, 26 (Figure 45A and C) and 78 week old (Figure 45B and D) mice, respectively. This peak was shown to correspond to the location of the calcein label itself, after correlating T and ρ parameter maps with fluorescence microscopy images. The loaded tibia of one 10 week old mouse with a diffuse calcein label did not adhere to this same pattern.

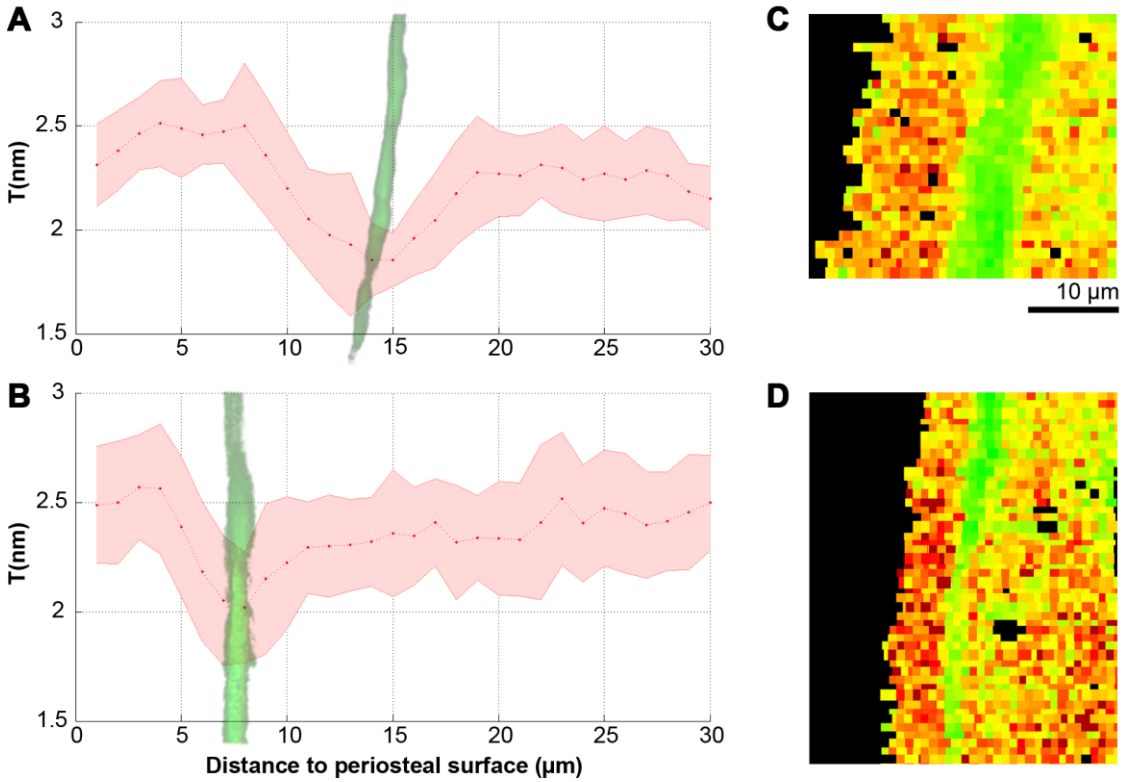

Figure 45: Graph of the T parameter profile 30 µm through the cortex starting at the periosteal surface in the loaded tibiae of a A) 26 week old and a B) 78 week old mouse and respective C), D) T parameter map of the first 30 µm of the tibial sections. The red line in the graphs corresponds to the average T parameter and the shadowed pink area above and below the line represents the standard deviation [294].

4.2.7 Mineral in the vicinity of blood vessels

Lower mean mineral particle thickness (Figure 46A) and lower degree of alignment of mineral particles (Figure 46B) was detected in the vicinity of blood vessels. This pattern was observed around all the scanned blood vessels of both loaded and control limbs, and for mice of all ages: 10 (3 blood vessels), 26 (1 blood vessel) and 78 (2 blood vessels) week old mice.

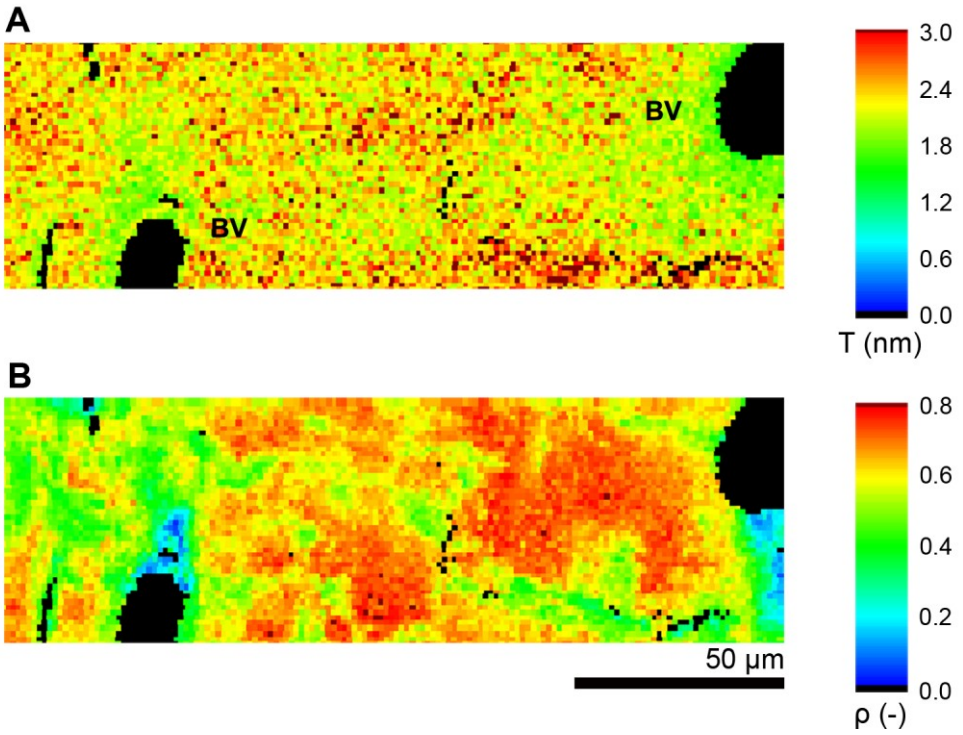

Figure 46: Lower A) T parameter and B) ρ parameter near blood vessels in the control tibia of a 10 week old mouse; BV = blood vessel [294].

In parallel with this finding, a lower degree of mineralization was detected around blood vessels in BSE images of both loaded and control tibiae of animals of all ages (Figure 47).

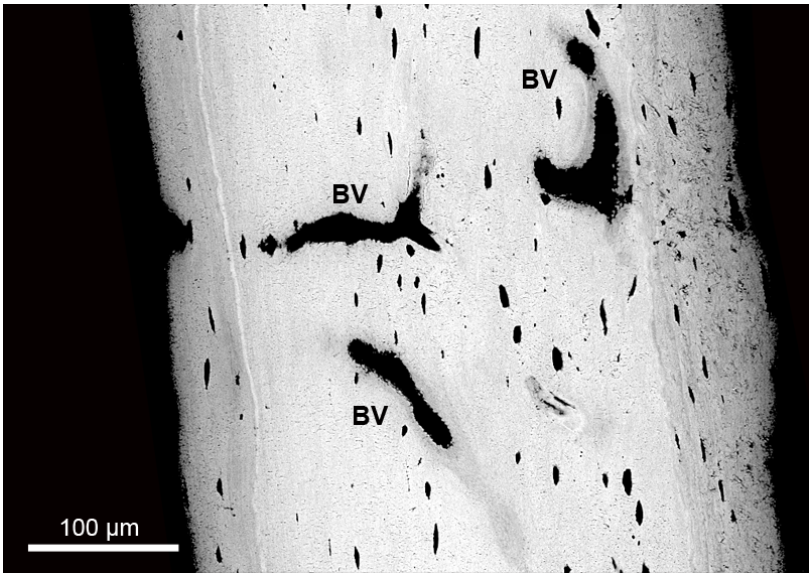

Figure 47: BSE image of a control tibia of a 26 week old mouse. Lower degree of mineralization can be seen around the blood vessels; BV = blood vessel.

4.3 Cortical bone osteocyte lacuno-canalicular network (LCN) and perilacunar tissue

4.3.1 The effect of *in vivo* loading on the topology of the osteocyte LCN of newly formed bone

Overviews of the loaded (*in vivo* loading superimposed on physiological loading) and control (physiological loading) tibiae of three young 10 week old mice were obtained with confocal laser scanning microscopy (CLSM), after staining of the osteocyte LCN with rhodamine (Figure 48).

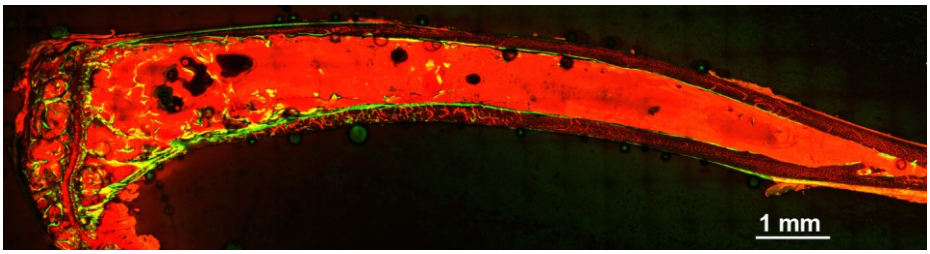

Figure 48: CLSM image of the control tibia of a 10 week old mouse rotated 90^0 in relation to bone's longitudinal direction (on the left would be the knee joint). Calcein labels can be observed in green color.

The overview images of the tibiae, allowed identifying regions where double calcein labeling, indicative of formation of new bone tissue, was present. The selected regions were imaged with CLSM with high magnification (100x) and the new tissue located between calcein labels (Figure 49) was isolated and analyzed.

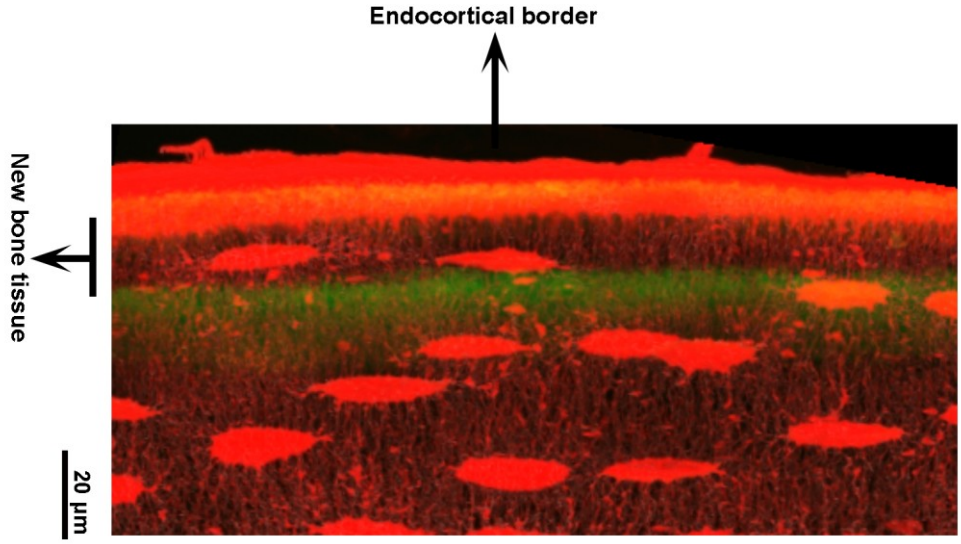

Figure 49: Projection of a series of CLSM images (z-stacks) at the control tibial midshaft of a 10 week old mouse. The new bone tissue is located between the calcein labels.

CLSM images of the tissue located between calcein labels in both the loaded and the control tibiae of three young 10 week old mice were processed and different parameters of the osteocyte LNC were quantified. The volumes of the regions analyzed were approximately 75500 μm^3.

The canalicular density corresponded to the total length of the canaliculi within the unit of tissue volume. For all the three analyzed samples, the canaliculi density was higher in the new tissue formed with additional *in vivo* loading, than in the new tissue formed only with physiological loading (Table 6).

	Canalicular density ($\mu m/\mu m^3$)		
New tissue (loaded limbs)	0.285	0.225	0.103
New tissue (control limbs)	0.093	0.068	0.089

Table 6: Canalicular density of the new tissue at the loaded and control tibiae of three different 10 week old mice. Each column in the table corresponds to one different animal.

In addition, the degree of the nodes, which is the number of canaliculi meeting at a node was calculated and the cumulative node degree distribution was plotted to quantify the connectivity of the network (Figure 50). The slope of the curves in the semi logarithmic plot was steeper for the new tissue in the control tibiae, when compared to the new tissue in the loaded tibiae, i.e. the local connectivity of the network was higher when the tissue was formed under additional loading. The network of the new tissue formed with additional loading had 28% of nodes with a degree above 4, while this value was only 13% for the network of the physiologically loaded tissue.

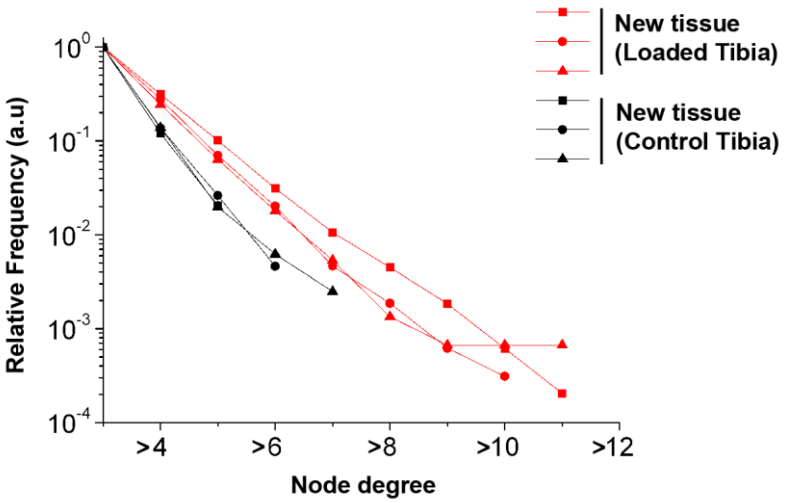

Figure 50: Graph of the decay of the cumulative node degree distribution in the new tissue at the loaded and at the control tibiae of three different 10 week old mice. The cumulative distribution establishes that the value of the probability for the degree of a specific node includes also all larger degrees. Each symbol represents a different animal.

The decay of the cumulative canalicular length distribution is shown in Figure 51 for the three studied control and loaded tibiae of young mice (Figure 51). Similar to what was seen for the decay of cumulative node degree distribution, the slope of the curves of the loaded and control tibia was different, but this time the trend between the two tibiae was reversed. The probability to find longer canaliculi was now higher in the new tissue in the control tibiae, than in the new tissue in the loaded tibiae. While in the new tissue in the control tibiae 38% of all the canaliculi had length above 3.25 μm, only 22% of the canaliculi in the new tissue in the loaded tibiae had a length above this value.

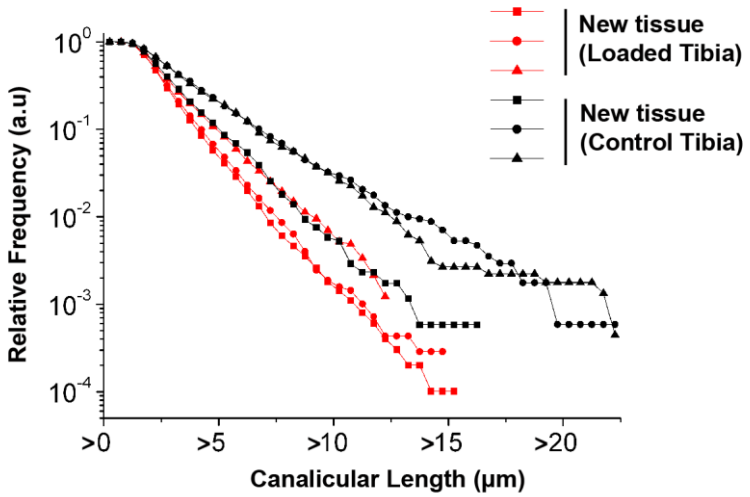

Figure 51: Graph of the decay of the cumulative canalicular length distribution in the new tissue at the loaded and at the control tibiae of three different 10 week old mice. Each symbol represents a different animal.

4.3.2 The mechanical properties of the perilacunar tissue

The overview of the loaded tibia of an adult 26 week old mouse was obtained with BSE imaging (Figure 52A), as well as higher magnified images of the tibial midshaft (Figure 52B). This way, it was possible to pre-select 5 different osteocyte's lacunae for nanoindentation to study tissue's elastic modulus and hardness in their vicinity. The lacunae chosen were located within the center of the bone and had no other lacunae in very close proximity. In Figure 52C one of the selected osteocyte's lacuna located at the midshaft and the performed indents can be seen.

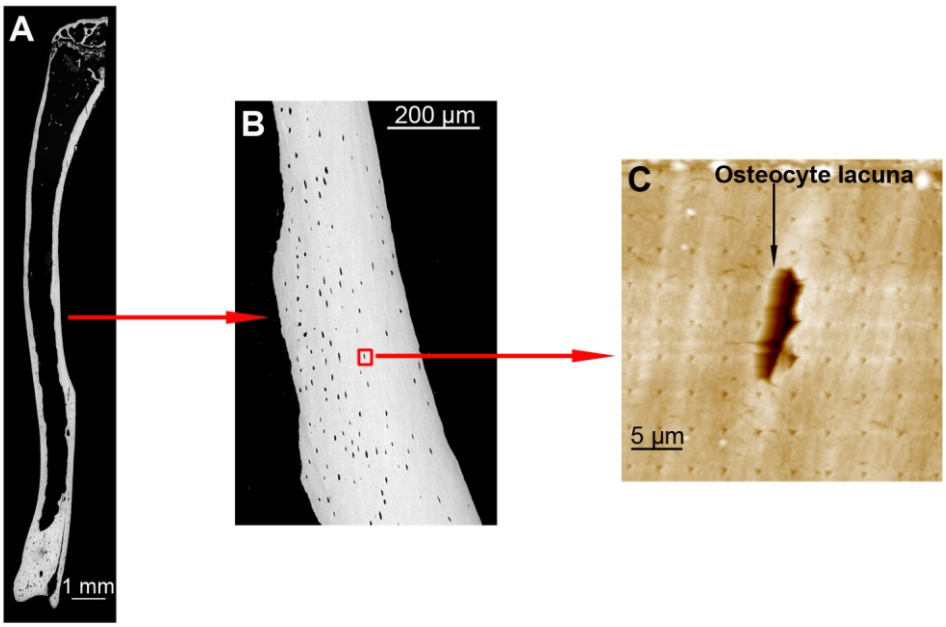

Figure 52: A) Overview of a loaded tibia of a 26 week old mouse obtained by merging a series of BSE images, B) Magnified BSE image at the tibial midshaft; osteocyte lacuna chosen to be indented at the intracortical region is squared in red, C) Topographic image of the bone surface after indentation in the vicinity of the osteocye lacuna. Indents were performed with a spacing of 3 µm between each other.

The averaged bone tissue located 0 to 3 µm away from the lacunae had a higher elastic modulus and hardness, than the tissue located further away from the lacunae, 9 to 18 µm away (Figure 53).

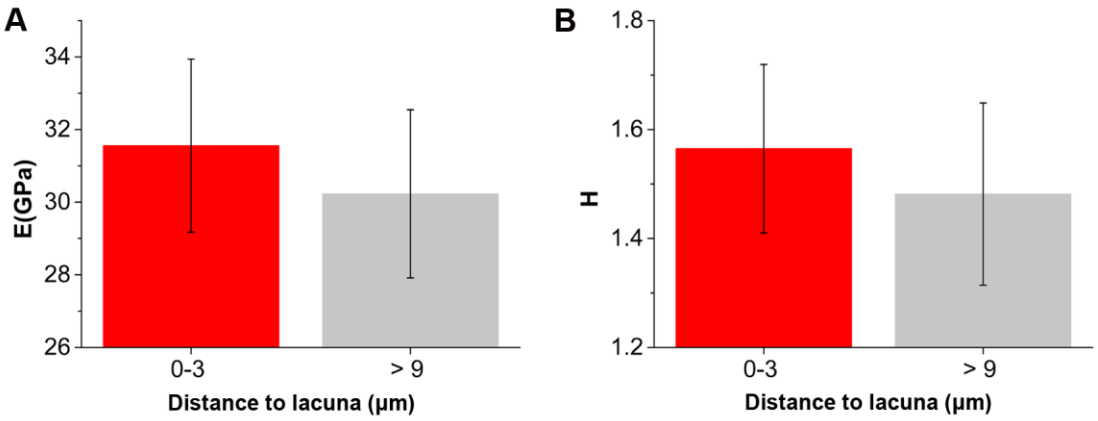

Figure 53: A) Elastic modulus and B) hardness of tissue located up to 3 µm away and tissue located more than 9 µm away from osteocyte lacunae at the intracortical region of the loaded tibia of one 26 week old mouse (bars are standard deviations of n = 5 lacunae).

5 Discussion

The overall goal of this dissertation was to investigate the influence of age and mechanical loading on bone structure and material properties. The first aim of the thesis was to analyze the effect of loading on cortical bone mass, geometry, and material quality and determine how animal age modulates the adaptive response to additional *in vivo* mechanical loading. The second aim was to study the influence of animal age and tissue age on cortical bone mass, geometry, and material quality during normal physiological loading.
An *in vivo* model was used, in which controlled axial loads were administered to the tibia of mice. The adaptive changes occurring at the midshaft were compared to those from the contralateral tibia that did not undergo additional loading (only weight-bearing from ambulation of the mouse in between daily loading sessions). The analysis was performed in female post-pubescent 10 week old, adult 26 week old and elderly 78 week old C57BL/6J mice.

In contrast to skeletal aging in humans, mice do not normally undergo Haversian remodelling, and they do not have spontaneous fractures. However, similar to humans, mice experience cortical and trabecular age-related bone loss [295]. The only animal model reported to have a skeletal maturation similar to human females, is the rhesus monkey [296]. Access to nonhuman primates is however very restricted and thus the mouse serves as an adequate, commonly used model to characterize skeletal aging. The choice of the mouse strain was based on previous loading and unloading studies [165, 175, 297] which demonstrated the increased mechanoresponsiveness of C57BL/6J mice, when compared to other mouse strains. The choice of young postpubescent 10 week old, adult 26 week old and elderly 78 week old mice allowed obtaining a broader understanding of skeletal maturation and bone adaptation to mechanical loading, as three main and distinct stages of the mouse lifespan (approximately 2 years) were studied. In the C57BL/6J mice, peak adult bone density was shown to be achieved at 16 weeks of age [298] and peak bone strength was attained before 20 weeks of age [299]. Therefore, 26 week old mice, in contrast to the 10 week growing mice, are skeletally mature and going already through age-related osteopenia, while the elderly 78 week old mice have a greatly reduced bone mass in comparison with 10 and 26 week old mice. Finally, this study was performed in female mice as this would allow for the role of estrogen to be considered in future studies of skeletal aging.

5.1 The effect of additional *in vivo* mechanical loading on cortical bone mass and geometry

One of the possible causes of age-related bone loss is a decrease in bone's mechanoresponsiveness with aging. However, the impact of aging on the skeletal response to mechanical loading is still a matter of discussion and investigation. As part of the first aim of this thesis, cortical bone mass and geometry were characterized after two weeks of *in vivo* mechanical loading of the tibiae of 10, 26 and 78 week old mice.

Cortical bone mass and geometry were enhanced by *in vivo* controlled loading in mice of all three ages (young, adult and elderly). In both young and adult mice, the onset in the response

of cortical bone to loading occurred at the same time, with increases in cortical bone area (Ct.Ar) and cortical thickness (Ct.Th) apparent by day 10. In elderly mice, the response of cortical bone to loading started earlier, at day 5. At day 15, Ct.Th was 13%, 18% and 6% and Ct.Ar 13%, 9% and 8% higher in the loaded limbs than in the control limbs in young, adult and elderly mice, respectively. Different groups have reported similar magnitudes of load-induced increases in cortical bone in young and adult mice [178, 270, 300]. Lynch et al. [249] reported a larger overall response to loading, with increases in Ct.Ar of +48% and +40% in 10 and 26 week old female C57BL/6 mice, respectively. The difference between the current work and their study might be related to the greater number of cycles used in their *in vivo* loading protocol (1200 cycles/day compared to 216 cycles/day in this work) and the larger strain (2300 με compared to 1200 με in this work) induced at the tibial midshaft. Brodt et al. [270] reported 5% and 7% load-induced increase in Ct.Ar, and no increase and an increase of 7% in Ct.Th in adult and elderly mice, respectively. Although the load-induced changes in Ct.Ar and Ct.Th in elderly mice were similar to the changes detected in the present study, in adult mice the changes were not as pronounced as the ones detected in the current study. Considerable differences existed between the two studies, such as the levels of strains engendered at the tibia and the use of different mice species. An interesting finding was that only for elderly mice, cortical volumetric tissue mineral density (Ct.vTMD) was higher in the loaded limbs than in the control limbs. Comparable results were obtained by Silva et al. [301], who reported that load-induced changes in Ct.vTMD occurred in 7 and 12 month old, but not in 2 and 4 month old mice. All the histomorphometric bone formation indices (except indices associated with single labeled surfaces) were enhanced by loading in young and adult mice, although to a lesser degree in the adult mice. In elderly mice, differences in the histomorphometric parameters between loaded and control limbs didn't reach significance.

Previous exercise studies have had conflicting results when assessing the influence of age on mechanoresponsiveness, ranging from enhanced [245, 250], unchanged [220, 269, 271] or decreased [243, 248] response to mechanical loading in elderly animals. Earlier controlled loading studies reported mainly a reduction in bone's response to loading with aging [244, 246, 247]. These studies were limited by the usage of non-physiological loading direction or the usage of invasive loading models. In the current study, a controlled non-invasive loading model which applies loads in a physiological direction was used. The interlimb differences (loaded limb − control limb) of the cortical bone microCT parameters indicated that there was no reduction in the mechanoresponsiveness of cortical bone between young and adult or between adult and elderly mice. However, the interlimb differences of Ct.Th and cortical area fraction (Ct.Ar/Tt.Ar) showed that there was a significant reduction in bone's adaptive response to loading between young and elderly mice. Interestingly, when considering interlimb differences of Ct.vTMD, mechanoresponsiveness seemed to increase in elderly mice, when compared to young and adult mice. Different histomorphometric indices indicated no change in mechanoresponsiveness between young and adult mice, although periosteal mineral apposition rate (Ps.MAR) and periosteal bone formation rate (Ps.BFR/BS) showed a reduction in response and endocortical mineralizing surface (Ec.MS/BS) and Ec.BFR/BS an increase in response, between young and adult mice. These results indicated that there was a greater response periosteally in young mice and endocortically in adult mice. Lynch et al. [249, 302] attributed the greater periosteal

response in young mice, to the fact that in adult mice smaller increases in Ct.Th by periosteal bone deposition are needed to increase the bending resistance to levels comparable to the young mice, as adult mice have greater periosteal perimeter. The interlimb differences in Ec.MS/BS, Ec.MAR and Ec.BFR/BS of adult and elderly mice, indicated a reduction in bone's mechanoresponsiveness in elderly mice. Most of the periosteal bone formation indices could not be analyzed for elderly mice because of the almost lack of double-labeled bone. Holguin et al. [272] also reported a decrease in mechanoresponsiveness in elderly mice and no change in MAR and BFR/BS with loading, but an increase in periosteal mineralizing surface. In their study, higher mechanical strains were induced at the tibial midshaft, 2200 με than in our study, 1200 με, which could explain the differences between studies. Contrary to the present study, Brodt et al. [270] reported increased response to loading in the endocortical surface and no change in the periosteal surface in aged mice, when compared to middle-aged mice. As previously mentioned, a different mice species and different strain tibial levels were used in Brodt et al. [270] study, when compared to this study.

Although some of the studied histomorphometric parameters indicated reduced mechanoresponsiveness in elderly mice, the microCT parameters revealed that the relative response (interlimb differences) of elderly mice to mechanical loading was not significantly different to the response of adult and young mice, except in terms of Ct.vTMD. These data indicates that in elderly mice, loading helped maintaining bone mass during the 15 days of the *in vivo* loading in the loaded tibiae, which otherwise would have gone through bone loss (as observed in the control limbs), possibly by an increase in cortical bone's mineralization degree. Although the static microCT analysis performed in the current study did not show a reduced cortical bone adaptive response to loading already in adulthood, recent work from our research group [303] using a newly developed technique (3D dynamic *in vivo* morphometry) has shown a reduced mechanoresponsiveness with aging. Unlike the static microCT measurements that only show the net bone volume fraction, the new method allows for direct measurement of resorbed and formed volumes, surface areas, and mineralizing thickness/erosion depth of bone over time. These recent data from our group indicate that there was a significant reduction in the bone formation (mineralizing volume/bone volume and mineralizing thickness) response to loading with age. Interestingly, the formation surface with mechanical stimulation is the only effect of loading conserved into old age. The data also showed that loading had no influence on erosion thickness in all age groups.

5.2 The effect of additional *in vivo* mechanical loading on cortical bone mineral and matrix properties

To get a broader understanding of the adaptive response of cortical bone to mechanical loading and how this response changes with animal age, it was essential to assess also the effect of mechanical loading on the quality of bone tissue. Bone quality is a broad term, which comprises bone's microarchitecture (trabecular microarchitecture and cortical porosity), the number and frequency of microcracks and also material properties, such as mineral particle size and perfection and collagen maturity. Very few studies have assessed load-induced changes in bone quality and the ones which did measured changes after exercise regimens, characterized

by a lack of controlled loading parameters. In this study, synchrotron sSAXS was used to measure the thickness and degree of alignment of bone's mineral particles with a spatial resolution of 1 μm. In addition, with FTIRI bone's degree of mineralization, mineral crystallinity, the percentage of inclusions (carbonate and acid phosphate) in mineral, as well as collagen maturity were assessed with an approximate spatial resolution of 6 μm.

The results obtained indicate that the effect of additional controlled *in vivo* loading on bone composition varied with animal age, as load-induced changes were predominantly observed in elderly mice. Controlled *in vivo* loading led to an increase in collagen maturity in all the studied regions (endocortical, periosteal and intracortical) in elderly mice, although only significantly in the intracortical and periosteal regions. In addition, there was an increase in mineral:matrix ratio at the endocortical and intracortical regions of the loaded tibiae of elderly mice, when compared to the control tibiae. This difference was not significant for the intracortical region, but while between the loaded tibiae of adult and elderly mice mineral:matrix ratio increased, between the control tibiae there was no change. This result is further strengthened by the microCT data showing significantly increased Ct.vTMD in the loaded tibia (compared to control tibia) of elderly mice after 15 days of *in vivo* loading. In contrast to the findings in elderly mice, bone composition was largely unaltered by loading in young mice, since only significantly greater acid phosphate content (at the intracortical region) was measured. The change in acid phosphate absolute values was very small: 0.45 in the loaded tibiae vs 0.44 in the control tibiae. Similarly in adult mice, only mineral crystallinity and acid phosphate content (both at the periosteal region) were enhanced by controlled loading. The sSAXS analysis didn't reveal any trend of alteration in the T and ρ parameters of bone's mineral with additional *in vivo* mechanical loading.

The significant increase in bone collagen maturity in the periosteal and intracortical regions after *in vivo* loading in elderly mice is intriguing. Alterations in collagen of both new and pre-existing bone tissue after exercise regimens in rodents were previously speculated to occur by different authors [273, 304, 305]. Their speculations were based on the enhancement of bone post-yield structural and tissue-level mechanical properties after exercise, but their studies were focused mainly in young rodents. However, Raab et al. [271] showed an increase in femoral ultimate stress in exercised (10 weeks of treadmill running) elderly rats, when compared to sedentary controls. Two studies by Isaakson et al. [224, 225] assessed the tensional properties of the collagen network, collagen content and collagen cross-links in young, adult and elderly C57BL/6 male mice after voluntary exercise (access to a running wheel beginning at age 1 month old). In contrast with the results obtained in this work of load-induced enhanced collagen maturity only in the elderly C57BL/6J female mice (no effect was measured in young or adult mice), Isaksson et al. [224, 225] measured no difference in the collagen content or cross-links between running mice compared to sedentary controls of any age. In addition, the authors reported that exercise led to improved tensional properties of the collagen network in young mice, but not in adult or elderly mice. It is difficult to establish comparisons between the current study and their work, since in this study strain-matched controlled loading was used over 15 days, whereas the previous studies included 1 to 17 months of voluntary exercise, which likely engendered different strain levels in the tibia during physical activity for the different aged mice. In addition,

Isaksson et al. [224, 225] studied male mice, while in this work female mice were analyzed. Unfortunately, besides the above mentioned investigations, no others studies have examined the effect of altered loading conditions on bone composition in elderly animals.

It is possible to speculate that the increase in bone's collagen maturity after controlled *in vivo* mechanical loading in elderly mice is a mechanism of enhancement of bone's mechanical properties achieved by stabilization of collagen through conversion of immature to mature enzymatic cross-links. Different studies have reported how mature enzymatic collagen cross-links are positively associated with bone's post-yield mechanical properties and even with pre-yield mechanical properties [127, 306-308]. An *in vitro* study reported that an increase in pyrdinoline (PYD) and deoxypyridinoline (DPD) (mature cross-links) of bovine bone correlated with an increase in bone's ultimate stress and post-yield energy absorption [127]. Inhibition of lysil oxidase (LOX)—enzyme responsible for cross-linking formation—in rats which induced a decrease of 45% in pyridinium cross-links was associated with a 26% and 30% decrease in cortical bone bending strength and modulus, respectively [308]. The association of collagen cross-links with bone's mechanical properties is however still controversial and the existing studies on the topic are not always consensual [119]. Additionally, it is not yet clear how mechanical loading impacts the collagen cross-linking profile, although there are indications that mechanical loading and collagen maturity are associated. The content of mature collagen cross-links is higher in weight bearing bones than in non-weight bearing bones in individuals up to 40 years old [122]. In addition, osteoblastic cells showed a higher conversion rate of immature to mature collagen cross-links under hypergravity, but a decreased rate under microgravity [309]. Furthermore, exercise and axial tibial compression in mice were shown to increase expression of periostin [310], which is known to be involved in the activation of LOX, the enzyme responsible for cross-linking formation [311]. Nevertheless, it is difficult to explain the mechanism behind the detected increase in both collagen maturity and mineralization in the intracortical region of the loaded tibia and also why this effect was only present in elderly mice. A recent study which assessed gene expression after *in vivo* tibial loading of 2, 4, 7 and 12 month old mice revealed that a series of osteoblast/matrix genes increased between loaded and control limbs, only in the older mice [301]. This finding might be associated with the load-induced changes detected only in elderly mice in this study. Our research group is also looking at the role of SOST/sclerostin in the anabolic response to mechanical loading as a function of age.

5.2.1 Mineral and matrix properties of newly formed tissue with additional *in vivo* loading

The new tissue formed with additional *in vivo* loading was characterized by studying its mineral and matrix properties with synchrotron sSAXS and FTIRI. Interestingly, when comparing new tissue formed in the loaded limbs with new tissue formed in the control limbs of the 10 week old mice; the age group that had the largest amount of new bone tissue laid down during the experimental period, no change in mineral and matrix properties was detected. This finding suggests that two weeks of controlled *in vivo* loading increased the rate of bone formation as confirmed by histomorphometric measurements, but the newly formed bone in response to *in*

vivo loading does not have altered mineral and matrix properties, when compared to bone formed during physiological loading. These results indicate that bone tissue formed during controlled loading does not compromise bone quality, which in exercised adult humans might influence the patient's risk of fracture. This is an important finding since mechanical loading has been seen as a promising treatment strategy to combat age-related bone loss. It was previously unclear whether the increased mineral apposition rate, due to the mechanical loading regime, altered the bone quality since earlier studies have shown that bone tissue rapidly formed via intramembranous ossification during healing has altered mineral and matrix properties [231, 232]. In 1981, Woo et al. [233] suggested that the new bone material that formed in pig femora during a 12 month exercise program had a similar quality to the original bone. However, in their measurements it was not possible to directly distinguish between new and old bone tissue. In the literature, it seems like no other study has compared how controlled *in vivo* loading (superimposed onto physiological loading) affected the mineral and matrix properties of newly formed tissue. Furthermore, no other study investigated whether the quality of the new tissue formed with controlled *in vivo* loading was altered with animal age. In this work, after isolating the new tissue in the loaded tibiae of young, adult and elderly mice (using calcein labeling), sSAXS measurements (1 μm spatial resolution) indicated that the new tissue formed in the loaded tibiae had the same mean mineral thickness and mineral degree of alignment across all animal ages.

Surprisingly, the new bone tissue formed in the periosteal region of bone at the tibial midshaft was composed of thicker and more highly aligned mineral particles than the new tissue formed in the endocortical region. Imaging the tibial midshaft with second harmonic generation by multiphoton confocal microscopy suggested that new the tissue at the periosteal region was composed of more highly aligned collagen fibers than the new tissue at the endocortical region of the tibial midshaft of young mice. This seems to coincide with the increased degree of mineral alignment detected at the periosteal region (when compared to the endocortical region), as it is known that mineral particles tend to follow the orientation of collagen. Similarly, a study of human femora and nonhuman primate ulna and humerus showed that transversely oriented collagen fibers increased along the endocortical margin of the bone, while closer to the periosteal margin, collagen fibres were mainly longitudinally oriented [312]. Furthermore, results from our group suggested that the periosteal region of bone experiences higher strain levels than the endocortical region during controlled *in vivo* loading [313], which might be associated with the detected thicker and more aligned mineral particles in the periosteal region.
Finally, in the loaded and control tibia of young mice, lower mineral:matrix ratio (significantly lower only in loaded tibia) and higher carbonate:mineral ratio was detected at the periosteal region, when compared to the endocortical region. This data suggests that the periosteal region was more mineralized and thus the endocortical region was composed of younger bone, which is reflected in the greater mineral apposition rate at the endocortical compared to the periosteal region.

5.3 The topology of the osteocyte lacuno-canalicular network (LCN) and perilacunar material quality

The effect of mechanical loading on the osteocyte LCN was assessed by comparing the topology of the osteocyte LCN between newly formed tissue with additional *in vivo* loading and newly formed tissue only with physiological loading. A functional osteocyte LCN is crucial to maintain the integrity of bone as a tissue, as osteocytes are known to play a central role in the process of mechanical adaptation by sensing mechanical stimuli.

The new tissue formed at the control and at the loaded tibiae of young 10 week old mice was identified with calcein labeling and its osteocyte LCN was analyzed with CLSM, after staining with the rhodamine dye. The tissue analyzed had between 3 and 12 days, since calcein was administered at day 3 and 12 of the experiment and the tibiae were collected at day 15. Interestingly, the topology of the osteocyte LCN was different between the new tissue formed in the loaded tibiae and the new tissue formed in the control tibiae. Specifically, the osteocyte LCN of the new tissue in the loaded tibia was denser and had higher degree of canalicular branching (higher node degree, which is the number of canaliculi connecting at a node) and possibly, because of that, higher percentage of lower canaliculi length, when compared to the osteocyte LCN of the new tissue in the control tibia. In short, the loading resulted in a more strongly interconnected osteocyte LCN. It is interesting to correlate this result with the fact that, even if not pronounced, there was an increase in the mineral degree of alignment in the new tissue of the loaded tibia, when compared to the new tissue of control tibiae.
The detected alterations in the osteocyte LCN might be a result of the increased (approximately three times greater) mechanical strain imposed on the loaded tibia, in comparison with the physiological strains during normal activity in the control tibia. In the last years, the osteoblast-osteocyte transition has been shown to be an active [314, 315], rather than a passive process, as previously thought. For example, the formation of dendrites was shown to be dynamic [315, 316] and the dendrites were shown to retain their capacity to retract and extend [314]. It's possible to speculate that the newly formed tissue in the loaded tibia which developed its osteocyte LCN in response to distinct loading patterns than the network in the control tibia, formed a more comprehensive and detailed osteocyte network adapted to the enhanced mechanical environment. However, such conclusions could only be established after analyzing the living cells, the osteocytes and its dendrites. These findings have to be interpreted with caution, due to the reduced number of regions analyzed. Nevertheless, different studies have suggested before that mechanical loading had an impact on the osteocyte LCN architecture and morphology. The presence of loading during development was related to more organized networks [185, 186, 317], more spindle-shaped lacunae [185, 317] and higher osteocyte densities [318-320]. In addition, Himeno-Ando et al. [321] reported that the osteocyte network of the tibia, long bone loaded mainly along the longitudinal direction, had more cellular processes and branches than the osteocyte network of the parietal bone, which is usually loaded radially and tangentially and Sugawara et al. [317] reported larger number and length of dendrites in 6 week old mice than in embryonic mice.

The tissue that directly surrounds the lacuna of osteocytes, the perilacunar tissue, is thought to constitute a unique microenvironment, which material properties might have an impact in the local lacuna strain field and the mechanical signal reaching the osteocytes. Different studies have suggested that the osteocyte is able to change its microenvironment, as it was shown, for example, in female C57BL/6 mice after two weeks in microgravity conditions [215]. The current work intended to study whether perilacunar tissue mechanical properties change with animal age (which could be associated with changes in bone's mechanoresponsiveness) and whether mechanical loading could reverse these changes.

The performed nanoindentation measurements at the *in vivo* loaded tibial midshaft of an adult mouse (3 μm spacing between indents) revealed that bone tissue up to 3 μm away from the osteocyte lacuna had higher elastic modulus and hardness than tissue more than 9 μm away from the lacuna. Potter [322] showed a trend of increased elastic modulus in tissue up to 5 μm away from the lacuna, when compared to tissue further away in bone, in young and old baboon femora. In addition, Nicolella et al. [323] showed that the perilacunar tissue was stiffer than tissue further away in bone in ovariectomized rats, but not in control rats. However, very recent studies based on synchrotron phase-nano computed tomography suggested that the gradients in the material properties of the tissue surrounding both osteocyte lacunae and canaliculi can be as small as 500 nm [218]. Continuing the proposed study on load- and age-related changes in bone's perilacunar tissue mechanical properties would have required the usage of very small indent spacing in the nanoindentation measurements, which is technically very challenging.

5.4 The effect of animal age on cortical bone mass and geometry during normal physiological loading

The second aim of this thesis was to analyze the influence of animal age on bone mass, geometry and quality. Cortical bone mass and geometry were initially measured, followed by an analysis of the properties of bone's basic constituents, the mineral and the collagen, in female post-pubescent 10 week old, adult 26 week old and elderly 78 week old C57BL/6 mice.

Different studies have previously assessed changes in bone mass and geometry with aging in mice and other species. Nevertheless, some inconsistencies have been reported on the growth patterns of bone after puberty. In this study, age-related changes in cortical bone mass and geometry were assessed by performing *in vivo* microCT and dynamic histomorphometry. Between young and adult mice, Ct.Ar, total cross-sectional area inside the periosteal envelope (Tt.Ar), Ct.Ar/Tt.Ar, Ct.Th and principal moments of inertia (Imax and Imin) increased. The increase in these parameters likely reflects the bone acquisition still occurring after sexual maturity (puberty occurs at 6-8 weeks of age) in these mice. In fact, reports [298, 299] suggest that skeletal maturity (peak bone mass and density) in the mouse femur is achieved between 16 and 20 weeks of age. In addition, the histomorphometric data revealed that the amount of new bone laid down is reduced in adult animals, when compared to young animals. Between adult and elderly mice, Ct.Ar, Ct.Ar/Tt.Ar, Ct.Th, Imax and Imin decreased, while Tt.Ar remained constant, reflecting the loss of bone mass with advanced age. The limited number of double

calcein labeling in the tibia of elderly mice restricted the comparison of histomorphometric parameters between adult and elderly mice.
Different authors reported an increase in Ct.Ar of long bones between post-pubescent (or even younger mice) and adult female and male C57BL/6 mice [299, 324-327]. However, the changes observed in Ct.Ar after adulthood were not as consistent, with different groups describing either a stabilization [324-326] or, similar to what observed in this study, a decrease in Ct.Ar between adult and elderly C57BL/6 mice [180, 327]. From human studies, it is thought that in women, Ct.Ar decreases with advancing aging, while in men it remains constant [328]. Together with an increase in the moment of inertia, the constancy of Ct.Ar with advanced age in men might reflect bone remodeling patterns that compensate for the deterioration of bone's material properties. One of the referenced groups [326] reporting no notable age-related changes after adulthood in Ct.Ar studied only male mice, which might explain the difference between their and the current study. However, it's not clear why Glatt et al. [324] and Somerville et al. [325] who studied female mice saw no change in Ct.Ar after adulthood. The increase detected in this study in Ct.Th between young and adult mice or the decrease between adult and elderly mice was previously reported by different groups [180, 299, 324, 326]. The Tt.Ar (includes both bone marrow and cortical bone) of the tibia was shown, in this study, to increase only up to adulthood, just as in the study of Somerville et al. [325] and the study of Patel et al. [180], who analyzed the tibial midshaft of female C57BL/6 mice, as well. However, Buie et al. [327] using an identical study design saw a trend of decrease of the tibial Tt.Ar (it's not reported whether the results are significant). The parameters Imax and Imin reflect the resistance of bone to bending and are influenced by how much bone there is and how it is distributed. The increase of both parameters between young and adult mice and the decrease between adult and elderly mice likely relate to the correspondent changes in Ct.Ar/Tt.Ar between the studied ages. A large number of studies reported age-related changes of a different moment of inertia, the polar moment of inertia, which reflects bone's torsional rigidity. In addition, Brodt et al. [299] showed an increase in the femoral medial-lateral and anterior-posterior moment of inertia in mice between 4 to 20 weeks old (24 weeks old was the maximum age studied) and Akkus et al. [85] in rats aged 3 to 24 months old.

Although in this work, age-related changes in the different cortical bone microCT parameters were not directly correlated to bone's mechanical properties at the whole bone or tissue level, several studies attest to the relevance of understanding how these parameters are altered with advanced age. As an example, Voide et al. [329] reported that pre-yield murine femoral mechanical properties could be predicted for a large part by bone volume, cortical thickness, cross-sectional area and total area and that none of these parameters could explain post-yield properties (they related it to collagen properties and microdamage accumulation). The conclusions arising from studies relating bone mass and morphology and bone's mechanical properties are highly dependent on a series of variables, such as the kind of mechanical test performed, the species used, the anatomical location studied. It is also not linear to isolate the contribution of a single parameter, as they tend to correlate among each other. It is, however, clear that it is essential to assess, not only bone mass and geometry, but also its quality, including the properties of its basic elements, the mineral and collagen, in order to get a broader

understanding of how bone changes with age and how that might impact is mechanical properties.

5.5 The effect of animal age on cortical bone mineral and matrix properties during normal physiological loading

To determine the age-related changes in bone mineral and matrix properties, the intracortical region at the tibial midshaft of control limbs of 10, 26 and 78 week old female mice was measured with synchrotron sSAXS and FTIRI.

An increase in mineral:matrix (approaching significance) was detected only between young and adult mice, but not between adult and elderly mice. A series of studies have reported a similar increase in the degree of mineralization up to adulthood [81-84]. However, after adulthood, different studies show either increased [85, 86, 96], constant [330] or decreased [83] degree of mineralization. The results obtained in this study indicate that only up to adulthood there is an increase in bone's degree of mineralization and not after this stage of life. Not surprisingly, the Ct.vTMD obtained with microCT, followed a similar trend with aging, increasing significantly between young and adult mice and stabilizing afterwards. The changes in carbonate substitution in bone's mineral particles with aging followed a similar trend as the degree of mineralization. The carbonate:mineral ratio (indicator of carbonate substitution in bone mineral) increased between young and adult mice, while between adult and elderly mice there was only a trend of decreased carbonate:mineral ratio, which was not significant. The results reported in the literature on the age-related changes in carbonate content are not consistent. The data obtained in this study supports the results obtained by Burket et al [84], who showed that carbonate substitution only increased up to skeletal maturity in the femora of baboons. Acid phosphate substitution, in contrast to the changes in carbonate substitution with animal aging, remained constant between young and adult mice and decreased significantly between adult and elderly mice. Acid phosphate content was shown to correlate with new mineral deposition [100, 101], but only recently validated as a FTIRI parameter in a study which showed that acid phosphate content decreased in mice between 0 and 6 months old [99]. Crystallinity, which reflects both mineral perfection and size, decreased between young and adult mice, but increased between adult and elderly mice. These changes could be associated with the same trends of change observed for the carbonate:mineral ratio between ages, since carbonate substitution in mineral is not stoichiometric and consequently disrupts the lattice spacing and the mineral uniformity [93, 94]. Even if a similar relationship to the one suggested by the data of this study, between carbonate substitution and mineral crystallinity was previously reported [81], the relation between the two parameters hasn't been yet clearly described. In addition, the changes detected in this study in the absolute values of crystallinity were very small: between 1.11 and 1.19 in control limbs and between 1.12 and 1.20 in loaded limbs. The thickness of the mineral particles (T parameter) in young, adult and elderly mice was also studied. Merging all the points measured within the intracortical region of the two mice studied per each age (approximately 12000 points), revealed that there is a shift towards thicker mineral particles (T>2.5 nm) in the tibia of elderly mice. However, analyzing the mean T parameter for each

individual mouse showed that there was no pronounced age-related change in the mean thickness of the mineral particles. This finding is supported by other sSAXS studies, which showed that the mean mineral thickness increases only up to 2 to 3 months in mice femora and tibiae [111] and that it remains substantially the same throughout life in human femora [106] and in human vertebrae (only subtle increases after 4 years old) [38]. For the degree of mineral alignment, no specific pattern of variation with age was detected. This result is consistent with studies that reported no change in the ρ parameter with increasing age in mice [111] and in the degree of preferred mineral orientation after the first decade of life in the human femora [106]. The obtained results suggest that the changes in mineral degree of alignment occur mainly during early stages of skeletal growth and not afterwards. No changes were detected in collagen maturity (mature/immature cross-links) between post-pubescent, adult and elderly mice, which is in agreement with previous FTIRI studies [81, 96, 130]. It is likely that most of the changes in collagen maturity occur before puberty. In human bone, it was also shown that immature and mature cross-links remain approximately constant in adult age, with immature cross-links decreasing only up to 25 years old and mature cross-links reaching a maximum at 10-15 years old [331].
Additionally, the mineral and matrix properties at the endocortical and periosteal regions at the tibial midshaft of control limbs of young, adult and elderly mice were assessed. Although some differences were registered in the properties of the tissue in the endocortical and periosteal regions between ages, these differences mostly never reached significance. These results might indicate that the newly formed bone by young, adult and elderly mice has similar material quality.

5.6 The effect of tissue age on cortical bone mineral and matrix properties during normal physiological loading

Since the effects of animal age and tissue age on bone mineral and matrix properties are often intermixed in the literature, the effects of each were evaluated separately, in this work. Tissue age-related changes were assessed by comparing young tissue at the endocortical and periosteal regions with older tissue at the intracortical region of the control tibial midshaft.

As with animal age, tissue age was shown to have a significant effect on the mineral and matrix properties studied with FTIRI. Similar to previous studies, lower mineral:matrix ratio [83, 84, 90-92] and crystallinity [83, 91, 92, 104] was detected in younger tissue at the periosteal and endocortical regions, when compared with older intracortical tissue across all animal ages. These results are not surprising, as it is known that newly laid bone is less mineralized than older bone. In addition, tissue at the endocortical and periosteal regions had higher acid phosphate content than tissue at the intracortical region in young, adult and elderly mice. High acid phosphate content has been associated with areas of new bone formation [99-101] and it has even been recently suggested as a reliable indicator of the most recent site of bone deposition [99]. Different studies showed that collagen maturity increased with tissue age [83, 84, 131], but also that it reached a maximum early during tissue maturation [83, 91, 122]. The results obtained in the current study reflect these findings, as it was shown that collagen

maturity was significantly or marginally significantly lower in the endocortical and periosteal regions, when compared to the intracortical region of the control limbs of 10 week old mice, the mice with the highest amount of newly formed tissue. The parameter carbonate:mineral ratio has been reported both to increase [84, 90, 131] and to decrease [85, 97] with tissue aging. In the current study, the only tissue age-related significant difference detected for this parameter was an increase in carbonate:mineral ratio in young animals and a decrease in elderly animals between the periosteal and the intracortical regions. The standard deviations of the carbonate:mineral ratio in the endocortical and periosteal regions were relatively high, which make the results difficult to interpret. It was also seen that the mean mineral thickness and degree of alignment tended to be lower in the newly formed tissue at the endocortical region, but not at the periosteal region, when compared to older tissue in the intracortical region. These results relate to the previously discussed finding of thinner and less aligned mineral particles of the new tissue at the endocortical region, when compared to the new tissue at the periosteal region of the loaded tibiae. In addition, the variation of T and ρ parameters with tissue age was shown by other groups, when comparing younger with older bone tissue in human osteons [113], in trabeculae [332] and in the cortical bone diaphysis of rat femora [112].

Assessing age-related (both animal age and tissue age) changes in bone nano and microscopic mineral and matrix properties broadens our understanding on bone development and also on the causes and/or effects of the increased bone fragility associated with advanced aging. In addition, only by having a well characterized control physiologically loaded bone was it possible to determine whether extra *in vivo* mechanical loading induced positive changes in bone quantity and quality or helped prevent its deterioration.

5.7 Relationship between mineral properties and calcein labeling in mineralizing bone surfaces and mineral in the vicinity of blood vessels

Unexpected findings emerged from this work concerning the use of fluorochrome labels on bone mineral. In addition, specific mineral patterns were detected around blood vessels in the bone. Both of these findings were possible due to the high-resolution techniques used in the study of the bone material.

Bone mineral was characterized at the region where the calcein fluorochrome labels were located by merging high resolution T and ρ parameter maps (1 μm spacing between measured points) of the tibial midshaft with the respective fluorescence images. The results obtained showed lower mean mineral thickness and degree of mineral particle alignment at the calcein fluorochrome labels location. Fluorochrome labeling is routinely used for decades for quantitative measurement of bone formation and bone remodeling dynamics. Newly formed bone tissue can be identified, as the fluorochrome labels (calcium-seeking substances) selectively bind to sites of new mineralized tissue formation and are incorporated into the mineralization front. However, it remains unclear why the selective binding occurs, although some studies suggest that this is due to the smaller crystal size formed in the initial phase of

mineralization, in comparison with older mineralizing sites [333]. A study in rats labeled with different fluorochromes also showed, using sSAXS, a decrease in the degree of mineral alignment, but not in the mineral thickness on the border between old and new bone [112], which seemed to coincide with the label itself. However, an *in vitro* study demonstrated that there is direct relationship between bone-like carbonated apatite crystal size and growth kinetics and the concentration of the fluorochrome label alizarin red [334]. The authors showed that alizarin red stabilized the detected amorphous precursor phase and therefore led to an exponential increase in the nucleation time of apatite. The results obtained in this study indicate that the calcein might not only bind to mineralizing surfaces, but also interfere with mineral growth, possibly in a similar manner as non-collageneous proteins by stunting their growth. The BSE images of the studied tibial samples did not show different mineral content at the calcein label sites, but this should rather be assessed with quantitative methods, such as quantitative backscattered electron imaging (qBEI) [25].

The regions surrounding blood vessels of young, adult and elderly mice were also characterized by a distinct mineral pattern. Thinner and less aligned mineral particles were found near all the analyzed blood vessels, when compared with the surrounding tissue. In contrast to the findings at the calcein label location, the presence of thinner and less aligned mineral particles near the blood vessels was likely related to the age of this tissue rather than alterations in crystal growth. As observed also in the BSE images, which showed lower mineral content in the regions surrounding blood vessels, the bone tissue surrounding blood vessels was younger.

5.8 Limitations of the study

The current work was not without limitations. The sSAXS data was limited by the sample size of 6 tibiae (n = 2 mice/age). These measurements were performed during a 96 hour session at the ESRF, a facility where usage is very restricted. However, it was possible to measure each sample with extremely high resolution, registering scattering patterns with 1 μm spacing between each other. Another limitation of this work was that the endocortical and periosteal regions analyzed with FTIRI did not always strictly correspond to bone tissue located between calcein labels. Nevertheless, the chosen endocortical and periosteal regions of interest included younger tissue with significantly lower mineral:matrix ratio, crystallinity and higher acid phosphate content than the intracortical mature tissue region. In addition, the differences between loaded and control limbs were generally much smaller than the differences between endocortical or periosteal and the intracortical region for each mouse, reinforcing the finding that *in vivo* loading did not affect the quality of the newly formed tissue. In addition, even though the influence of animal age and tissue age on bone mineral and matrix properties was separately analyzed, one shouldn't forget that the differences detected between young and older mice are not necessarily linked to a real animal aging effect. Young mice may be different from older mice because, due to fast growth, even their "old" bone is comparatively younger than "old" bone in older mice.

6 Conclusions

This thesis aimed at determining the effect of mechanical loading as a function of age on cortical bone mass and geometry and material quality (mineral and collagen matrix properties). Furthermore, this thesis aimed at understanding how animal and tissue age influenced bone mass, geometry, and material quality. For that, cortical bone in young, adult and elderly female C57BL/6J mice was examined after two weeks of controlled noninvasive *in vivo* tibial compressive loading and physiological loading. With microCT and dynamic histomorphometry, the effects of aging and loading on cortical bone mass and geometry were assessed, while the effects on bone's mineral and collagen were measured using high-resolution techniques such as synchrotron sSAXS and FTIRI. The effect of mechanical loading on the topology of the osteocyte LCN and perilacunar tissue (tissue surrounding the osteocyte lacuna) material properties, involved in mechanical sensation, were assessed with CLSM and nanoindentation, respectively.

The following conclusions were drawn:

- The effect of controlled *in vivo* loading on cortical bone varied with animal age. In young mice, and to a lesser extent in adult mice, loading enhanced the bone mass and geometry. In elderly mice, loading did not result in net bone gain, but still prevented a net bone loss. Interestingly, load-induced adaptive changes in the mineral and matrix properties were predominantly observed in elderly mice. Additional controlled loading led to enhanced collagen maturity and degree of mineralization in the elderly mice, which might correspond to a mechanism by which bone mechanical properties could be enhanced. These findings suggest that mechanical loading is a promising noninvasive treatment to enhance bone quality, as well as maintain bone mass in individuals suffering from age-related bone loss.

- The material quality of the new bone tissue formed with additional *in vivo* loading was similar to the quality of new bone tissue formed only with physiological loading. Although the rate of bone formation (assessed through histomorphometry) was increased by additional controlled *in vivo* loading, it was shown with synchrotron sSAXS and FTIRI, that the physical and chemical properties of the mineral particles, as well as collagen maturity of the new tissue were not altered by additional *in vivo* loading.

- The new bone tissue formed at the endocortical and periosteal regions was shown to be distinct. Interestingly, the newly formed tissue at the periosteal surface of the bone was composed of mineral particles with a higher degree of alignment and greater thickness than the newly formed tissue at the endocortical region. These results provide new clues on how deposition of new bone is potentially influenced by the different mechanical and biological environments, characteristic of the endocortical and periosteal regions.

- Mechanical loading seems to have a relevant impact on the topology of the osteocyte LCN of new bone tissue. Preliminary results showed that the newly formed tissue with additional *in vivo* loading had a denser and more highly branched osteocyte LCN than the new tissue formed only with physiological loading. A detailed and comprehensive network more efficient in the transport of ions and other substances might have been responsible for the fact that the new tissue formed with additional *in vivo* loading had similar quality to the tissue formed only with physiological loading, even if formed at a faster pace.

- Pilot studies indicated that perilacunar tissue and tissue further away in bone had distinct mechanical properties (nanoindentation performed with spatial resolution of 3 μm). Further measurements assessing submicron gradient material properties in the vicinity of osteocyte lacunae would provide more clues on the role of the perilacunar tissue in mechanosensation.

- Mineral and matrix properties were animal age and tissue age dependent during physiological loading. However, changes in bone mass and geometry with aging were more pronounced than changes in bone's mineral and matrix properties. The results obtained suggest that changes in the studied bone's mineral and matrix properties occur mainly during early stages of skeletal growth, as different parameters such as collagen maturity, mineral thickness and degree of alignment did not or, at least not pronouncedly, changed between post-pubescent, adult and elderly animals.

- Bone mineral properties were altered by fluorochrome labeling and dependent on the proximity to blood vessels. Regions labeled with calcein fluorochrome were shown to have lower mean mineral thickness and degree of mineral alignment, which suggests that fluorochrome labeling might stunt bone's mineral growth and thus affect bone mineral quality. In addition, thinner and less aligned particles were present near blood vessels, finding which was attributed to the presence of younger tissue.

Outlook

The work reported in this thesis generated some additional questions and possible directions of future research:

- The impact of mechanical loading on the degree of mineralization and collagen maturity at the tibial midshaft of elderly mice should be further investigated. In particular, high-performance liquid chromatography could be used to obtain more detailed information on the load-induced changes in the types and amounts of collagen cross-links in elderly mice. Understanding the significance of the changes occurring with loading would require assessing the load-induced changes at the whole bone and the tissue level mechanical properties of elderly mice, using for example four-point bending and nanoindentation, respectively. This would allow correlating load-induced changes in mechanical properties with the detected changes in the degree of mineralization and collagen maturity in the loaded limbs of elderly mice.

- A more detailed understanding of the impact of mechanical loading on the osteocyte LCN formation is needed. Initially, it would be important to extend the quantification of the osteocyte LCN to a higher number of regions in the tibial midshaft and a higher number of mice. In addition, it would be interesting to determine whether the additional strain imposed on bone with *in vivo* loading would also lead to a denser and more branched osteocyte LCN in adult and elderly mice, as observed in young mice. Extending the quantification of the osteocyte LCN to other parameters, such as the lacunae diameter or the canaliculi orientation with respect to the bone's long axis, would also provide more insights on the impact of mechanical loading on the osteocyte LCN formation. For example, it is not established whether with additional load, lacunae are more aligned in the principal loading direction or whether the increased mineral apposition rate causes rapid irregular embedding of osteocytes. Finally, correlating the topology of the osteocyte LCN with the imposed strains throughout the tibia—calculated using finite element models—would provide novel insights on whether and how the strain environment in bone impact the topology of the osteocyte LCN and consequently its capacity to efficiently transmit mechanical stimuli and transport ions and other substances.

- The fragility of bone is known to increase with advanced aging, as a result of changes in bone quantity and quality. In this work, bone was analyzed at different levels of its structural hierarchy in young, adult and elderly mice. Identifying, in addition, the changes in the topology of the osteocyte LCN would complement these results and broaden the understanding of the increased fragility of bone with advanced age. This could be achieved by comparing the topology of the osteocyte LCN at the intracortical region of the control limbs of young, adult and elderly mice and identify, for example, whether the LCN connectivity is decreased with aging, as some studies suggest.

- As mechanical loading can be used as a treatment strategy to prevent or combat age-related bone loss or/and fragility for longer time periods than two weeks, further studies with longer loading durations are required.

- The results obtained suggesting an interference of calcein with mineral growth, raise the question whether other fluorochrome labels which are clinically used, such as tetracycline would have similar impact on bone's mineral. It would be relevant to test this hypothesis and also to further explore the changes occurring in mineral at the fluorochrome label location with high-resolution techniques, such as qBEI.

References

1. Weiner S, Wagner HD. The material bone: Structure mechanical function relations. Annual Review of Materials Science. 1998;28:271-98.
2. Fratzl P, Weinkamer R. Nature's hierarchical materials. Progress in Materials Science. 2007;52:1263–334.
3. Currey JD. Bones: Structure and Mechanics. N.J.: Princeton University Press; 2006.
4. Boskey AL, Coleman R. Aging and bone. J Dent Res. 2010;89(12):1333-48.
5. Bouxsein ML. Bone quality: where do we go from here? Osteoporos Int. 2003;14 Suppl 5:S118-27.
6. Bouxsein M. Biomechanics of age-related fractures. In: Marcus R, Feldeman D, Dempster DW, Luckey M, Cauley JA, editors. Osteoporosis: Academic Press; 2013.
7. Seeman E, Delmas PD. Bone quality-the material and structural basis of bone strength and fragility. N Engl J Med. 2006;354(21):2250-61.
8. Forwood MR, Burr DB. Physical activity and bone mass: exercises in futility? Bone Miner. 1993;21(2):89-112.
9. Pearson OM, Lieberman DE. The aging of Wolff's "law": ontogeny and responses to mechanical loading in cortical bone. Am J Phys Anthropol. 2004;Suppl 39:63-99.
10. Bonewald LF. Osteocytes. In: Rosen CJ, Bouillon R, Compston JE, Rosen V, editors. Primer on the Metabolic Bone Diseases and Disorders of Mineral Metabolism: John Wiley & Sons, Inc.; 2013.
11. Kerschnitzki M, Kollmannsberger P, Burghammer M, Duda GN, Weinkamer R, Wagermaier W, et al. Architecture of the osteocyte network correlates with bone material quality. J Bone Miner Res. 2013;28(8):1837-45.
12. Bonivtch AR, Bonewald LF, Nicolella DP. Tissue strain amplification at the osteocyte lacuna: a microstructural finite element analysis. J Biomech. 2007;40(10):2199-206.
13. Gong JK, Arnold JS, Cohn SH. Composition of Trabecular and Cortical Bone. Anat Rec. 1964;149:325-31.
14. Termine JD, Robey PG. Bone matrix proteins and the mineralization process In: Rosen CJ, Bouillon R, Compston JE, Rosen V, editors. Primer on the Metabolic Bone Diseases and Disorders of Mineral Metabolism: John Wiley & Sons, Inc.; 2013.
15. Zimmermann EA, Schaible E, Bale H, Barth HD, Tang SY, Reichert P, et al. Age-related changes in the plasticity and toughness of human cortical bone at multiple length scales. Proc Natl Acad Sci U S A. 2011;108(35):14416-21.
16. Landis WJ, Hodgens KJ, Arena J, Song MJ, McEwen BF. Structural relations between collagen and mineral in bone as determined by high voltage electron microscopic tomography. Microsc Res Tech. 1996;33(2):192-202.
17. White SW, Hulmes DJ, Miller A, Timmins PA. Collagen-mineral axial relationship in calcified turkey leg tendon by X-ray and neutron diffraction. Nature. 1977;266(5601):421-5.
18. Hodge AJ, Petruska JA. Recent studies with the electron microscope on ordered aggregates of the tropocollagen molecule. In: Ramachandran GN, editor. Aspects of protein structure. New York: Academic Press; 1963.
19. http://bhgroup.lsa.umich.edu/research/collagen.
20. Landis WJ, Song MJ, Leith A, McEwen L, McEwen BF. Mineral and organic matrix interaction in normally calcifying tendon visualized in three dimensions by high-voltage electron microscopic tomography and graphic image reconstruction. J Struct Biol. 1993;110(1):39-54.
21. Nudelman F, Pieterse K, George A, Bomans PH, Friedrich H, Brylka LJ, et al. The role of collagen in bone apatite formation in the presence of hydroxyapatite nucleation inhibitors. Nat Mater. 2010;9(12):1004-9.
22. Landis WJ. Mineral characterization in calcifying tissues: atomic, molecular and macromolecular perspectives. Connect Tissue Res. 1996;34(4):239-46.

23. Hassenkam T, Fantner GE, Cutroni JA, Weaver JC, Morse DE, Hansma PK. High-resolution AFM imaging of intact and fractured trabecular bone. Bone. 2004;35(1):4-10.
24. Reznikov N, Shahar R, Weiner S. Bone hierarchical structure in three dimensions. Acta Biomater. 2014;10(9):3815-26.
25. Fratzl P, Gupta HS, Paschalis EP, Roschger P. Structure and mechanical quality of the collagen–mineral nano-composite in bone. J Mater Chem 2004;14:2115-23. http://dx.doi.org/10.1039/B402005G
26. Boyde A, Jones S. Aspects of anatomy and development of bone: The nm, μm and mm hierarchy. Advances in organ biology. 1198;5A:3-44.
27. McConnell D. The crystal structure of bone. Clinical orthopaedics. 1962;23:253-68.
28. Ou-Yang H, Paschalis EP, Mayo WE, Boskey AL, Mendelsohn R. Infrared microscopic imaging of bone: spatial distribution of CO3(2-). J Bone Miner Res. 2001;16(5):893-900.
29. Fantner GE, Hassenkam T, Kindt JH, Weaver JC, Birkedal H, Pechenik L, et al. Sacrificial bonds and hidden length dissipate energy as mineralized fibrils separate during bone fracture. Nat Mater. 2005;4(8):612-6.
30. Rubin MA, Rubin J, Jasiuk I. SEM and TEM study of the hierarchical structure of C57BL/6J and C3H/HeJ mice trabecular bone. Bone. 2004;35(1):11-20.
31. Weiner S, Arad T, Sabanay I, Traub W. Rotated plywood structure of primary lamellar bone in the rat: orientations of the collagen fibril arrays. Bone. 1997;20(6):509-14.
32. Weiner S, Traub W, Wagner HD. Lamellar bone: structure-function relations. J Struct Biol. 1999;126(3):241-55.
33. Marotti G. A new theory of bone lamellation. Calcif Tissue Int. 1993;53 Suppl 1:S47-55; discussion S6.
34. Marotti G, Zallone AZ. Changes in the vascular network during the formation of Haversian systems. Acta Anat (Basel). 1980;106(1):84-100.
35. Jaschouz D, Paris O, Roschger P, Hwang H-S, Fratzl P. Pole figure analysis of mineral nanoparticle orientation in individual trabecula of human vertebral bone. Journal of Applied Crystallography. 2003;36:494-8.
36. Tesch W, Vandenbos T, Roschgr P, Fratzl-Zelman N, Klaushofer K, Beertsen W, et al. Orientation of mineral crystallites and mineral density during skeletal development in mice deficient in tissue nonspecific alkaline phosphatase. J Bone Miner Res. 2003;18(1):117-25.
37. Rinnerthaler S, Roschger P, Jakob HF, Nader A, Klaushofer K, Fratzl P. Scanning small angle X-ray scattering analysis of human bone sections. Calcif Tissue Int. 1999;64(5):422-9.
38. Roschger P, Grabner BM, Rinnerthaler S, Tesch W, Kneissel M, Berzlanovich A, et al. Structural development of the mineralized tissue in the human L4 vertebral body. J Struct Biol. 2001;136(2):126-36.
39. Browne D. http://cnx.org/contents/e4e7ed87-dca1-4c48-be92-9eb45065b8f0@2/Skeletal_System_Module_4:__Bon: Skeletal System Module 4: Bone Structure. OpenStax CNX; Nov 16, 2013.
40. http://www.iofbonehealth.org/facts-and-statistics/frax-map.
41. Arnett T. Teaching slides. http://wwwbrsocorguk/gallery/: Bone Research Society.
42. Melton LJ, 3rd, Gabriel SE, Crowson CS, Tosteson AN, Johnell O, Kanis JA. Cost-equivalence of different osteoporotic fractures. Osteoporos Int. 2003;14(5):383-8.
43. Svedbom A, Hernlund E, Ivergard M, Compston J, Cooper C, Stenmark J, et al. Osteoporosis in the European Union: a compendium of country-specific reports. Arch Osteoporos. 2013;8(1-2):137.
44. Strom O, Borgstrom F, Kanis JA, Compston J, Cooper C, McCloskey EV, et al. Osteoporosis: burden, health care provision and opportunities in the EU: a report prepared in collaboration with the International Osteoporosis Foundation (IOF) and the European Federation of Pharmaceutical Industry Associations (EFPIA). Arch Osteoporos. 2011;6(1-2):59-155.

45. Riggs BL, Wahner HW, Seeman E, Offord KP, Dunn WL, Mazess RB, et al. Changes in bone mineral density of the proximal femur and spine with aging. Differences between the postmenopausal and senile osteoporosis syndromes. J Clin Invest. 1982;70(4):716-23.
46. Kanis JA. Assessment of fracture risk and its application to screening for postmenopausal osteoporosis: synopsis of a WHO report. WHO Study Group. Osteoporos Int. 1994;4(6):368-81.
47. NIH Consensus Development Panel on Osteoporosis Prevention, Diagnosis, and Therapy, March 7-29, 2000: highlights of the conference. South Med J. 2001;94(6):569-73.
48. Reid IR. Osteoporosis: Overview of Pathogenesis. In: Rosen CJ, Bouillon R, Compston JE, Rosen V, editors. Primer on the Metabolic Bone Diseases and Disorders of Mineral Metabolism: John Wiley & Sons, Inc.; 2013.
49. Marshall D, Johnell O, Wedel H. Meta-analysis of how well measures of bone mineral density predict occurrence of osteoporotic fractures. BMJ. 1996;312(7041):1254-9.
50. Cummings SR, Nevitt MC, Browner WS, Stone K, Fox KM, Ensrud KE, et al. Risk factors for hip fracture in white women. Study of Osteoporotic Fractures Research Group. N Engl J Med. 1995;332(12):767-73.
51. Schuit SC, van der Klift M, Weel AE, de Laet CE, Burger H, Seeman E, et al. Fracture incidence and association with bone mineral density in elderly men and women: the Rotterdam Study. Bone. 2004;34(1):195-202.
52. Hui SL, Slemenda CW, Johnston CC, Jr. Baseline measurement of bone mass predicts fracture in white women. Ann Intern Med. 1989;111(5):355-61.
53. Melton LJ, 3rd, Atkinson EJ, O'Fallon WM, Wahner HW, Riggs BL. Long-term fracture prediction by bone mineral assessed at different skeletal sites. J Bone Miner Res. 1993;8(10):1227-33.
54. Cummings SR, Black DM, Nevitt MC, Browner W, Cauley J, Ensrud K, et al. Bone density at various sites for prediction of hip fractures. The Lancet. 1993;341(8837):72-5.
55. Sornay-Rendu E, Munoz F, Garnero P, Duboeuf F, Delmas PD. Identification of osteopenic women at high risk of fracture: the OFELY study. J Bone Miner Res. 2005;20(10):1813-9.
56. Wainwright SA, Marshall LM, Ensrud KE, Cauley JA, Black DM, Hillier TA, et al. Hip fracture in women without osteoporosis. J Clin Endocrinol Metab. 2005;90(5):2787-93.
57. Donnelly E, Lane JM, Boskey AL. Research perspectives: The 2013 AAOS/ORS research symposium on Bone Quality and Fracture Prevention. J Orthop Res. 2014;32(7):855-64.
58. Delmas PD. Treatment of postmenopausal osteoporosis. Lancet. 2002;359(9322):2018-26.
59. Frolik CA, Black EC, Cain RL, Satterwhite JH, Brown-Augsburger PL, Sato M, et al. Anabolic and catabolic bone effects of human parathyroid hormone (1-34) are predicted by duration of hormone exposure. Bone. 2003;33(3):372-9.
60. Li X, Warmington KS, Niu QT, Asuncion FJ, Barrero M, Grisanti M, et al. Inhibition of sclerostin by monoclonal antibody increases bone formation, bone mass, and bone strength in aged male rats. J Bone Miner Res. 2010;25(12):2647-56.
61. Padhi D, Jang G, Stouch B, Fang L, Posvar E. Single-dose, placebo-controlled, randomized study of AMG 785, a sclerostin monoclonal antibody. J Bone Miner Res. 2011;26(1):19-26.
62. http://www.niams.nih.gov/Health_Info/Bone/Osteoporosis/.
63. Riggs BL, Wahner HW, Melton LJ, 3rd, Richelson LS, Judd HL, Offord KP. Rates of bone loss in the appendicular and axial skeletons of women. Evidence of substantial vertebral bone loss before menopause. J Clin Invest. 1986;77(5):1487-91.
64. Riggs BL, Melton LJ, Robb RA, Camp JJ, Atkinson EJ, McDaniel L, et al. A population-based assessment of rates of bone loss at multiple skeletal sites: evidence for

substantial trabecular bone loss in young adult women and men. J Bone Miner Res. 2008;23(2):205-14.
65. Gilsanz V, Gibbens DT, Carlson M, Boechat MI, Cann CE, Schiulz EE. Peak Trabecular Vertebral Density: A Comparison of Adolescent and Adult Females. Calcif Tissue Int 1988;43:260-2.
66. Parfitt AM. Skeletal Heterogeneity and the Purposes of Bone Remodelling: Implications for the Understanding of Osteoporosis. In: Marcus R, Feldeman D, Dempster DW, Luckey M, Cauley JA, editors. Osteoporosis: Academic Press; 2013.
67. Seeman E. Modeling and Remodeling: The cellular machinery responsible for the gain and loss of bone's material and structural strength. In: Bilezikian JP, Raisz LG, Martin TJ, editors. Principles of Bone Biology: Academic Press; 2008.
68. Ensrud KE, Palermo L, Black DM, Cauley J, Jergas M, Orwoll ES, et al. Hip and calcaneal bone loss increase with advancing age: longitudinal results from the study of osteoporotic fractures. J Bone Miner Res. 1995;10(11):1778-87.
69. Hannan MT, Felson DT, Dawson-Hughes B, Tucker KL, Cupples LA, Wilson PW, et al. Risk factors for longitudinal bone loss in elderly men and women: the Framingham Osteoporosis Study. J Bone Miner Res. 2000;15(4):710-20.
70. Jee WS. Integrated bone tissue physiology:anatomy and physiology. In: Cowin SC, editor. Bone mechanics handbook. New York: Informa Healthcare; 2009.
71. Garn SM, Rohmann CG, Wagner B. Bone loss as a general phenomenon in man. Fed Proc. 1967;26(6):1729-36.
72. Garn SM, Wagner B, Rohmann CG, Ascoli W. Further evidence for continuing bone expansion. Am J Phys Anthropol. 1968;28(2):219-21.
73. Frost HM. On the estrogen-bone relationship and postmenopausal bone loss: A new model. J Bone Miner Res. 1999;14(9):1473-7.
74. Weinstein RS, Hutson MS. Decreased trabecular width and increased trabecular spacing contribute to bone loss with aging. Bone. 1987;8(3):137-42.
75. Parfitt AM. Age-related structural changes in trabecular and cortical bone: cellular mechanisms and biomechanical consequences. Calcif Tissue Int. 1984;36 Suppl 1:S123-8.
76. Parfitt AM, Mathews CH, Villanueva AR, Kleerekoper M, Frame B, Rao DS. Relationships between surface, volume, and thickness of iliac trabecular bone in aging and in osteoporosis. Implications for the microanatomic and cellular mechanisms of bone loss. J Clin Invest. 1983;72(4):1396-409.
77. Gourion-Arsiquaud S, Faibish D, Myers E, Spevak L, Compston J, Hodsman A, et al. Use of FTIR spectroscopic imaging to identify parameters associated with fragility fracture. J Bone Miner Res. 2009;24(9):1565-71.
78. Currey JD, Brear K, Zioupos P. The effects of ageing and changes in mineral content in degrading the toughness of human femora. J Biomech. 1996;29(2):257-60.
79. Currey JD. Effects of differences in mineralization on the mechanical properties of bone. Philos Trans R Soc Lond B Biol Sci. 1984;304(1121):509-18.
80. Currey JD. How well are bones designed to resist fracture? J Bone Miner Res. 2003;18(4):591-8.
81. Miller LM, Little W, Schirmer A, Sheik F, Busa B, Judex S. Accretion of bone quantity and quality in the developing mouse skeleton. J Bone Miner Res. 2007;22(7):1037-45.
82. Tarnowski CP, Ignelzi MA, Jr., Morris MD. Mineralization of developing mouse calvaria as revealed by Raman microspectroscopy. J Bone Miner Res. 2002;17(6):1118-26.
83. Gourion-Arsiquaud S, Burket JC, Havill LM, DiCarlo E, Doty SB, Mendelsohn R, et al. Spatial variation in osteonal bone properties relative to tissue and animal age. J Bone Miner Res. 2009;24(7):1271-81.
84. Burket J, Gourion-Arsiquaud S, Havill LM, Baker SP, Boskey AL, van der Meulen MC. Microstructure and nanomechanical properties in osteons relate to tissue and animal age. J Biomech. 2011;44(2):277-84.

85. Akkus O, Adar F, Schaffler MB. Age-related changes in physicochemical properties of mineral crystals are related to impaired mechanical function of cortical bone. Bone. 2004;34(3):443-53.
86. Yerramshetty JS, Lind C, Akkus O. The compositional and physicochemical homogeneity of male femoral cortex increases after the sixth decade. Bone. 2006;39(6):1236-43.
87. Morris MD, Mandair GS. Raman assessment of bone quality. Clin Orthop Relat Res. 2011;469(8):2160-9.
88. Jowsey J. Studies of Haversian systems in man and some animals. J Anat. 1966;100(Pt 4):857-64.
89. Barer M, Jowsey J. Bone formation and resorption in normal human rib. A study of persons from 11 to 88 years of age. Clin Orthop Relat Res. 1967;52:241-7.
90. Donnelly E, Boskey AL, Baker SP, van der Meulen MC. Effects of tissue age on bone tissue material composition and nanomechanical properties in the rat cortex. J Biomed Mater Res A. 2010;92(3):1048-56.
91. Busa B, Miller LM, Rubin CT, Qin YX, Judex S. Rapid establishment of chemical and mechanical properties during lamellar bone formation. Calcif Tissue Int. 2005;77(6):386-94.
92. Paschalis EP, DiCarlo E, Betts F, Sherman P, Mendelsohn R, Boskey AL. FTIR microspectroscopic analysis of human osteonal bone. Calcif Tissue Int. 1996;59(6):480-7.
93. Penel G, Leroy G, Rey C, Bres E. MicroRaman spectral study of the PO4 and CO3 vibrational modes in synthetic and biological apatites. Calcif Tissue Int. 1998;63(6):475-81.
94. Baig AA, Fox JL, Young RA, Wang Z, Hsu J, Higuchi WI, et al. Relationships among carbonated apatite solubility, crystallite size, and microstrain parameters. Calcif Tissue Int. 1999;64(5):437-49.
95. Hanschin RG, Stern WB. X-ray diffraction studies on the lattice perfection of human bone apatite (Crista iliaca). Bone. 1995;16(4 Suppl):355S-63S.
96. Raghavan M, Sahar ND, Kohn DH, Morris MD. Age-specific profiles of tissue-level composition and mechanical properties in murine cortical bone. Bone. 2012;50(4):942-53.
97. Turunen MJ, Prantner V, Jurvelin JS, Kroger H, Isaksson H. Composition and microarchitecture of human trabecular bone change with age and differ between anatomical locations. Bone. 2013;54(1):118-25.
98. Glimcher MJ. The nature of the mineral phase in bone. In: Avioli LV, Krane SM, editors. Metabolic Bone Diseases and Related Disorders. San Diego: Academic Press; 1998.
99. Spevak L, Flach CR, Hunter T, Mendelsohn R, Boskey A. Fourier transform infrared spectroscopic imaging parameters describing acid phosphate substitution in biologic hydroxyapatite. Calcif Tissue Int. 2013;92(5):418-28.
100. Miller LM, Vairavamurthy V, Chance MR, Mendelsohn R, Paschalis EP, Betts F, et al. In situ analysis of mineral content and crystallinity in bone using infrared micro-spectroscopy of the nu(4) PO(4)(3-) vibration. Biochim Biophys Acta. 2001;1527(1-2):11-9.
101. Roberts JE, Bonar LC, Griffin RG, Glimcher MJ. Characterization of very young mineral phases of bone by solid state 31phosphorus magic angle sample spinning nuclear magnetic resonance and X-ray diffraction. Calcif Tissue Int. 1992;50(1):42-8.
102. Jager I, Fratzl P. Mineralized collagen fibrils: a mechanical model with a staggered arrangement of mineral particles. Biophys J. 2000;79(4):1737-46.
103. Bokskey A. Bone mineral crystal size. Osteoporos Int 2003;14(Suppl 5):S16-20.
104. Paschalis EP, Betts F, DiCarlo E, Mendelsohn R, Boskey AL. FTIR microspectroscopic analysis of normal human cortical and trabecular bone. Calcif Tissue Int. 1997;61(6):480-6.

105. Simmons ED, Jr., Pritzker KP, Grynpas MD. Age-related changes in the human femoral cortex. J Orthop Res. 1991;9(2):155-67.
106. Chatterji S, Wall JC, Jeffery JW. Age-related changes in the orientation and particle size of the mineral phase in human femoral cortical bone. Calcif Tissue Int. 1981;33(6):567-74.
107. Tesch W, Eidelman N, Roschger P, Goldenberg F, Klaushofer K, Fratzl P. Graded microstructure and mechanical properties of human crown dentin. Calcif Tissue Int. 2001;69(3):147-57.
108. Lange C, Li C, Manjubala I, Wagermaier W, Kuhnisch J, Kolanczyk M, et al. Fetal and postnatal mouse bone tissue contains more calcium than is present in hydroxyapatite. J Struct Biol. 2011;176(2):159-67.
109. Fratzl P, Schreiber S, Klaushofer K. Bone mineralization as studied by small-angle x-ray scattering. Connect Tissue Res. 1996;34(4):247-54.
110. Fratzl P, Fratzl-Zelman N, Klaushofer K, Vogl G, Koller K. Nucleation and growth of mineral crystals in bone studied by small-angle X-ray scattering. Calcif Tissue Int. 1991;48(6):407-13.
111. Grabner B, Landis WJ, Roschger P, Rinnerthaler S, Peterlik H, Klaushofer K, et al. Age- and genotype-dependence of bone material properties in the osteogenesis imperfecta murine model (oim). Bone. 2001;29(5):453-7.
112. Bunger MH, Oxlund H, Hansen TK, Sorensen S, Bibby BM, Thomsen JS, et al. Strontium and bone nanostructure in normal and ovariectomized rats investigated by scanning small-angle X-ray scattering. Calcif Tissue Int. 2010;86(4):294-306.
113. Granke M, Gourrier A, Rupin F, Raum K, Peyrin F, Burghammer M, et al. Microfibril orientation dominates the microelastic properties of human bone tissue at the lamellar length scale. PLoS One. 2013;8(3):e58043.
114. Chatterji S, Wall JC, Jeffrey JW. Changes in the degree of orientation of bone materials with age in the human femur. Experientia. 1972;28(2):156-7.
115. Li C, Paris O, Siegel S, Roschger P, Paschalis EP, Klaushofer K, et al. Strontium is incorporated into mineral crystals only in newly formed bone during strontium ranelate treatment. J Bone Miner Res. 2010;25(5):968-75.
116. Burr DB. The contribution of the organic matrix to bone's material properties. Bone. 2002;31(1):8-11.
117. Wang X, Bank RA, TeKoppele JM, Agrawal CM. The role of collagen in determining bone mechanical properties. J Orthop Res. 2001;19(6):1021-6.
118. Boivin G, Bala Y, Doublier A, Farlay D, Ste-Marie LG, Meunier PJ, et al. The role of mineralization and organic matrix in the microhardness of bone tissue from controls and osteoporotic patients. Bone. 2008;43(3):532-8.
119. Zioupos P, Currey JD, Hamer AJ. The role of collagen in the declining mechanical properties of aging human cortical bone. J Biomed Mater Res. 1999;45(2):108-16.
120. Knott L, Whitehead CC, Fleming RH, Bailey AJ. Biochemical changes in the collagenous matrix of osteoporotic avian bone. Biochem J. 1995;310 (Pt 3):1045-51.
121. Kowitz J, Knippel M, Schuhr T, Mach J. Alteration in the extent of collagen I hydroxylation, isolated from femoral heads of women with a femoral neck fracture caused by osteoporosis. Calcif Tissue Int. 1997;60(6):501-5.
122. Saito M, Marumo K. Collagen cross-links as a determinant of bone quality: a possible explanation for bone fragility in aging, osteoporosis, and diabetes mellitus. Osteoporos Int. 2010;21(2):195-214.
123. Campagnola PJ, Loew LM. Second-harmonic imaging microscopy for visualizing biomolecular arrays in cells, tissues and organisms. Nat Biotechnol. 2003;21(11):1356-60.
124. Nyman JS, Roy A, Acuna RL, Gayle HJ, Reyes MJ, Tyler JH, et al. Age-related effect on the concentration of collagen crosslinks in human osteonal and interstitial bone tissue. Bone. 2006;39(6):1210-7.

125. Tang SY, Zeenath U, Vashishth D. Effects of non-enzymatic glycation on cancellous bone fragility. Bone. 2007;40(4):1144-51.
126. Viguet-Carrin S, Follet H, Gineyts E, Roux JP, Munoz F, Chapurlat R, et al. Association between collagen cross-links and trabecular microarchitecture properties of human vertebral bone. Bone. 2010;46(2):342-7.
127. Garnero P, Borel O, Gineyts E, Duboeuf F, Solberg H, Bouxsein ML, et al. Extracellular post-translational modifications of collagen are major determinants of biomechanical properties of fetal bovine cortical bone. Bone. 2006;38(3):300-9.
128. Saito M, Fujii K, Mori Y, Marumo K. Role of collagen enzymatic and glycation induced cross-links as a determinant of bone quality in spontaneously diabetic WBN/Kob rats. Osteoporos Int. 2006;17(10):1514-23.
129. Paschalis EP, Verdelis K, Doty SB, Boskey AL, Mendelsohn R, Yamauchi M. Spectroscopic characterization of collagen cross-links in bone. J Bone Miner Res. 2001;16(10):1821-8.
130. Kobrina Y, Turunen MJ, Saarakkala S, Jurvelin JS, Hauta-Kasari M, Isaksson H. Cluster analysis of infrared spectra of rabbit cortical bone samples during maturation and growth. Analyst. 2010;135(12):3147-55.
131. Boskey A, Pleshko Camacho N. FT-IR imaging of native and tissue-engineered bone and cartilage. Biomaterials. 2007;28(15):2465-78.
132. Paschalis EP, Recker R, DiCarlo E, Doty SB, Atti E, Boskey AL. Distribution of collagen cross-links in normal human trabecular bone. J Bone Miner Res. 2003;18(11):1942-6.
133. Chalmers J, Ray RD. The growth of transplanted foetal bones in different immunological environments. Journal of Bone and Joint Surgery 1962;44:149–64.
134. Wolff J. Das Gesetz der Transformation der Knochen. Berlin: Hischwald; 1892.
135. Roux W. Der Kampf der Teile im Organismus. Saarbrucken: VDM Verlag Publishing; 1881.
136. Frost HM. Bone "mass" and the "mechanostat": a proposal. Anat Rec. 1987;219(1):1-9.
137. Frost HM. Bone's mechanostat: a 2003 update. Anat Rec A Discov Mol Cell Evol Biol. 2003;275(2):1081-101.
138. Lanyon LE, Sugiyama T, Price JS. Regulation of bone mass: Local control or systemic influence or both? IBMS BoneKEy. 2009;6(6):218-26. http://dx.doi.org/10.1138/20090382
139. Nishimura Y, Fukuoka H, Kiriyama M, Suzuki Y, Oyama K, Ikawa S, et al. Bone turnover and calcium metabolism during 20 days bed rest in young healthy males and females. Acta Physiol Scand Suppl. 1994;616:27-35.
140. Caillot-Augusseau A, Lafage-Proust MH, Soler C, Pernod J, Dubois F, Alexandre C. Bone formation and resorption biological markers in cosmonauts during and after a 180-day space flight (Euromir 95). Clin Chem. 1998;44(3):578-85.
141. Collet P, Uebelhart D, Vico L, Moro L, Hartmann D, Roth M, et al. Effects of 1- and 6-month spaceflight on bone mass and biochemistry in two humans. Bone. 1997;20(6):547-51.
142. Spengler DM, Morey ER, Carter DR, Turner RT, Baylink DJ. Effect of space flight on bone strength. Physiologist. 1979;22(6):S75-6.
143. Jones HH, Priest JD, Hayes WC, Tichenor CC, Nagel DA. Humeral hypertrophy in response to exercise. J Bone Joint Surg Am. 1977;59(2):204-8.
144. Haapasalo H, Kontulainen S, Sievanen H, Kannus P, Jarvinen M, Vuori I. Exercise-induced bone gain is due to enlargement in bone size without a change in volumetric bone density: a peripheral quantitative computed tomography study of the upper arms of male tennis players. Bone. 2000;27(3):351-7.
145. Kontulainen S, Sievanen H, Kannus P, Pasanen M, Vuori I. Effect of long-term impact-loading on mass, size, and estimated strength of humerus and radius of female racquet-sports players: a peripheral quantitative computed tomography study between young and old starters and controls. J Bone Miner Res. 2003;18(2):352-9.

146. van Marken Lichtenbelt WD, Fogelholm M, Ottenheijm R, Westerterp KR. Physical activity, body composition and bone density in ballet dancers. Br J Nutr. 1995;74(4):439-51.
147. Dalen N, Olsson KE. Bone mineral content and physical activity. Acta Orthop Scand. 1974;45(2):170-4.
148. Wittich A, Mautalen CA, Oliveri MB, Bagur A, Somoza F, Rotemberg E. Professional football (soccer) players have a markedly greater skeletal mineral content, density and size than age- and BMI-matched controls. Calcif Tissue Int. 1998;63(2):112-7.
149. Fehling PC, Alekel L, Clasey J, Rector A, Stillman RJ. A comparison of bone mineral densities among female athletes in impact loading and active loading sports. Bone. 1995;17(3):205-10.
150. Heinonen A, Oja P, Kannus P, Sievanen H, Haapasalo H, Manttari A, et al. Bone mineral density in female athletes representing sports with different loading characteristics of the skeleton. Bone. 1995;17(3):197-203.
151. Taaffe DR, Snow-Harter C, Connolly DA, Robinson TL, Brown MD, Marcus R. Differential effects of swimming versus weight-bearing activity on bone mineral status of eumenorrheic athletes. J Bone Miner Res. 1995;10(4):586-93.
152. Robling AG, Burr DB, Turner CH. Skeletal loading in animals. J Musculoskelet Neuronal Interact. 2001;1(3):249-62.
153. Mosekilde L, Danielsen CC, Sogaard CH, Thorling E. The effect of long-term exercise on vertebral and femoral bone mass, dimensions, and strength-assessed in a rat model. Bone. 1994;15(3):293-301.
154. Umemura Y, Ishiko T, Yamauchi T, Kurono M, Mashiko S. Five jumps per day increase bone mass and breaking force in rats. J Bone Miner Res. 1997;12(9):1480-5.
155. Lanyon LE, Goodship AE, Pye CJ, MacFie JH. Mechanically adaptive bone remodelling. J Biomech. 1982;15(3):141-54.
156. Goodship AE, Lanyon LE, McFie H. Functional adaptation of bone to increased stress. An experimental study. J Bone Joint Surg Am. 1979;61(4):539-46.
157. Takano Y, Turner CH, Owan I, Martin RB, Lau ST, Forwood MR, et al. Elastic anisotropy and collagen orientation of osteonal bone are dependent on the mechanical strain distribution. J Orthop Res. 1999;17(1):59-66.
158. Liskova M, Hert J. Reaction of bone to mechanical stimuli. 2. Periosteal and endosteal reaction of tibial diaphysis in rabbit to intermittent loading. Folia Morphol (Praha). 1971;19(3):301-17.
159. Lanyon LE, Rubin CT. Static vs dynamic loads as an influence on bone remodelling. J Biomech. 1984;17(12):897-905.
160. Chambers TJ, Evans M, Gardner TN, Turner-Smith A, Chow JW. Induction of bone formation in rat tail vertebrae by mechanical loading. Bone Miner. 1993;20(2):167-78.
161. Lambers FM, Schulte FA, Kuhn G, Webster DJ, Muller R. Mouse tail vertebrae adapt to cyclic mechanical loading by increasing bone formation rate and decreasing bone resorption rate as shown by time-lapsed in vivo imaging of dynamic bone morphometry. Bone. 2011;49(6):1340-50.
162. Webster D, Wasserman E, Ehrbar M, Weber F, Bab I, Muller R. Mechanical loading of mouse caudal vertebrae increases trabecular and cortical bone mass-dependence on dose and genotype. Biomech Model Mechanobiol. 2010;9(6):737-47.
163. Torrance AG, Mosley JR, Suswillo RF, Lanyon LE. Noninvasive loading of the rat ulna in vivo induces a strain-related modeling response uncomplicated by trauma or periostal pressure. Calcif Tissue Int. 1994;54(3):241-7.
164. Turner CH, Akhter MP, Raab DM, Kimmel DB, Recker RR. A noninvasive, in vivo model for studying strain adaptive bone modeling. Bone. 1991;12(2):73-9.
165. Akhter MP, Cullen DM, Pedersen EA, Kimmel DB, Recker RR. Bone response to in vivo mechanical loading in two breeds of mice. Calcif Tissue Int. 1998;63(5):442-9.

166. Lee KC, Maxwell A, Lanyon LE. Validation of a technique for studying functional adaptation of the mouse ulna in response to mechanical loading. Bone. 2002;31(3):407-12.
167. Mosley JR, March BM, Lynch J, Lanyon LE. Strain magnitude related changes in whole bone architecture in growing rats. Bone. 1997;20(3):191-8.
168. Mosley JR, Lanyon LE. Strain rate as a controlling influence on adaptive modeling in response to dynamic loading of the ulna in growing male rats. Bone. 1998;23(4):313-8.
169. Turner CH, Owan I, Takano Y. Mechanotransduction in bone: role of strain rate. Am J Physiol. 1995;269(3 Pt 1):E438-42.
170. Rubin CT, Lanyon LE. Regulation of bone formation by applied dynamic loads. J Bone Joint Surg Am. 1984;66(3):397-402.
171. Robling AG, Burr DB, Turner CH. Partitioning a daily mechanical stimulus into discrete loading bouts improves the osteogenic response to loading. J Bone Miner Res. 2000;15(8):1596-602.
172. Srinivasan S, Gross TS. Intermittent rest enhances osteoblastic activation induced by mechanical loading. Trans Orthop Res Soc. 2000;25:628.
173. Robling AG, Burr DB, Turner CH. Recovery periods restore mechanosensitivity to dynamically loaded bone. J Exp Biol. 2001;204(Pt 19):3389-99. http://jeb.biologists.org/content/204/19/3389.full
174. Chen NX, Ryder KD, Pavalko FM, Turner CH, Burr DB, Qiu J, et al. Ca(2+) regulates fluid shear-induced cytoskeletal reorganization and gene expression in osteoblasts. Am J Physiol Cell Physiol. 2000;278(5):C989-97.
175. Fritton JC, Myers ER, Wright TM, van der Meulen MC. Loading induces site-specific increases in mineral content assessed by microcomputed tomography of the mouse tibia. Bone. 2005;36(6):1030-8.
176. De Souza RL, Matsuura M, Eckstein F, Rawlinson SC, Lanyon LE, Pitsillides AA. Non-invasive axial loading of mouse tibiae increases cortical bone formation and modifies trabecular organization: a new model to study cortical and cancellous compartments in a single loaded element. Bone. 2005;37(6):810-8.
177. Lynch ME, Main RP, Xu Q, Walsh DJ, Schaffler MB, Wright TM, et al. Cancellous bone adaptation to tibial compression is not sex dependent in growing mice. J Appl Physiol (1985). 2010;109(3):685-91.
178. Sugiyama T, Saxon LK, Zaman G, Moustafa A, Sunters A, Price JS, et al. Mechanical loading enhances the anabolic effects of intermittent parathyroid hormone (1-34) on trabecular and cortical bone in mice. Bone. 2008;43(2):238-48.
179. Sugiyama T, Meakin LB, Browne WJ, Galea GL, Price JS, Lanyon LE. Bones' adaptive response to mechanical loading is essentially linear between the low strains associated with disuse and the high strains associated with the lamellar/woven bone transition. J Bone Miner Res. 2012;27(8):1784-93.
180. Patel TK, Brodt MD, Silva MJ. Experimental and finite element analysis of strains induced by axial tibial compression in young-adult and old female C57Bl/6 mice. J Biomech. 2014;47(2):451-7.
181. Willie BM, Weinkamer R, Duda GN. Bone structural's adaptation and Wolff's Law. In: Fratzl P, Weinkamer R, Dunlop JW, editors. Materials Design Inspired by Nature: Function Through Inner Architecture: Cambridge: RSC; 2013. http://dx.doi.org/10.1039/9781849737555
182. Bonewald LF. Osteocyte Biology. In: Marcus R, Feldman D, Dempster DW, Luckey M, Cauley JA, editors. Osteoporosis: Academic Press; 2013.
183. Marroti G. The original contributions of the scanning electron microscope to the knowledge of bone structure, Bone and Cartilage in Health and Disease. In: Bonucci E, Motta PM, editors. Ultrastructure of Skeletal Tissues 7: Springer US; 1990. p. 19-39.
184. Lanyon LE. Osteocytes, strain detection, bone modeling and remodeling. Calcif Tissue Int. 1993;53 Suppl 1:S102-6; discussion S6-7.

185. Vatsa A, Breuls RG, Semeins CM, Salmon PL, Smit TH, Klein-Nulend J. Osteocyte morphology in fibula and calvaria --- is there a role for mechanosensing? Bone. 2008;43(3):452-8.
186. Hirose S, Li M, Kojima T, de Freitas PH, Ubaidus S, Oda K, et al. A histological assessment on the distribution of the osteocytic lacunar canalicular system using silver staining. J Bone Miner Metab. 2007;25(6):374-82.
187. Dallas SL, Prideaux M, Bonewald LF. The osteocyte: an endocrine cell ... and more. Endocr Rev. 2013;34(5):658-90.
188. Skerry TM, Bitensky L, Chayen J, Lanyon LE. Early strain-related changes in enzyme activity in osteocytes following bone loading in vivo. J Bone Miner Res. 1989;4(5):783-8.
189. Dodds RA, Ali N, Pead MJ, Lanyon LE. Early loading-related changes in the activity of glucose 6-phosphate dehydrogenase and alkaline phosphatase in osteocytes and periosteal osteoblasts in rat fibulae in vivo. J Bone Miner Res. 1993;8(3):261-7.
190. Tatsumi S, Ishii K, Amizuka N, Li M, Kobayashi T, Kohno K, et al. Targeted ablation of osteocytes induces osteoporosis with defective mechanotransduction. Cell Metab. 2007;5(6):464-75.
191. Cowin SC, Moss-Salentijn L, Moss ML. Candidates for the mechanosensory system in bone. J Biomech Eng. 1991;113(2):191-7.
192. Knothe Tate ML. "Whither flows the fluid in bone?" An osteocyte's perspective. J Biomech. 2003;36(10):1409-24.
193. Weinbaum S, Cowin SC, Zeng Y. A model for the excitation of osteocytes by mechanical loading-induced bone fluid shear stresses. J Biomech. 1994;27(3):339-60.
194. Verbruggen SW, Vaughan TJ, McNamara LM. Fluid flow in the osteocyte mechanical environment: a fluid-structure interaction approach. Biomech Model Mechanobiol. 2014;13(1):85-97.
195. You L, Cowin SC, Schaffler MB, Weinbaum S. A model for strain amplification in the actin cytoskeleton of osteocytes due to fluid drag on pericellular matrix. J Biomech. 2001;34(11):1375-86.
196. Wang Y, McNamara LM, Schaffler MB, Weinbaum S. A model for the role of integrins in flow induced mechanotransduction in osteocytes. Proc Natl Acad Sci U S A. 2007;104(40):15941-6.
197. Han Y, Cowin SC, Schaffler MB, Weinbaum S. Mechanotransduction and strain amplification in osteocyte cell processes. Proc Natl Acad Sci U S A. 2004;101(47):16689-94.
198. Owan I, Burr DB, Turner CH, Qiu J, Tu Y, Onyia JE, et al. Mechanotransduction in bone: osteoblasts are more responsive to fluid forces than mechanical strain. Am J Physiol. 1997;273(3 Pt 1):C810-5.
199. Burr DB, Milgrom C, Fyhrie D, Forwood M, Nyska M, Finestone A, et al. In vivo measurement of human tibial strains during vigorous activity. Bone. 1996;18(5):405-10.
200. Yang PF, Bruggemann GP, Rittweger J. What do we currently know from in vivo bone strain measurements in humans? J Musculoskelet Neuronal Interact. 2011;11(1):8-20.
201. Smalt R, Mitchell FT, Howard RL, Chambers TJ. Induction of NO and prostaglandin E2 in osteoblasts by wall-shear stress but not mechanical strain. Am J Physiol. 1997;273(4 Pt 1):E751-8.
202. Nicolella DP, Moravits DE, Gale AM, Bonewald LF, Lankford J. Osteocyte lacunae tissue strain in cortical bone. J Biomech. 2006;39(9):1735-43.
203. Varga P, Hesse B, Langer M, Schrof S, Mannicke N, Suhonen H, et al. Synchrotron X-ray phase nano-tomography-based analysis of the lacunar-canalicular network morphology and its relation to the strains experienced by osteocytes in situ as predicted by case-specific finite element analysis. Biomech Model Mechanobiol. 2014.
204. Santos A, Bakker AD, Klein-Nulend J. The role of osteocytes in bone mechanotransduction. Osteoporos Int. 2009;20(6):1027-31.

205. Dooley C, Tisbo P, Lee TC, Taylor D. Rupture of osteocyte processes across microcracks: the effect of crack length and stress. Biomech Model Mechanobiol. 2012;11(6):759-66.
206. Qiu S, Rao DS, Fyhrie DP, Palnitkar S, Parfitt AM. The morphological association between microcracks and osteocyte lacunae in human cortical bone. Bone. 2005;37(1):10-5.
207. Gu G, Kurata K, Chen Z, Vaananen K. Osteocyte: a cellular basis for mechanotransduction in bone. J Biomechanical Science and Eng. 2007;2(4):150-65.
208. Qing H, Bonewald LF. Osteocyte remodeling of the perilacunar and pericanalicular matrix. Int J Oral Sci. 2009;1(2):59-65.
209. Teti A, Zallone A. Do osteocytes contribute to bone mineral homeostasis? Osteocytic osteolysis revisited. Bone. 2009;44(1):11-6.
210. Baud CA. Morphology and inframicroscopic structure of osteocytes. Acta Anat (Basel). 1962;51:209-25.
211. Belanger LF. Osteocytic osteolysis. Calcif Tissue Res. 1969;4(1):1-12.
212. Alcobendas M, Baud CA, Castanet J. Structural changes of the periosteocytic area in Vipera aspis (L.) (Ophidia, Viperidae) bone tissue in various physiological conditions. Calcif Tissue Int. 1991;49(1):53-7.
213. Lane NE, Yao W, Balooch M, Nalla RK, Balooch G, Habelitz S, et al. Glucocorticoid-treated mice have localized changes in trabecular bone material properties and osteocyte lacunar size that are not observed in placebo-treated or estrogen-deficient mice. J Bone Miner Res. 2006;21(3):466-76.
214. Qing H, Ardeshirpour L, Pajevic PD, Dusevich V, Jahn K, Kato S, et al. Demonstration of osteocytic perilacunar/canalicular remodeling in mice during lactation. J Bone Miner Res. 2012;27(5):1018-29.
215. Blaber EA, Dvorochkin N, Lee C, Alwood JS, Yousuf R, Pianetta P, et al. Microgravity induces pelvic bone loss through osteoclastic activity, osteocytic osteolysis, and osteoblastic cell cycle inhibition by CDKN1a/p21. PLoS One. 2013;8(4):e61372.
216. Baylink DJ, Wergedal JE. Bone formation by osteocytes. Am J Physiol. 1971;221(3):669-78.
217. Zambonin Zallone A, Teti A, Primavera MV, Pace G. Mature osteocytes behaviour in a repletion period: the occurrence of osteoplastic activity. Basic Appl Histochem. 1983;27(3):191-204.
218. Hesse B, Varga P, Langer M, Pacureanu A, Schrof S, Mannicke N, et al. Canalicular Network Morphology is the Major Determinant of the Spatial Distribution of Mass Density in Human Bone Tissue - Evidence by Means of Synchrotron Radiation Phase-Contrast Nano-CT. J Bone Miner Res. 2014.
219. Busse B, Djonic D, Milovanovic P, Hahn M, Puschel K, Ritchie RO, et al. Decrease in the osteocyte lacunar density accompanied by hypermineralized lacunar occlusion reveals failure and delay of remodeling in aged human bone. Aging Cell. 2010;9(6):1065-75.
220. Jarvinen TL, Pajamaki I, Sievanen H, Vuohelainen T, Tuukkanen J, Jarvinen M, et al. Femoral neck response to exercise and subsequent deconditioning in young and adult rats. J Bone Miner Res. 2003;18(7):1292-9.
221. Kesavan C, Mohan S, Oberholtzer S, Wergedal JE, Baylink DJ. Mechanical loading-induced gene expression and BMD changes are different in two inbred mouse strains. J Appl Physiol (1985). 2005;99(5):1951-7.
222. Polidoulis I, Beyene J, Cheung AM. The effect of exercise on pQCT parameters of bone structure and strength in postmenopausal women-a systematic review and meta-analysis of randomized controlled trials. Osteoporos Int. 2012;23(1):39-51.
223. Tidswell HK, Innes JF, Avery NC, Clegg PD, Barr AR, Vaughan-Thomas A, et al. High-intensity exercise induces structural, compositional and metabolic changes in cuboidal bones--findings from an equine athlete model. Bone. 2008;43(4):724-33.

224. Isaksson H, Tolvanen V, Finnila MA, Iivarinen J, Tuukkanen J, Seppanen K, et al. Physical exercise improves properties of bone and its collagen network in growing and maturing mice. Calcif Tissue Int. 2009;85(3):247-56.
225. Isaksson H, Tolvanen V, Finnila MA, Iivarinen J, Turunen A, Silvast TS, et al. Long-term voluntary exercise of male mice induces more beneficial effects on cancellous and cortical bone than on the collagenous matrix. Exp Gerontol. 2009;44(11):708-17.
226. Mechanic GL, Arnaud SB, Boyde A, Bromage TG, Buckendahl P, Elliott JC, et al. Regional distribution of mineral and matrix in the femurs of rats flown on Cosmos 1887 biosatellite. FASEB J. 1990;4(1):34-40.
227. Lafage-Proust MH, Collet P, Dubost JM, Laroche N, Alexandre C, Vico L. Space-related bone mineral redistribution and lack of bone mass recovery after reambulation in young rats. Am J Physiol. 1998;274(2 Pt 2):R324-34.
228. Patterson-Buckendahl P, Arnaud SB, Mechanic GL, Martin RB, Grindeland RE, Cann CE. Fragility and composition of growing rat bone after one week in spaceflight. Am J Physiol. 1987;252(2 Pt 2):R240-6.
229. Turner RT, Bell NH, Duvall P, Bobyn JD, Spector M, Holton EM, et al. Spaceflight results in formation of defective bone. Proc Soc Exp Biol Med. 1985;180(3):544-9.
230. Kohn DH, Sahar ND, Wallace JM, Golcuk K, Morris MD. Exercise alters mineral and matrix composition in the absence of adding new bone. Cells, tissues, organs. 2009;189(1-4):33-7.
231. Manjubala I, Liu Y, Epari DR, Roschger P, Schell H, Fratzl P, et al. Spatial and temporal variations of mechanical properties and mineral content of the external callus during bone healing. Bone. 2009;45(2):185-92.
232. Liu Y, Manjubala I, Schell H, Epari DR, Roschger P, Duda GN, et al. Size and habit of mineral particles in bone and mineralized callus during bone healing in sheep. J Bone Miner Res. 2010;25(9):2029-38.
233. Woo SL, Kuei SC, Amiel D, Gomez MA, Hayes WC, White FC, et al. The effect of prolonged physical training on the properties of long bone: a study of Wolff's Law. J Bone Joint Surg Am. 1981;63(5):780-7.
234. Vainionpaa A, Korpelainen R, Leppaluoto J, Jamsa T. Effects of high-impact exercise on bone mineral density: a randomized controlled trial in premenopausal women. Osteoporos Int. 2005;16(2):191-7.
235. Heinonen A, Kannus P, Sievanen H, Oja P, Pasanen M, Rinne M, et al. Randomised controlled trial of effect of high-impact exercise on selected risk factors for osteoporotic fractures. Lancet. 1996;348(9038):1343-7.
236. Kato T, Terashima T, Yamashita T, Hatanaka Y, Honda A, Umemura Y. Effect of low-repetition jump training on bone mineral density in young women. J Appl Physiol (1985). 2006;100(3):839-43.
237. Kerr D, Morton A, Dick I, Prince R. Exercise effects on bone mass in postmenopausal women are site-specific and load-dependent. J Bone Miner Res. 1996;11(2):218-25.
238. Kohrt WM, Ehsani AA, Birge SJ, Jr. Effects of exercise involving predominantly either joint-reaction or ground-reaction forces on bone mineral density in older women. J Bone Miner Res. 1997;12(8):1253-61.
239. Kohrt WM, Snead DB, Slatopolsky E, Birge SJ, Jr. Additive effects of weight-bearing exercise and estrogen on bone mineral density in older women. J Bone Miner Res. 1995;10(9):1303-11.
240. Fuchs RK, Bauer JJ, Snow CM. Jumping improves hip and lumbar spine bone mass in prepubescent children: a randomized controlled trial. J Bone Miner Res. 2001;16(1):148-56.
241. Vainionpaa A, Korpelainen R, Vihriala E, Rinta-Paavola A, Leppaluoto J, Jamsa T. Intensity of exercise is associated with bone density change in premenopausal women. Osteoporos Int. 2006;17(3):455-63.

242. Bassey EJ, Rothwell MC, Littlewood JJ, Pye DW. Pre- and postmenopausal women have different bone mineral density responses to the same high-impact exercise. J Bone Miner Res. 1998;13(12):1805-13.
243. Hoshi A, Watanabe H, Chiba M, Inaba Y. Effects of exercise at different ages on bone density and mechanical properties of femoral bone of aged mice. Tohoku J Exp Med. 1998;185(1):15-24.
244. Turner CH, Takano Y, Owan I. Aging changes mechanical loading thresholds for bone formation in rats. J Bone Miner Res. 1995;10(10):1544-9.
245. Buhl KM, Jacobs CR, Turner RT, Evans GL, Farrell PA, Donahue HJ. Aged bone displays an increased responsiveness to low-intensity resistance exercise. J Appl Physiol (1985). 2001;90(4):1359-64.
246. Rubin CT, Bain SD, McLeod KJ. Suppression of the osteogenic response in the aging skeleton. Calcif Tissue Int. 1992;50(4):306-13.
247. Srinivasan S, Agans SC, King KA, Moy NY, Poliachik SL, Gross TS. Enabling bone formation in the aged skeleton via rest-inserted mechanical loading. Bone. 2003;33(6):946-55.
248. Silbermann M, Bar-Shira-Maymon B, Coleman R, Reznick A, Weisman Y, Steinhagen-Thiessen E, et al. Long-term physical exercise retards trabecular bone loss in lumbar vertebrae of aging female mice. Calcif Tissue Int. 1990;46(2):80-93.
249. Lynch ME, Main RP, Xu Q, Schmicker TL, Schaffler MB, Wright TM, et al. Tibial compression is anabolic in the adult mouse skeleton despite reduced responsiveness with aging. Bone. 2011;49(3):439-46.
250. Leppanen OV, Sievanen H, Jokihaara J, Pajamaki I, Kannus P, Jarvinen TL. Pathogenesis of age-related osteoporosis: impaired mechano-responsiveness of bone is not the culprit. PLoS One. 2008;3(7):e2540.
251. Rianon NJ, Lang TF, Sigurdsson G, Eiriksdottir G, Sigurdsson S, Garcia M, et al. Lifelong physical activity in maintaining bone strength in older men and women of the Age, Gene/Environment Susceptibility-Reykjavik Study. Osteoporos Int. 2012;23(9):2303-12.
252. Engelke K, Kemmler W, Lauber D, Beeskow C, Pintag R, Kalender WA. Exercise maintains bone density at spine and hip EFOPS: a 3-year longitudinal study in early postmenopausal women. Osteoporos Int. 2006;17(1):133-42.
253. Lanyon L, Skerry T. Postmenopausal osteoporosis as a failure of bone's adaptation to functional loading: a hypothesis. J Bone Miner Res. 2001;16(11):1937-47.
254. Ehrlich PJ, Lanyon LE. Mechanical strain and bone cell function: a review. Osteoporos Int. 2002;13(9):688-700.
255. Kita K, Kawai K, Hirohata K. Changes in bone marrow blood flow with aging. J Orthop Res. 1987;5(4):569-75.
256. Kassem M, Marie PJ. Senescence-associated intrinsic mechanisms of osteoblast dysfunctions. Aging Cell. 2011;10(2):191-7.
257. Tonna EA. Electron microscopic study of bone surface changes during aging. The loss of cellular control and biofeedback. J Gerontol. 1978;33(2):163-77.
258. Sahin E, Depinho RA. Linking functional decline of telomeres, mitochondria and stem cells during ageing. Nature. 2010;464(7288):520-8.
259. Fedarko NS, Vetter UK, Robey PG. Age-related changes in bone matrix structure in vitro. Calcif Tissue Int. 1995;56 Suppl 1:S41-3.
260. Stanford CM, Welsch F, Kastner N, Thomas G, Zaharias R, Holtman K, et al. Primary human bone cultures from older patients do not respond at continuum levels of in vivo strain magnitudes. J Biomech. 2000;33(1):63-71.
261. Klein-Nulend J, Sterck JG, Semeins CM, Lips P, Joldersma M, Baart JA, et al. Donor age and mechanosensitivity of human bone cells. Osteoporos Int. 2002;13(2):137-46.
262. Sterck JG, Klein-Nulend J, Lips P, Burger EH. Response of normal and osteoporotic human bone cells to mechanical stress in vitro. Am J Physiol. 1998;274(6 Pt 1):E1113-20.

263. Termine JD. Cellular activity, matrix proteins, and aging bone. Exp Gerontol. 1990;25(3-4):217-21.
264. Nordin BE, Need AG, Chatterton BE, Horowitz M, Morris HA. The relative contributions of age and years since menopause to postmenopausal bone loss. J Clin Endocrinol Metab. 1990;70(1):83-8.
265. Slemenda C, Hui SL, Longcope C, Johnston CC. Sex steroids and bone mass. A study of changes about the time of menopause. J Clin Invest. 1987;80:1261-9.
266. Vashishth D, Verborgt O, Divine G, Schaffler MB, Fyhrie DP. Decline in osteocyte lacunar density in human cortical bone is associated with accumulation of microcracks with age. Bone. 2000;26(4):375-80.
267. Okada S, Yoshida S, Ashrafi SH, Schraufnagel DE. The canalicular structure of compact bone in the rat at different ages. Microsc Microanal. 2002;8(2):104-15.
268. Mullender MG, van der Meer DD, Huiskes R, Lips P. Osteocyte density changes in aging and osteoporosis. Bone. 1996;18(2):109-13.
269. Umemura Y, Ishiko T, Tsujimoto H, Miura H, Mokushi N, Suzuki H. Effects of jump training on bone hypertrophy in young and old rats. Int J Sports Med. 1995;16(6):364-7.
270. Brodt MD, Silva MJ. Aged mice have enhanced endocortical response and normal periosteal response compared with young-adult mice following 1 week of axial tibial compression. J Bone Miner Res. 2010;25(9):2006-15.
271. Raab DM, Smith EL, Crenshaw TD, Thomas DP. Bone mechanical properties after exercise training in young and old rats. J Appl Physiol (1985). 1990;68(1):130-4.
272. Holguin N, Brodt MD, Sanchez ME, Silva MJ. Aging diminishes lamellar and woven bone formation induced by tibial compression in adult C57BL/6. Bone. 2014;65:83-91.
273. Huang TH, Chang FL, Lin SC, Liu SH, Hsieh SS, Yang RS. Endurance treadmill running training benefits the biomaterial quality of bone in growing male Wistar rats. J Bone Miner Metab. 2008;26(4):350-7.
274. Main RP, Lynch ME, van der Meulen MC. In vivo tibial stiffness is maintained by whole bone morphology and cross-sectional geometry in growing female mice. J Biomech. 2010;43(14):2689-94.
275. Stauber M, Muller R. Micro-computed tomography: a method for the non-destructive evaluation of the three-dimensional structure of biological specimens. Methods Mol Biol. 2008;455:273-92.
276. Bouxsein ML, Boyd SK, Christiansen BA, Guldberg RE, Jepsen KJ, Muller R. Guidelines for assessment of bone microstructure in rodents using micro-computed tomography. J Bone Miner Res. 2010;25(7):1468-86.
277. Parfitt AM, Drezner MK, Glorieux FH, Kanis JA, Malluche H, Meunier PJ, et al. Bone histomorphometry: standardization of nomenclature, symbols, and units. Report of the ASBMR Histomorphometry Nomenclature Committee. J Bone Miner Res. 1987;2(6):595-610.
278. Krakty O, Porod G, Kahovec L. Einige Neuerungen in der Technik uns Auswertung von Rontgen-Kleinwinkelmessungen. Zeitschrift fur Elektrochemie. 1951;55(1):53-9.
279. Landis WJ, Paine MC, Glimcher MJ. Electron microscopic observation of bone tissue prepared anhydrously in organic solvents. Ultrastructure Res. 1977;63(2):188–223.
280. Hammersley AP, Svensson SO, Hanfland M, Fitch AN, Hausermann D. Two-dimensional detector software: From real detector to idealised image or two-theta scan High Pressure Research. 1996;14(4-6):235-48.
281. Fratzl P, Schreiber S, Klaushofer K, . Bone mineralization as studied by small-angle x-ray scattering. Connect Tissue Res. 1996;34((4)):247-54.
282. Helmchen F, Denk W. Deep tissue two-photon microscopy. Nat Methods. 2005;2(12):932-40.
283. Williams RM, Zipfel WR, Webb WW. Interpreting second-harmonic generation images of collagen I fibrils. Biophys J. 2005;88(2):1377-86.
284. Boskey AL, Mendelsohn R. Infrared spectroscopic characterization of mineralized tissues. Vib Spectrosc. 2005;38(1-2):107-14.

285. Marcott C, Reeder RC, Paschalis EP, Tatakis DN, Boskey AL, Mendelsohn R. Infrared microspectroscopic imaging of biomineralized tissues using a mercury-cadmium-telluride focal-plane array detector. Cell Mol Biol (Noisy-le-grand). 1998;44(1):109-15.
286. Faibish D, Gomes A, Boivin G, Binderman I, Boskey A. Infrared imaging of calcified tissue in bone biopsies from adults with osteomalacia. Bone. 2005;36(1):6-12.
287. Paschalis EP, Tatakis DN, Robins S, Fratzl P, Manjubala I, Zoehrer R, et al. Lathyrism-induced alterations in collagen cross-links influence the mechanical properties of bone material without affecting the mineral. Bone. 2011;49(6):1232-41.
288. Gourion-Arsiquaud S, Faibish D, Myers E, Spevak L, Compston J, Hodsman A, et al. Use of FTIR spectroscopic imaging to identify parameters associated with fragility fracture. J Bone Miner Res 2009;49(6):1565-71.
289. Razi H, Birkhold A, Zaslansky P, Weinkamer R, Duda GN, Willie BM, et al. Skeletal maturity leads to a reduction in the strain magnitudes induced within the bone: a murine tibia study Acta Biomater. 2014;under revision.
290. Kerschnitzki M, Wagermaier W, Roschger P, Seto J, Shahar R, Duda GN, et al. The organization of the osteocyte network mirrors the extracellular matrix orientation in bone. J Struct Biol. 2011;173(2):303-11.
291. Oliver WC, Pharr GM. An Improved Technique for Determining Hardness and Elastic-Modulus Using Load and Displacement Sensing Indentation Experiments. J Mater Res. 1992;7(6):1564-83.
292. Ozcivici E, Ferreri S, Qin Y, Judex S. Determination of Bone's Mechanical Matrix Properties by Nanoindentation. In: Westendorf JJ, editor. Osteoporosis Methods and Protocols Rochester: Human Press; 2011.
293. Willie BM, Birkhold AI, Razi H, Thiele T, Aido M, Kruck B, et al. Diminished response to in vivo mechanical loading in trabecular and not cortical bone in adulthood of female C57Bl/6 mice coincides with a reduction in deformation to load. Bone. 2013;55(2):335-46.
294. Aido M, Kerschnitzki M, Hoerth R, Burghammer M, Montero C, Checa S, et al. Relationship between nanoscale mineral properties and calcein labeling in mineralizing bone surfaces. Connect Tissue Res. 2014;55 Suppl 1:15-7.
295. Jilka RL. The relevance of mouse models for investigating age-related bone loss in humans. J Gerontol A Biol Sci Med Sci. 2013;68(10):1209-17.
296. Cerroni AM, Tomlinson GA, Turnquist JE, Grynpas MD. Bone mineral density, osteopenia, and osteoporosis in the rhesus macaques of Cayo Santiago. Am J Phys Anthropol. 2000;113(3):389-410.
297. Amblard D, Lafage-Proust MH, Laib A, Thomas T, Ruegsegger P, Alexandre C, et al. Tail suspension induces bone loss in skeletally mature mice in the C57BL/6J strain but not in the C3H/HeJ strain. J Bone Miner Res. 2003;18(3):561-9.
298. Beamer WG, Donahue LR, Rosen CJ, Baylink DJ. Genetic variability in adult bone density among inbred strains of mice. Bone. 1996;18(5):397-403.
299. Brodt MD, Ellis CB, Silva MJ. Growing C57Bl/6 mice increase whole bone mechanical properties by increasing geometric and material properties. J Bone Miner Res. 1999;14(12):2159-66.
300. Sugiyama T, Price JS, Lanyon LE. Functional adaptation to mechanical loading in both cortical and cancellous bone is controlled locally and is confined to the loaded bones. Bone. 2010;46(2):314-21.
301. Silva MJ, Brodt MD, Lynch MA, Stephens AL, Wood DJ, Civitelli R. Tibial loading increases osteogenic gene expression and cortical bone volume in mature and middle-aged mice. PLoS One. 2012;7(4):e34980.
302. Lynch ME, Main RP, Xu Q, Walsh DJ, Schaffler MB, Wright TM, et al. Cancellous bone adaptation to tibial compression is not sex dependent in growing mice. J Appl Physiol. 2010;109(3):685-91.

303. Birkhold AI, Razi H, Duda GN, Weinkamer R, Checa S, Willie BM. Mineralizing surface is the main target of mechanical stimulation independent of age: 3D dynamic in vivo morphometry. Bone. 2014;66:15-25.
304. Wallace JM, Rajachar RM, Allen MR, Bloomfield SA, Robey PG, Young MF, et al. Exercise-induced changes in the cortical bone of growing mice are bone- and gender-specific. Bone. 2007;40(4):1120-7.
305. Koistinen AP, Halmesmaki EP, Iivarinen JT, Arokoski JP, Brama PA, Jurvelin JS, et al. Short-term exercise-induced improvements in bone properties are for the most part not maintained during aging in hamsters. Exp Gerontol. 2014;51:46-53.
306. Banse X, Sims TJ, Bailey AJ. Mechanical properties of adult vertebral cancellous bone: correlation with collagen intermolecular cross-links. J Bone Miner Res. 2002;17(9):1621-8.
307. Vashishth D, Gibson GJ, Khoury JI, Schaffler MB, Kimura J, Fyhrie DP. Influence of nonenzymatic glycation on biomechanical properties of cortical bone. Bone. 2001;28(2):195-201.
308. Oxlund H, Barckman M, Ortoft G, Andreassen TT. Reduced concentrations of collagen cross-links are associated with reduced strength of bone. Bone. 1995;17(4 Suppl):365S-71S.
309. Saito M, Soshi S, Fujii K. Effect of hyper- and microgravity on collagen post-translational controls of MC3T3-E1 osteoblasts. J Bone Miner Res. 2003;18(9):1695-705.
310. Bonnet N, Standley KN, Bianchi EN, Stadelmann V, Foti M, Conway SJ, et al. The matricellular protein periostin is required for sost inhibition and the anabolic response to mechanical loading and physical activity. J Biol Chem. 2009;284(51):35939-50.
311. Shimazaki M, Nakamura K, Kii I, Kashima T, Amizuka N, Li M, et al. Periostin is essential for cardiac healing after acute myocardial infarction. J Exp Med. 2008;205(2):295-303.
312. Bromage TG, Goldman HM, McFarlin SC, Warshaw J, Boyde A, Riggs CM. Circularly polarized light standards for investigations of collagen fiber orientation in bone. Anat Rec B New Anat. 2003;274(1):157-68.
313. Razi H, Birkhold A, Duda GN, Willie BM, Checa S. Cortical bone in adult mice exhibits lower strain levels at remodeling sites compared to young mice. 19th Congress of the European Society of Biomechanic; Patras, Greece2013.
314. Dallas SL, Bonewald LF. Dynamics of the transition from osteoblast to osteocyte. Ann N Y Acad Sci. 2010;1192:437-43.
315. Holmbeck K, Bianco P, Pidoux I, Inoue S, Billinghurst RC, Wu W, et al. The metalloproteinase MT1-MMP is required for normal development and maintenance of osteocyte processes in bone. J Cell Sci. 2005;118(Pt 1):147-56.
316. Franz-Odendaal TA, Hall BK, Witten PE. Buried alive: how osteoblasts become osteocytes. Dev Dyn. 2006;235(1):176-90.
317. Sugawara Y, Kamioka H, Ishihara Y, Fujisawa N, Kawanabe N, Yamashiro T. The early mouse 3D osteocyte network in the presence and absence of mechanical loading. Bone. 2013;52(1):189-96.
318. Britz HM, Carter Y, Jokihaara J, Leppanen OV, Jarvinen TL, Belev G, et al. Prolonged unloading in growing rats reduces cortical osteocyte lacunar density and volume in the distal tibia. Bone. 2012;51(5):913-9.
319. Totland GK, Fjelldal PG, Kryvi H, Lokka G, Wargelius A, Sagstad A, et al. Sustained swimming increases the mineral content and osteocyte density of salmon vertebral bone. J Anat. 2011;219(4):490-501.
320. Zarrinkalam MR, Mulaibrahimovic A, Atkins GJ, Moore RJ. Changes in osteocyte density correspond with changes in osteoblast and osteoclast activity in an osteoporotic sheep model. Osteoporos Int. 2012;23(4):1329-36.
321. Himeno-Ando A, Izumi Y, Yamaguchi A, Iimura T. Structural differences in the osteocyte network between the calvaria and long bone revealed by three-dimensional

fluorescence morphometry, possibly reflecting distinct mechano-adaptations and sensitivities. Biochem Biophys Res Commun. 2012;417(2):765-70.
322. Potter RS. Age effects on the material and mechanical properties of bone at the osteocyte lacuna. Santo Antonio: The University of Texas; 2009.
323. Nicolella DP, Yao W, Lane N. Estrogen deficiency alters the localized material properties of the peri-lacunar bone matrix in old rats. J Bone Miner Res. 2008;23 Supp 1:S400.
324. Glatt V, Canalis E, Stadmeyer L, Bouxsein ML. Age-related changes in trabecular architecture differ in female and male C57BL/6J mice. J Bone Miner Res. 2007;22(8):1197-207.
325. Somerville JM, Aspden RM, Armour KE, Armour KJ, Reid DM. Growth of C57BL/6 mice and the material and mechanical properties of cortical bone from the tibia. Calcif Tissue Int. 2004;74(5):469-75.
326. Halloran BP, Ferguson VL, Simske SJ, Burghardt A, Venton LL, Majumdar S. Changes in bone structure and mass with advancing age in the male C57BL/6J mouse. J Bone Miner Res. 2002;17(6):1044-50.
327. Buie HR, Moore CP, Boyd SK. Postpubertal architectural developmental patterns differ between the L3 vertebra and proximal tibia in three inbred strains of mice. J Bone Miner Res. 2008;23(12):2048-59.
328. Morgan E, Bouxsein M. Biomechanics of Bone and Age-Related Fractures. In: Bilezikian JP, Raisz LG, Martin TJ, editors. Principles of Bone Biology: Academic Press; 2008.
329. Voide R, van Lenthe GH, Muller R. Bone morphometry strongly predicts cortical bone stiffness and strength, but not toughness, in inbred mouse models of high and low bone mass. J Bone Miner Res. 2008;23(8):1194-203.
330. Roschger P, Gupta HS, Berzlanovich A, Ittner G, Dempster DW, Fratzl P, et al. Constant mineralization density distribution in cancellous human bone. Bone. 2003;32(3):316-23.
331. Eyre DR, Dickson IR, Van Ness K. Collagen cross-linking in human bone and articular cartilage. Age-related changes in the content of mature hydroxypyridinium residues. Biochem J. 1988;252(2):495-500.
332. Li C, Paris O, Siegel S, Roschger P, Paschalis E, Klaushofer K, et al. Strontium is incorporated into mineral crystals only in newly formed bone during strontium ranelate treatment. J Bone Miner Res. 2010;25:968-79.
333. Erben RG. Bone-labeling techniques. In: An YH, Martin KL, editors. Handbook of histology methods for bone and cartillage: Totowa:Humana Press; 2003. p. 99-117.
334. Ibsen CJ, Birkedal H. Modification of bone-like apatite nanoparticle size and growth kinetics by alizarin red S. Nanoscale. 2010;2(11):2478-86.

Curriculum Vitae
Marta Aido

Higher Education

2010 - 2015	**Ph.D. student**, Technical University of Berlin/ Julius Wolff Institute, Charité-Universitätsmedizin Berlin, Germany Graduate School: Berlin-Brandenburg School for Regenerative Therapies
2005 - 2006	**Exchange student**, Delft University of Technology, The Netherlands
2003 - 2008	**M.Sc.**, Biomedical Engineering, Technical University of Lisbon, Portugal ***M.Sc. Thesis**: Ultrasound Contrast Agents in Triggered Drug and Gene Delivery*
	B.Sc., Biomedical Engineering, Technical University of Lisbon, Portugal

Additional Research Experience & Industry Internship

2008 - 2009	**Research Assistant**, National Institute of Biomedical Engineering, Biomaterials Department, Porto, Portugal ***European Project**: Development of a Bio-electrochemical Device for Central Nervous System Repair*
2007 - 2008	**Intern**, **Philips Research**, Bio-Molecular Engineering Department, Eindhoven, The Netherlands (M.Sc. Thesis)

Awards & Grants

2014	**Ph.D. Scholarship** for Ph.D. completion, Charité-Universitätsmedizin Berlin
2013	**Young Investigator Travel Award**, International Conference on the Chemistry and Biology of Mineralized Tissues
2013	**Travel Award,** Berlin-Brandenburg School for Regenerative Therapies
2011	**European Synchrotron Research Facility Grant**, beam line access
2011	**New Investigator Award***,* Joint Meeting of the European Calcified Tissue Society and the International Bone and Mineral Society

Publications

Aido, M., Kerschnitzki, M., Hoerth, R., Checa, S., Spevak, L., Boskey, A., Fratzl, P., Duda, G.N., Wagermaier, W., Willie, B.M., Effect of in vivo loading on bone composition varies with animal age, *Experimental Gerontology*, In press, 2015

Checa, S., Hesse, B., Roschger, P., **Aido, M.**, Duda, G.N., Raum, K., Willie, B.M., Skeletal maturation substantially affects elastic tissue properties in the endosteal and periosteal regions of loaded mice tibiae, *Acta Biomaterialia*, In press, 2015

Aido, M., Kerschnitzki, M., Hoerth, R., Checa, S., Burghammer, M., Montero, C., Fratzl, P., Duda, G., Willie, B.M., Wagermaier, W., Relationship between nanoscale mineral properties and calcein labeling in mineralizing bone surfaces, *Connective Tissue Research*, In press, 2014

Willie, B.M., Birkhold, A., Razi, H., Thiele, T., **Aido, M.**, Kruck, B., Schill, A., Checa, S., Main R.P., Duda, G.N., Diminished response to in vivo mechanical loading in trabecular and not cortical bone in adulthood of female C57Bl/6 mice coincides with a reduction in deformation to load, *Bone*, In press, 2013